

ABSTRACT

Title of Dissertation: CONSTRUCTION AND UTILIZATION OF
DIGITAL BRAIN ATLASES IN LARVAL
ZEBRAFISH

Gregory David Marquart
Doctor of Philosophy, 2017

Dissertation directed by: Adjunct Professor, Harold A. Burgess
Neuroscience and Cognitive Science Program
University of Maryland, College Park
and
Senior Investigator
Eunice Kennedy Shriver National Institute of
Child Health and Human Development
Bethesda, Maryland

Associate Professor, Jens Herberholz
Neuroscience and Cognitive Science Program
Psychology Department
University of Maryland, College Park

Rapid escape responses are critical for predator avoidance in fish. Yet, while short-latency C-start (SLCs) circuitry is well-known (e.g., Mauthner and related cells), neurons integral to long-latency C-starts (LLCs) remain uncharacterized. In this dissertation, I identify neurons critical for LLC through the genetic and laser ablations of neurons in transgenic lines.

Although transgenic lines provide powerful tools for implicating neurons in behavior, they suffer a number of limitations. Transgene expression is frequently broad, incompletely mapped, or off-target, making it difficult to accurately compare en masse or to other modalities. I addressed this by designing a UAS reporter that suppresses off-

target expression through microRNA binding and building a digital atlas from hundreds of transgenic zebrafish lines. By co-imaging and registering lines with a broadly expressed structural marker, the Zebrafish Brain Browser aligns expression to within approximately one cell diameter allowing rapid and accurate comparison of expression, identification of transgenes, and prediction of genetic overlap in almost any set of cells in the larval zebrafish brain. Other modalities (e.g., neural activity and anatomic segmentation) were also incorporated from Z-Brain, another popular zebrafish brain atlas, by a novel multichannel secondary registration. Together, this work increases the fidelity, interoperability, and accessibility of brain atlases and provides a powerful platform for the dissection of neural circuits in larval zebrafish.

Using these tools to design and analyze genetic ablations, I performed a 'circuit-breaking' screen to identify neurons underlying LLC behavior. Three of the screened lines reduced LLC probability by >50%. These lines labeled two shared cell clusters: one adjacent to the locus coeruleus (LC) and another in the dorsal hindbrain. Through laser ablation and optogenetic stimulation, LC-adjacent neurons were shown to be both necessary and sufficient for LLC startle. Projections of individual LC-adjacent neurons were characterized by a novel genetic intersection approach. These neurons were strikingly homogeneous, projecting bilaterally to midbrain and hindbrain structures. From this work, I hypothesize that ipsilateral hindbrain projections activate premotor neurons, while contralateral neurites subserve reciprocal inhibition. For the first time, I have identified a core component of the circuit mediating long-latency C-starts, an ethologically important behavior in zebrafish.

CONSTRUCTION AND UTILIZATION OF DIGITAL BRAIN ATLASES IN
LARVAL ZEBRAFISH

by

Gregory David Marquart

Dissertation submitted to the Faculty of the Graduate School of the
University of Maryland, College Park, in partial fulfillment
of the requirements for the degree of
Doctor of Philosophy
2017

Advisory Committee:

Associate Professor, Jens Herberholz, Ph.D., Chair
Adjunct Professor, Harold A. Burgess, Ph.D.
Assistant Professor, Quentin Gaudry, Ph.D.
Associate Professor, Matthew Ryan Roesch, Ph.D.
Professor, Richard Payne, Ph.D., Dean's Representative

© Copyright by
Gregory David Marquart
2017

Dedication

I dedicate this dissertation to all those who have supported and encouraged me throughout my life and in graduate school in particular. I would also like to dedicate this dissertation to all of those who though they had the aptitude, failed to receive the proper support and encouragement. I hope I have not squandered the opportunity that I received that they did not.

Acknowledgements

I would like to thank my parents AUDREY JOANN SCHALLA MARQUART and JAMES PATRICK MARQUART, my siblings ANTHONY JAMES MARQUART, MICHELLE LYNETTE MARQUART BAKER, CHRISTOPHER JOSEPH MARQUART, JOHN JAMES DER SCHALLA MARQUART, and RYAN PATRICK MARQUART, as well as my extended family – particularly my aunts PATRICIA JEANETTE MARQUART SEALE and JULES MAREE MARQUART and my uncle IRVING LAZAR for their kindness, generosity, and inspiration. I would also like to thank my close family friends, KIRBY WILLIAM HOLLADAY JR, PAMELA HOLLADAY, KENNETH LEE, JEANNIE LEE, HORST TREICHEL, and JOAN TRICHEL for their love and support.

Academically, I thank PAMELA CONNERLY and GRETCHEN KIRCHNER at IUS for restoring in me my scholastic confidence, giving me a taste for research, and supporting my pursuit of graduate school. At UMD, I would like to thank DAPHNE SOARES, ELIZABETH QUINLAN, and DAVID YAGER for their early guidance as well as QUENTIN GAUDRY, MATTHEW ROESCH, and RICHARD PAYNE for their support throughout.

I would also like to thank my labmates MATTHEW SWIERZBINSKI, DIVYA UMA, and LUCY VENUTI at UMD and SADIE BERGERON, JENNIFER SINCLAIR, and KATHRYN TABOR at the NICHD for their camaraderie. Outside of the lab, I would like to thank JEFFREY CHRABASZCZ, AMANDA CHICOLI, RONNY GENTRY, MOLLY HYER, and GREG PERRIN at UMD and DAN CASTRANOVA, AJAY CHITNIS, MARINA VENERO GALANTERNIK, and DAMIAN DALLE NOGARE at the NICHD for all of their conversations and conviviality. Last, I would like to thank KEVIN DONALDSON, ERIC HORSTICK, ADAM JONES, PAUL WATKINS, and JESSICA WESS for being steadfast friends throughout. I am sure that if it were not for their friendship and encouragement, I would not have made it through these many years.

Finally, I thank my co-advisors HAROLD ANTONY BURGESS and JENS HERBERHOLZ for seeing in me what sometimes I could not see myself. Words cannot express my appreciation for all of the opportunities, mentorship, tolerance, patience, and support that they have provided.

Table of Contents

Dedication	ii
Acknowledgements	iii
Table of Contents	iv
List of Figures	vii
List of Abbreviations	ix
Chapter 1: Apropos an introduction	1
An invertebrate's vertebrate	2
Digital atlases of the larval zebrafish brain (Chapter 2)	4
Combining digital brain atlases into a single platform (Chapter 3)	5
Identification of the LLC startle circuit in larval zebrafish (Chapter 4)	7
Chapter 2: A 3D searchable database of transgenic zebrafish Gal4 and Cre lines for functional neuroanatomy studies	10
Abstract	10
Introduction	11
Results	15
3-dimensional spatial registration of Gal4 lines	15
Characterization of enhancer trap lines by brain imaging and integration mapping	19
A 3D searchable interface for finding transgenic lines that express in a target region	22
Refining Gal4 reporter domains using Cre intersectional expression	28
Suppressing non-neuronal expression using microRNA	32
Discussion	34
Materials and Methods	40
Software and data availability	40
Animal husbandry	40
Transgenic lines	41
Imaging	44
Registration	45
Annotation	48
Synthetic 3' UTR constructs.	49

Supplementary Material	51
Chapter 3: High-precision registration between zebrafish brain atlases using symmetric diffeomorphic normalization	60
Abstract	60
Background	61
Methods	65
Zebrafish lines	65
Immunohistochemistry	66
Registration	66
Volume rendering & 3D visualization	67
Measurements	69
Results	71
Optimization of ANTs based registration of live vglut2a:DsRed image scans	71
Improved precision of ZBB after registration using ANTs	77
Optimization of ANTs registration parameters for fixed tissue	81
Inter-atlas registration using multi-channel diffeomorphic transformation	86
Neuroanatomical visualization	93
Discussion	96
Potential implications	100
Availability of supporting data	101
Additional Material	102
Chapter 4: Neural substrates of long-latency startle response in larval zebrafish	117
Abstract	117
Introduction	118
Results	121
Genetic ablation in y252Et, y293Et, and y330Et significantly reduces LLCs	121
Bilateral laser ablation eliminates LLCs	124
Optogenetic stimulation of vestibular nucleus elicits startle	126
R1 neurons project bilaterally in both the midbrain and hindbrain	128
Discussion	132
Methods	137
Animal Husbandry	137
Transgenic Lines	137

Imaging	138
Laser ablations	139
Immunohistochemistry	140
In situ hybridization	141
Behavioral analysis	143
Optogenetic activation	144
Neuron tracing	145
Acknowledgements	145
Chapter 5: Conclusion	152
Appendix 1: Decision making and behavioral choice during predator avoidance	159
Abstract	159
Introduction	160
Mechanisms of Predator Avoidance	161
Giant-Neuron Mediated Escape	165
Crayfish	165
Drosophila	169
Visual Interneuron Mediated Escape	175
Locust	175
Crabs	180
Value-Based Decision Making	186
Crayfish	188
Sea Slug	192
Conclusion and Future Directions	195
Bibliography	201

List of Figures

Figure 2.1. Method for high throughput, accurate registration of 6 dpf larval brains.	17
Figure 2.2. Average brain representations of Gal4 enhancer trap lines.	22
Figure 2.3. Brain browser software for searching enhancer trap lines.	25
Figure 2.4. Region of interest search with the brain browser.	27
Figure 2.5. Average brain representations of Cre enhancer trap lines.	30
Figure 2.6. Intersectional control of reporter gene expression in neurons expressing both Gal4 and Cre.	32
Figure 2.7. Suppression of non-neuronal expression using synthetic 3' untranslated regions.	34
Suppl. Figure 2.1. Optimization of brain registration using CMTK.	53
Suppl. Figure 2.2. Assessing registration accuracy by co-localized Gal4 reporter gene expression.	54
Suppl. Figure 2.3. Transgenic lines providing neuroanatomical markers.	56
Suppl. Figure 2.4. Extent of brain expression in Gal4 enhancer trap lines.	57
Suppl. Figure 2.5. Synthetic 3' UTR utr.zb1 suppresses transgene expression in muscle.	58
Suppl. Figure 2.6. Annotated sequence of utr.zb3.	59
Figure 3.1. Optimization of parameters for registration of live brain scans using ANTs.	74
Figure 3.2. Improved precision of transgene representations in ZBB1.2.	80
Figure 3.3. Optimization of ANTs registration parameters for fixed tissue.	84
Figure 3.4. Transformation between Z-Brain and ZBB coordinate systems using multi-channel registration.	90
Figure 3.5. 3D visualization of brain browser data.	95
Additional File 3.1. Point-based landmarks for quantification of live-scan registration precision.	102
Additional File 3.2. Cells segmented for assessing distortion introduced by registration.	105
Additional File 3.3. Point-based landmarks labeled by transgenic lines.	107
Additional File 3.4. ZBB and Z-Brain expression patterns used for atlas registration.	110
Additional File 3.5. Point-based landmarks for measuring precision of Z-Brain/ZBB co-registration.	113
Figure 4.1. Genetic ablation of Gal4 enhancer trap lines	123
Figure 4.2. Laser ablation of regions associated with LLC startle	126
Figure 4.3. Optogenetic stimulation of y293Et elicits startle responses	128

Figure 4.4. Morphology of individual R1 neurons associated with LLCs	131
Suppl. Figure 4.1. Genetic ablation startle kinematics	147
Suppl. Figure 4.2. R1 neurotransmitter identity	147
Suppl. Figure 4.3. Neural and non-neural y293Et expression	148
Suppl. Figure 4.4. R2 cells in y293Et are GFAP positive	149
Suppl. Figure 4.5. Traces of individual R1 neurons	150
Suppl. Video 4.1. Optogenetic stimulation of y293Et R1 neurons	151
Figure A1.1. Escape success and latencies measured in juvenile crayfish attacked by dragonfly nymphs.	169
Figure A1.2. Escape flight planning and execution in <i>Drosophila</i> .	173
Figure A1.3. Escape jump and DCMD activity in locusts in response to looming stimuli.	179
Figure A1.4. Response of a crab's LG neuron to looming stimuli and correlation with escape run.	182
Figure A1.5. Circuitry for arthropod escape behavior.	184
Figure A1.6. Escape choices and neural activation in crayfish exposed to approaching shadows.	191
Figure A1.7. Effects of internal state on behavioral choice in a sea slug.	194

List of Abbreviations

3D, 3 dimensional
ABS, Acrylonitrile butadiene styrene
afp, anti-freeze protein
aLLg, anterior lateral line ganglion
ASis, auditory sensory interneurons
ASns, auditory sensory neurons
BAC, bacterial artificial chromosome
BE, bath electrodes
BGi, rabbit β -globin intron 2
DCMD, descending contralateral movement detector neuron
DIMD, descending ipsilateral movement detector neuron
DLMns, dorsal lateral motor neurons
dpf, days post fertilization
E3h, E3 medium supplemented with HEPES
EG, eminentia granularis
Et - enhancer trap
FETi, fast extensor tibia motor neuron
Fiji, Fiji is just ImageJ
FJM, final joint movement
FLTis, flexor tibia motor neurons
FR, fasciculus retroflexus
GF, giant fiber
Gt - gene trap
IJM, initial joint movement
IO, inferior olive
IPN, interpeduncular nucleus
Hb, habenula
hpf, hours post fertilization
LAS AF, Leica Application Suite—Advanced Fluorescence
LDCMD, late descending contralateral movement detector neuron
LG, lateral giant (crayfish)
LG, lobula giant (crab)
LGMD, lobula giant movement detector neuron
LGMD2, lobula giant movement detector neuron 2
MG, medial giant
MoG, motor giant neuron
MS-222, tricaine methanesulfonate
MSis, mechanosensory interneurons

MSns, mechanosensory neurons
NCC, normalized cross-correlation
Non-G, non-giant
NRSE, neuronal restrictive silencing element
NucMLF, nucleus of the medial longitudinal fasciculus
OSis, olfactory sensory neurons
OSns, olfactory sensory neurons
OV, oral veil
PCR, polymerase chain reaction
PD, photodiodes
pLLg, posterior lateral line ganglion
Prob, proboscis
PSI, peripherally synapsing interneuron
PTU, N-Phenylthiourea
Rh, rhinophore
ROI, region of interest
SG, segmental giant neuron
SR, superior raphe
Tg, transgenic
Tn, tentacle
TTMn, tergotrochanteral muscle neuron
UAS, upstream activation sequence
UTR, untranslated region
VSis, visual sensory interneurons
VSns, visual sensory neurons

Chapter 1: Apropos an introduction

The human nervous system is the most complex system of which we have experience and so unsurprisingly, it has long been a subject of scientific inquiry. While this is due in part to its mesmerizing complexity, there are also profound philosophic and medical ramifications at stake in explaining its function. Indeed, few intellectual pursuits or areas of human health and well-being are likely not to be impacted by a better understanding of brain function. Nevertheless, while the problems of neuroscience have been pursued in a large number of model systems with a range of techniques, we still cannot adequately explain the function of even simple nervous systems, let alone the human brain. Despite volumes of observations, from ionic currents, to receptor-ligand interactions, to population encodings, and nonlinear summations; the nervous system remains impervious to our attempts at explanation.

Although every year we gain knowledge of evermore exquisitely detailed neuroscientific minutiae, our observations frequently lack a basic ‘compatibility’ necessary for them to be readily integrated into more comprehensive conceptual frameworks that would allow us to effectively aggregate this knowledge and craft ever more refined models of brain function. So even though we now have the capacity to simultaneously record neural activity from nearly all neurons found in small nervous systems (i.e., in zebrafish and *C. elegans*), we cannot systematically identify all parts of these systems across experimental specimen and aggregate information from a large

numbers of neurons across experiments. So, despite the fact that we can acquire brainwide at cellular resolution, we cannot analyze at cellular resolution.

Without methods allowing the alignment and identification of same cell groups across experimental organisms, we inevitably convolve disparate information from discordant parts of the nervous system and subsequently mask rather than elucidate potentially meaningful underlying neurobiology. Methods to faithfully align complex three-dimensional information on both the structure and function of the brain are needed. These methods will provide powerful tools for the effective aggregation of information and enable us to analyze at cellular resolution, rather than merely acquiring at cellular resolution. This will help us uncover important truths about underlying neurobiology more quickly and comprehensively.

An invertebrate's vertebrate

Larval zebrafish share gross vertebrate brain morphology with many neuroanatomic structures analogous to those found in humans easily identifiable. Yet at early stages of development, larval zebrafish have a numerical complexity (i.e., ~100,000 neurons) similar to that found in invertebrate systems (e.g., arthropods). With abundant genetic tools, high fecundity, rapid development, and a limited behavioral repertoire, zebrafish have emerged as a powerful neurobehavioral model system. In larval zebrafish, neural activity, genes, and underlying structure can be quantified at cellular resolution across the entire brain and tied to behavior allowing for systematic brain-wide analysis of

effects from experimental manipulations. Despite these benefits, however, many potentially informative biomarkers are but coarsely mapped, brain regions only broadly segmented, and many cell populations ill-defined. Given the complexity and variability of cell-types found in the brain, a full understanding of how the brain processes sensory information to control behavior will likely require the cellular-level characterization of the morphology, connectivity and function of individual neurons. We need ways to rapidly acquire, precisely align, and adroitly aggregate information in order to make comprehensive brainwide analysis and not just brainwide measurements.

The ease of genetic manipulation, a notable strength of zebrafish as a model, allows large numbers of transgenic lines, such as Gal4 and Cre enhancer traps, to be rapidly generated. These lines can be used to manipulate subsets of neurons with a high degree of specificity and reproducibility. The utility of transgenic lines, however, depends on how well the spatial and temporal extent of their expression is mapped and how well expression can then be driven in small enough populations of neurons as to affect discrete behaviors. Unfortunately, the expression of many transgenes is only coarsely mapped and consequently the full extent of what cells are being manipulated is unknown. Transgene expression is frequently not specific to the brain or not restricted to sufficiently discrete sets of neurons to allow for meaningful interrogation of the nervous system. High-resolution mapping of cellular level expression and alignment of expression patterns can be used to address this limitation.

As single transgenes are frequently too broadly expressed for effective manipulation of the nervous system, intersectional strategies with multiple transgenes can be used to target smaller more discrete neural subpopulations. For the effective design of intersectional strategies, however, expression patterns (e.g., for Gal4 and Cre) must be spatially characterized at high resolution and mapped in relation to one another so that overlapping expression domains can be predicted. This mapping of expression patterns into a shared reference space would give researchers a common resource or atlas in which to identify transgenic combinations that selectively label neurons of interest that would then be exploitable by intersectional genetic approaches. Although registration techniques have been applied to confocal imaging data from *Drosophila* and more recently to larval zebrafish [1–3], showing that volumetric registration techniques can be successfully applied to high resolution microscopy data, it remains unclear whether this can be performed on live tissue and systematically to large numbers of transgenic expression patterns of varying spatial extents and complexities through the larval zebrafish brain with sufficient fidelity to accurately predict genetic intersections.

Digital atlases of the larval zebrafish brain (Chapter 2)

In Chapter 2 of this dissertation, I address these problems by adapting volumetric registration techniques to create a large scale three-dimensional atlas of gene expression encompassing over one hundred transgenic lines in the larval zebrafish brain. This initial version of the Zebrafish Brain Browser (ZBB) is a compilation of 354 high resolution

brain scans from 109 distinct transgenic lines that have been registered into a common reference space. The workflow developed allows the rapid imaging, alignment, and integration of large numbers of cellular-resolution expression patterns into a common three-dimensional reference space which can be used to quickly visualize, catalogue, and analyze co-expression at any point within the brain. For this, ZBB includes software to visualize multiple lines as well as search among all lines either visually by 3-dimensional regions of interest (ROIs) or through text-based anatomical search. Importantly, ZBB also enables intersectional expression domains between Gal4 and Cre lines to be accurately predicted. This atlas has become a critical component of our own experimental workflows, but is a valuable resource for others in the field to utilize in their own research.

Combining digital brain atlases into a single platform (Chapter 3)

While ZBB provides zebrafish neuroscience researchers a unified framework for the aggregation and analysis of brainwide expression data, additional datasets exist that would be useful to integrate. Due to technical or experimental constraints, however, such datasets may be acquired with different reference channels used for alignment and consequently cannot be directly aligned to ZBB. Another recently released larval zebrafish brain atlas, Z-brain [4], exemplifies this situation. Z-Brain includes 29 immunohistochemical patterns co-imaged with total ERK (tERK) immunoreactivity that forms the basis of a manual expert segmentation of the larval zebrafish brain which is

used to interpret phosphorylated ERK (pERK) activity, a marker of neural activity. Although Z-Brain and ZBB are both powerful datasets in themselves, the complementary information contained in the two datasets would be of greater utility to the zebrafish neuroscience community if it were able to be combined into a single resource. Their contents, however, are not readily integrated as the two atlases utilize different references to which all data is co-imaged and aligned. ZBB uses a live transgenic marker for *vglut2a* and Z-Brain uses tERK immunoreactivity. Additionally, Z-Brain required the fixation of larval tissue rather than the use of live specimen and used different imaging parameters. Nevertheless, because ZBB and Z-Brain are 1) both constructed from data acquired from 6 days post fertilization larval zebrafish and 2) share several genetic markers in common that could be used in a secondary ‘bridging’ registration step, we speculated that the two atlases could be merged despite disparate reference channels, differences in image acquisition, and morphological aberrations introduced by tissue fixation. In Chapter 3, I address this compatibility problem by employing a multi-channel bridging that enables accurate alignment between ZBB and Z-Brain. Additionally, registration parameters were optimized to compensate for morphological aberrations introduced by tissue fixation. Together, this optimization and bridging between ZBB and Z-Brain greatly increases the gene expression information available in Z-Brain and allows for the integration of immunohistochemical stains and expert manual segmentation into ZBB.

Identification of the LLC startle circuit in larval zebrafish (Chapter 4)

It is critical for an organism to identify and react to predatory cues in an appropriate time and manner. Although ‘anticipatory’ anti-predation behaviors may exist, in simple nervous systems fast start escape behaviors are the predominant anti-predator behaviors. The time-sensitive nature of anti-predatory behaviors was thought to require simple circuits consisting of a small number of large cells, which by minimizing synaptic delay and maximizing conduction velocity ensured a rapid response to attack. In these “command” or “command-like” systems, activity of a single neuron is often both necessary and sufficient for production of escape behavior. Evidence from many models, however, suggests the existence of alternative slightly slower, but more variable startle responses. These alternative systems which lack classic command elements typically display a greater degree of complexity and flexibility that affords an increased level of control over the timing, direction, and structure of the response.

In fish, ‘C-start’ escape responses are the principal behaviors utilized for predator avoidance. C-starts can be elicited by multiple modalities, but responses to acousto-vibrational stimuli are the most thoroughly characterized. The majority of work has focused on circuits associated with the Mauthner cells (M-cells) whose electrophysiological activity has been linked to the performance of C-starts. Indeed, C-start responses were thought to rely exclusively on these M-cells. However, ablation studies and high-speed behavioral analysis suggests M-cell-independent startle circuitry

must exist. When startle behavior is analyzed at high-speed, responses are distributed bimodally, which the two distributions commonly referred to as short-latency C-starts (SLCs) and long-latency C-starts (LLCs). And although the performance of SLCs corresponds to M-cell activation and is eliminated following M-cell ablation, LLC production does not correlate to M-cell activity and they persist following M-cell ablation. Command-like neurons like the M-cell have frequently been easily identified due to their large size and distinctive morphology. Because they lack large easily identifiable command elements, neural circuits for alternative non-giant startle behaviors have been harder to identify. So, although much is known of the circuit responsible for SLCs, virtually nothing is known of that which underlies LLC behavior.

Digital atlases like ZBB can be used to design unbiased genetic ablation screens that may uncover previously unknown neural circuits underlying behaviors like LLC startle. With ZBB, lines can be identified that cumulatively cover the majority of the larval zebrafish brain and these lines can then be used to systematically test all brain regions for a role in behavior. In Chapter 4, to identify components of the circuit or circuits responsible for LLC startle and as a proof of principle of the utility of digital brain atlases, I performed a “circuit-breaking” genetic screen. In genetic ablations that reduced LLC probability, I looked for common patterns in the expression of affected lines. While genetic ablations may reduce LLC probability through the disruption of distinct circuits, alternatively, they may hit upon shared components identifiable by the overlap in expression of affected lines. This overlap would hypothetically narrow down

the possible locus or loci of cells underlying LLC startle. Lines reducing LLCs overlapped in two locations. Through laser ablations and optogenetic stimulation, one of these two regions was identified as critical for LLC behavior. With this result, for the first time, I have identified a core component of the circuit mediating long-latency C-starts, an ethologically important behavior in zebrafish.

Chapter 2: A 3D searchable database of transgenic zebrafish Gal4 and Cre lines for functional neuroanatomy studies

The work presented in this chapter has been edited for stylistic consistency and to conform with Graduate School guidelines, but has been published previously as:

Marquart GD, Tabor KM, Brown M, Strykowski JL, Varshney GK, LaFave MC, Mueller T, Burgess SM, Higashijima S-I, Burgess HA. A 3D Searchable Database of Transgenic Zebrafish Gal4 and Cre Lines for Functional Neuroanatomy Studies. *Front Neural Circuits* (2015) **9**:1566.

Abstract

Transgenic methods enable the selective manipulation of neurons for functional mapping of neuronal circuits. Using confocal microscopy, we have imaged the cellular-level expression of 109 transgenic lines in live 6 day post fertilization larvae, including 80 Gal4 enhancer trap lines, 9 Cre enhancer trap lines and 20 transgenic lines that express fluorescent proteins in defined gene-specific patterns. Image stacks were acquired at single micron resolution, together with a broadly expressed neural marker, which we used to align enhancer trap reporter patterns into a common 3-dimensional reference space. To facilitate use of this resource, we have written software that enables searching for transgenic lines that label cells within a selectable 3-dimensional region of interest or neuroanatomical area. This software also enables the intersectional expression of transgenes to be predicted, a feature which we validated by detecting cells with co-expression of Cre and Gal4. Many of the imaged enhancer trap lines show intrinsic brain-specific expression. However, to increase the utility of lines that also drive expression in non-neuronal tissue we have designed a novel UAS reporter, that suppresses expression

in heart, muscle and skin through the incorporation of microRNA binding sites in a synthetic 3' untranslated region. Finally, we mapped the site of transgene integration, thus providing molecular identification of the expression pattern for most lines. Cumulatively, this library of enhancer trap lines provides genetic access to 70% of the larval brain and is therefore a powerful and broadly accessible tool for the dissection of neural circuits in larval zebrafish.

Introduction

A full understanding of how the brain processes sensory information to control behavior requires the cellular-level characterization of the morphology, connectivity and function of individual neurons. To this end, genetic tools are increasingly used to activate transgene expression in subsets of neurons with a high degree of cell-type specificity. A powerful repertoire of transgenic methods has been developed to visualize, monitor and manipulate neurons in larval zebrafish. However, the usefulness of these tools depends on the precision with which their expression can be reproducibly driven in small defined populations. In many cases, transgene expression is neither specific to the brain, nor restricted to a sufficiently discrete set of neurons to allow for functional interrogation of the nervous system.

Several strategies have been used for genetically targeting neurons. Promoter fragments, containing cis-regulatory elements from genes expressed in target neurons often allow reporter genes to be expressed in the same cells [5]. Larger genomic regions

cloned into bacterial artificial chromosomes have also been successfully used to faithfully recapitulate gene-specific patterns [6,7]. However, as few genes are expressed in small numbers of neurons, these approaches seldom yield highly discrete domains of reporter expression. Moreover, the generation of each such line is often resource and labor intensive. In contrast, a large number of transgenic “enhancer trap” lines can be rapidly and easily generated through random transposase-mediated transgene integration where transgene expression is directed by regulatory elements flanking the site of integration [8–10]. In particular, the high germ line efficiency of *tol2* has enabled several large scale Gal4 enhancer trap screens [11–13] and provided transgenic zebrafish lines that have proven powerful tools for both imaging as well as interrogating the function of the nervous system [14]. Still, only a small proportion of these enhancer trap lines show strongly restricted patterns of expression. An alternative strategy was recently tested in which a large number of ~3 kbp genomic DNA fragments from neuronal genes was used to generate transgenic lines [15]. It was hypothesized that these fragments, each containing only a subset of gene regulatory elements, would drive highly restricted patterns of neuronal expression. However, from more than 7000 such fragments tested in *Drosophila*, less than 0.1% directed reporter expression to a single neuronal cell type [16]. Thus at present, small groups of neurons - required for functional interrogation - cannot be reliably targeted using single transgene methods alone.

A promising approach is to use intersectional strategies that require two transgenes to be expressed in the same cell to activate expression of a reporter gene. To

implement such methods, a number of extensions to the classic Gal4/UAS system have been introduced, including split-Gal4 and expression of the Gal4 inhibitor protein, Gal80 [17,18]. Recombinases such as Cre have also been used to further restrict Gal4 expression domains, for example by removing a stop cassette downstream of the UAS promoter [19]. Gal4 and Cre driver lines have successfully been used for intersectional approaches in zebrafish [20], making this an appealing strategy to achieve highly targeted reporter expression in neuronal cell types.

To expedite the design and maximize the utility of such intersectional strategies, Gal4 and Cre expression patterns must be spatially characterized at high resolution. Only recently have cellular level resolution images of Gal4 enhancer trap lines been made available [21]. Moreover, these expression patterns should ideally be integrated into a common spatial coordinate system in order to predict domains of overlapping expression, enabling researchers to better identify combinations of Gal4 and Cre transgenic lines that label select neurons of interest. This problem can be solved through inclusion of a reference channel and registration of confocal scans to a single common reference brain. Rigorous methods that correct for small inter-individual differences in brain structure or morphology have been developed and applied extensively to human magnetic resonance imaging data. Such brain registration techniques have also been applied to confocal imaging data from *Drosophila* and more recently to larval zebrafish brain scans [1–4]. These studies illustrate the feasibility and potential utility of applying volumetric registration techniques to confocal imaging data at the scale of the larval zebrafish brain.

Here, we present a database of the expression patterns of 109 transgenic lines that have been registered into a common reference space, derived from 354 high resolution brain scans. We provide 'brain browser' software that facilitates the rapid visualization of multiple lines and enables searching lines using anatomic labels, or user defined 3-dimensional regions of interest. The database includes 80 Gal4 enhancer trap lines and 9 Cre enhancer trap lines. To aid in navigating the brain and interpreting enhancer trap expression patterns, we also imaged 20 transgenic lines with genetically defined expression patterns. We show that the browser can be used to find enhancer trap lines that label specific neurons, or even the projection targets of neurons of interest. The browser also enables the intersectional expression domains of Cre and Gal4 lines to be predicted. As a step toward future systematic functional analyses of brain function, the browser also allows a given expression pattern to be used as the template to delineate a set of transgenic lines that cover the same region with minimal overlap.

Transgenic lines with minimal expression outside the brain are the most valuable for neuroscience research. While we have previously shown that non-neuronal expression can be suppressed by inclusion of one or more neuronal restrictive silencing elements in the transgene vector [22,23], this technique cannot be retroactively applied to refine expression of many valuable existing Gal4 lines. Instead, here we tested synthetic 3' untranslated regions (UTRs) that incorporate target sites for microRNAs that are highly expressed in non-neuronal tissues for their ability to suppress expression outside the brain. MicroRNAs are 21-22 nucleotide ribonucleic acid hairpins that repress translation

or destabilize messenger RNA [24–26]. Each microRNA suppresses the expression of target genes that contain 7-8 nucleotides that are complementary to the microRNA 'seed' sequence. We show that one synthetic 3' UTR (utr.zb3), containing target sites for several non-neuronal microRNAs, strongly suppresses expression of a UAS driven reporter in heart, muscle and skin. This synthetic UTR thus enables the use of numerous lines previously inaccessible to desirable experimental manipulations.

Results

3-dimensional spatial registration of Gal4 lines

To construct a high resolution database of enhancer trap lines, we first developed a pipeline for generating average brain representations for transgenic lines (**Fig. 2.1A**). We used *UAS:Kaede* as a reporter to visualize Gal4 expression, and the *vglut2a:DsRed* transgenic line, which has a broad pattern of DsRed expression, as a reference channel for image registration. At 6 dpf, brain images of live Gal4, *UAS:Kaede*, *vglut2a:DsRed* larvae were acquired with a confocal microscope at single micron resolution. To reduce scan times, we collected Kaede and DsRed fluorescence simultaneously, with post-scan linear unmixing to eliminate cross-talk between channels. We acquired two image stacks for each brain, covering rostral and caudal regions, which were stitched together prior to image registration. For registration, we used the Computational Morphometry Toolkit (CMTK) (Rohlfing and Maurer, 2003). To find optimal registration parameters, we used

a calibration set, comprising larvae that were scanned, remounted and rescanned. Using normalized cross-correlation as a measure of registration quality between duplicate scans of the calibration set, we identified an individual *vglut2a:DsRed* brain that yielded the best registrations to use as the reference. We then systematically tested registration parameters to obtain the most accurate alignments while minimizing computation time (see **Methods: Registration** and *Supp. Fig. 2.1B* for additional details).

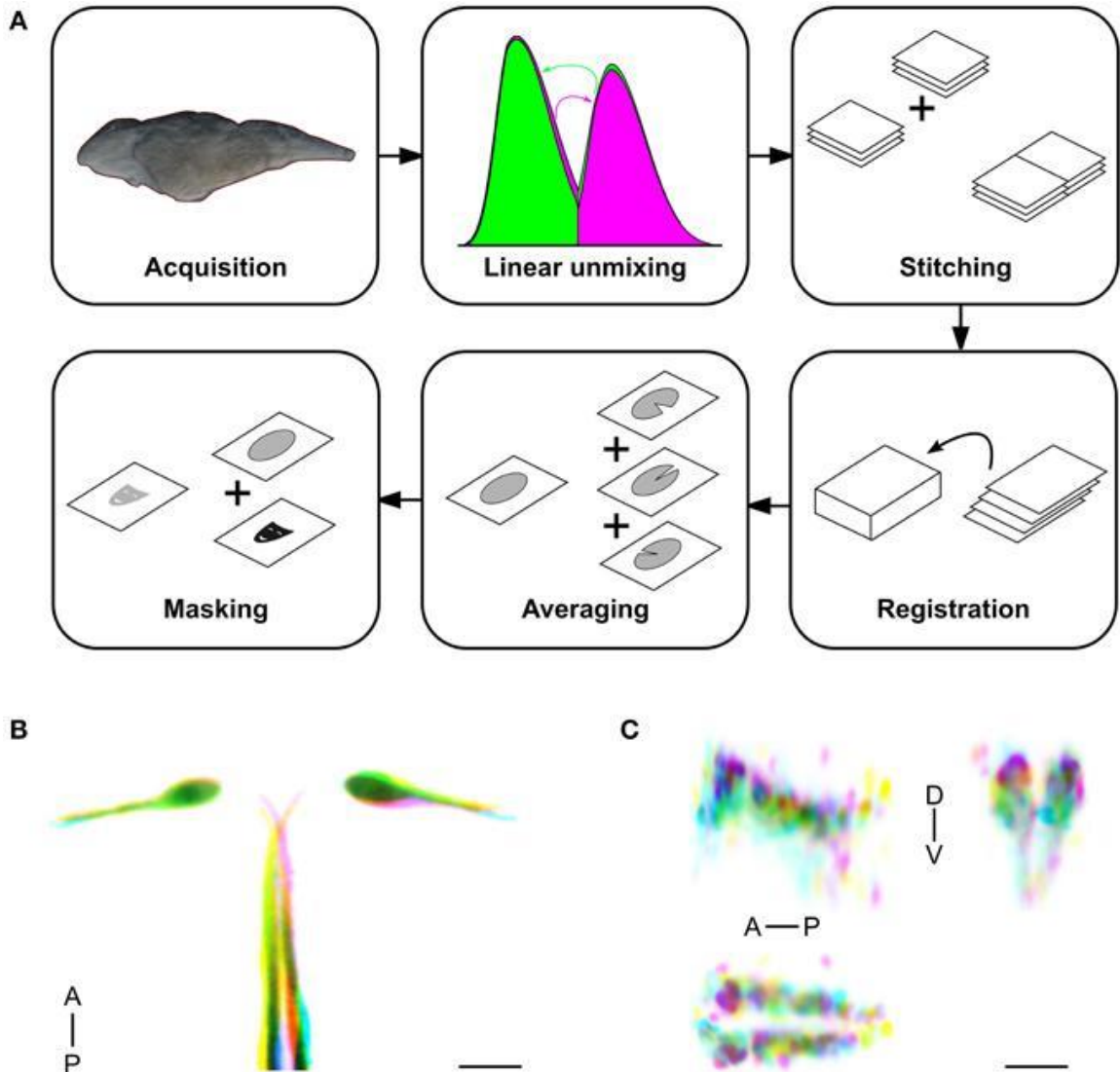


Figure 2.1. Method for high throughput, accurate registration of 6 dpf larval brains.

Image 1: **(A)** Acquisition and computation pipeline, detailed protocols for each step are described in the Materials and Methods section. **(B)** Overlay of the Mauthner cell, from single image stacks taken from three different *y264Et* larvae (color-coded yellow, pink and blue respectively). Good correspondence is seen for the soma and lateral dendrite region, with more variability in the position of the axon. Scale bar 25 μm . **(C)** Overlay of the superior raphe nucleus, from averaged image stacks for lines *y228Tg* (pink), *y293Et* (blue), and *y308Et* (yellow), shown using a sagittal projection through the region (top

left), a transverse projection (top right) and horizontal projection (bottom). Anterior (A), Posterior (P), Dorsal (D), Ventral (V). Scale bar 25 μm .

Based on findings from previous work [27], we averaged imaging data from a minimum of three larvae per line to generate representations of Gal4 expression. Averaging helped to fill-in information that was incomplete in any one larva due to variegated expression, yielding a more accurate representation of the expression present in each line than data from a single fish. Next we applied a mask to the average image stack that removed expression data and background fluorescence from outside the brain, enabling 3D visualization of brain expression patterns. To assess the accuracy of our registration pipeline, we compared registered images acquired from transgenic larvae with overlapping expression patterns. *j1229aGt* and *y264Tg* both label the Mauthner cell [28,29]. The *vglut2a:DsRed* reference channel does not label these neurons; nevertheless, Mauthner cell bodies were brought into close alignment in three individual *y264Tg* larvae (**Fig. 2.1B**). Similarly, the Mauthner cells show near perfect overlap between the average representations of *y264Tg* and *j1229aGt* (**Supp. Fig. 2.2A,B**). To assess the accuracy of registration for smaller, potentially more variable cell populations, we compared lines *y228Tg*, *y293Et* and *y308Et* which all label the superior raphe nucleus as part of their expression domain. Within the raphe, expression patterns registered to within approximately 1 cell diameter (**Fig. 2.1C**). Next, we compared two average representations for enhancer trap line *y339Et* that were produced from independent sets of larvae. Projections and slices from these stacks were visually similar (**Supp. Fig.**

2C,D). Finally, we noted that after registration, vascular GFP expression in *flk:GFP* aligned well with gaps in the pan-neuronal HuC: Cer pattern, confirming that our imaging pipeline yielded accurate representations of transgene expression patterns (*Supp. Fig. 2E,F*).

Characterization of enhancer trap lines by brain imaging and integration mapping

We previously generated more than 200 transgenic Gal4 lines while developing a new vector that allows for brain-specific enhancer trapping [22]. Additionally, during the isolation of transgenic Gal4 lines that used defined promoter elements from the *tph2* and *dbh* genes, we retained several lines with robust Gal4 expression that extended beyond the corresponding gene expression domain, and that are thus effectively enhancer traps. Based on visual inspection of expression patterns under epifluorescence, we selected 80 lines that appeared most useful for anatomical and behavioral experiments, to characterize using high resolution imaging and brain registration (*Table 2.1*). In addition, we selected 20 transgenic lines that were generated using BACs or promoters from genes with well-defined expression patterns, thus providing anatomical landmarks and cell type information for annotating the Gal4 enhancer trap lines (*Supp. Fig. 2.3A*). We then scanned the brains of 256 Gal4-expressing and 98 other transgenic larvae (*Fig. 2.2, Supp. Fig. 3B*), comprising 3-10 individuals for each line. Images were processed using the pipeline described above, producing a single representation of each line. We manually

annotated neuroanatomical structures labeled by each line, and collected an epifluorescent image to characterize the extent of non-neuronal expression (*Supp. Table 2.1*).

Table 2.1. Summary of enhancer trap lines imaged.

Vector	Imaged	Neural		Integration site			
		Specific	Mapped	Intergenic	Exon	Intron 1	Intron 2+
cfos:Gal4	19	5	11	10	-	-	1
REx2-cfos:Gal4	18	16	12	6	1	2	3
SCP1:Gal4	13	1	8	2	3	-	3
REx2-SCP1:Gal4	24	7	14	6b	2	2	4
E-trap:Gal4a	6	4	5	3b	-	2	-
REx2-SCP1:Cre	6	4	-	-	-	-	-
attp-REx2-SCP1:Cre	3	2	-	-	-	-	-
<i>Total</i>	<i>89</i>	<i>39</i>	<i>50</i>	<i>27</i>	<i>6</i>	<i>6</i>	<i>11</i>

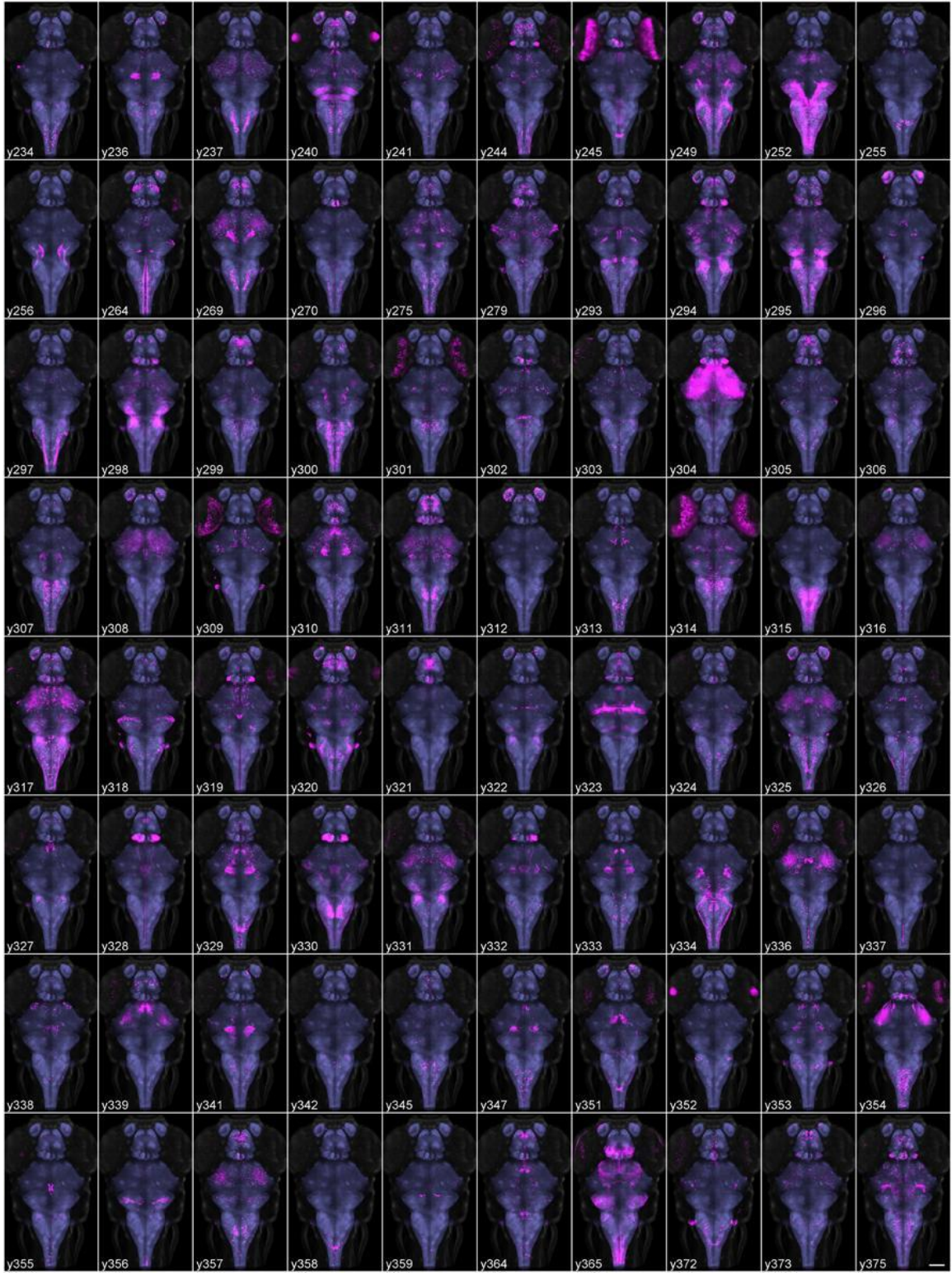


Figure 2.2. Average brain representations of Gal4 enhancer trap lines.

Maximum projections through 80 Gal4 enhancer trap lines that were imaged, registered and averaged for this study. Gal4 expression was visualized using the *UAS:Kaede* transgenic line (magenta). Each panel is the average of at least three brains. For contrast, each panel also shows ubiquitous *βactin:Switch* expression (gray) and pan-neuronal *HuC: Cer* expression (blue, after application of brain mask). Scale bar (bottom right panel) 100 μm.

Identification of the genomic location of enhancer trap lines may in some cases reveal valuable information about the cell-type expressing the transgene, or indicate whether an endogenous gene is possibly disrupted by the insertion [30,31]. We therefore collected DNA samples from Gal4 enhancer trap lines, used high-throughput sequencing to map the integration site of the transgenes and verified map positions using PCR [32]. For 12 of the 50 imaged lines that were mapped, the integration site was located in an exon or first intron and may therefore disrupt gene expression (*Supp. Table 2.1*). We also confirmed integration positions for an additional 48 lines that were not selected for imaging due to strong non-neuronal expression or the lack of a discrete pattern within the brain. Gene expression is likely perturbed in 21 lines from this group (*Supp. Table 2.2*).

A 3D searchable interface for finding transgenic lines that express in a target region

All of the transgenic and enhancer trap lines in this dataset have been registered to the same coordinate space, allowing expression patterns to be compared using widely available software tools such as ImageJ or FluoRender [33,34]. However, searching for lines that show expression in a given 3D region of interest (ROI) or among a specific

group of neurons is less straightforward. We addressed this problem by writing new 'brain browser' software that allows users to highlight either a given 3D volume, or specific cells within 3D regions, and search for transgenic lines in the data set that contain fluorescent pixels in the defined area of interest.

The Zebrafish Brain Browser simultaneously displays slices or projections of selected lines in horizontal, sagittal and transverse views (*Fig. 2.3A-C*). Clicking on a point in any view updates the other two windows to display corresponding slices through the same point. An additional panel gives ancillary information about the currently selected line, including the integration site of the transgene and nearest gene, neuroanatomical annotation as well as an epifluorescent image of the whole fish. Users can rapidly perform maximum projections of selected 3D regions (*Fig. 2.3A*), zoom into areas of interest, or visualize selected lines as a 3D projection (*Fig. 2.3D*).

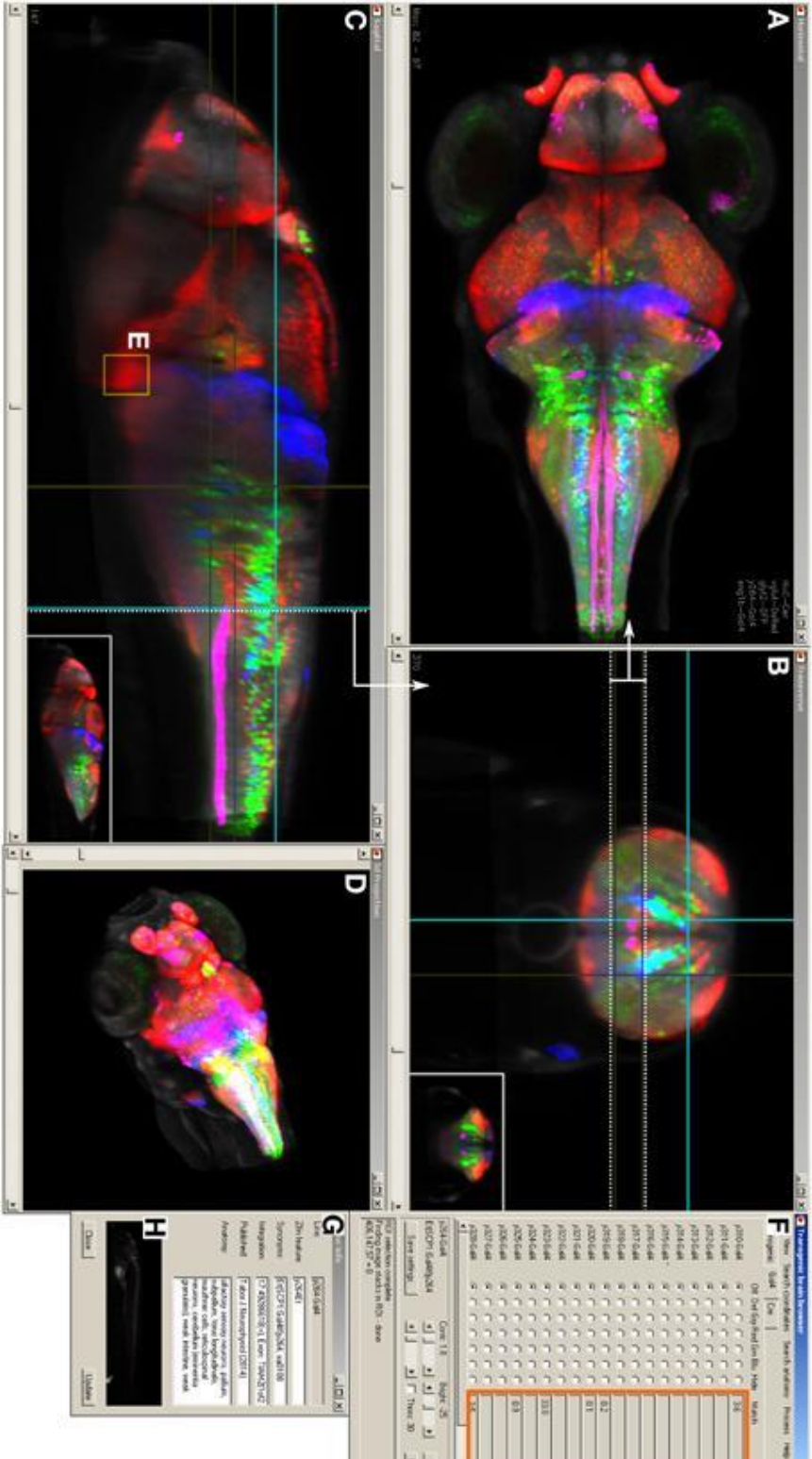


Figure 2.3. Brain browser software for searching enhancer trap lines.

The browser displays horizontal (**A**), transverse (or oblique), (**B**) and sagittal (**C**) views of user-selected image stacks of transgenic and enhancer trap lines. The browser displays single brain slices (**B,C**), using cross-hairs to indicate the slice location in orthogonal planes (e.g., dotted line in **C** shows the position of the transverse view in **B**). Alternatively, maximum projections of selected regions can be visualized (**A**, between the region indicated by dotted lines in **B**) or a 3D projection of the whole brain (**D**). The control panel (**F**) lists all lines in the database and during searches, indicates lines (orange box) that label selected 3D regions of interest (**E**) or neuroanatomical structures. Information on the transgene integration site and neuroanatomical annotation are available in an additional panel (**G**), which also contains epifluorescent images for all Gal4 enhancer trap lines (**H**).

Selecting a single pixel in 3D space highlights all lines that express the transgene at the matching coordinate. To search more thoroughly for a line that labels cells in a given region, the user can create a 3D ROI encompassing a given volume, or select cell bodies that are part of a chosen transgenic line (**Fig. 2.3E**). The ROI is used as a mask to identify fluorescent pixels in all other lines in the database. Based on the number of fluorescent pixels in the ROI, the user can then inspect lines likely to contain cells in that region. For instance, to identify a Gal4 line that labels the inferior olive (IO), we first located this structure in the ventral caudal medulla using the *vglut2a:DsRed* line [35,36]. We selected an ROI encompassing neurons in the IO (**Fig. 2.4A**) and inspected Gal4 lines that the browser reported labeled that region (**Fig. 2.4B-D**). The three top hits, *y311Et*, *y320Et* and *y330Et* all strongly expressed Gal4 in IO neurons. Similarly, projection targets of axon tracts may be identified by highlighting the termination zone using suitable transgenic lines, and searching for enhancer trap lines containing cells in the region. For instance, line *y328Et* strongly labels the projection of habenula neurons via

the fasciculus retroflexus to their termination zone in the interpeduncular nucleus (IPN, *Fig. 2.4E*). We selected an ROI in the termination area of the fasciculus retroflexus and searched for a Gal4 line that labeled neurons in the IPN. Line y300Et contained cell bodies in the search area (*Fig. 2.4F*) and we confirmed that these neurons are within the IPN by immunostaining y300Et for somatostatin (*Fig. 2.4G*) [37].

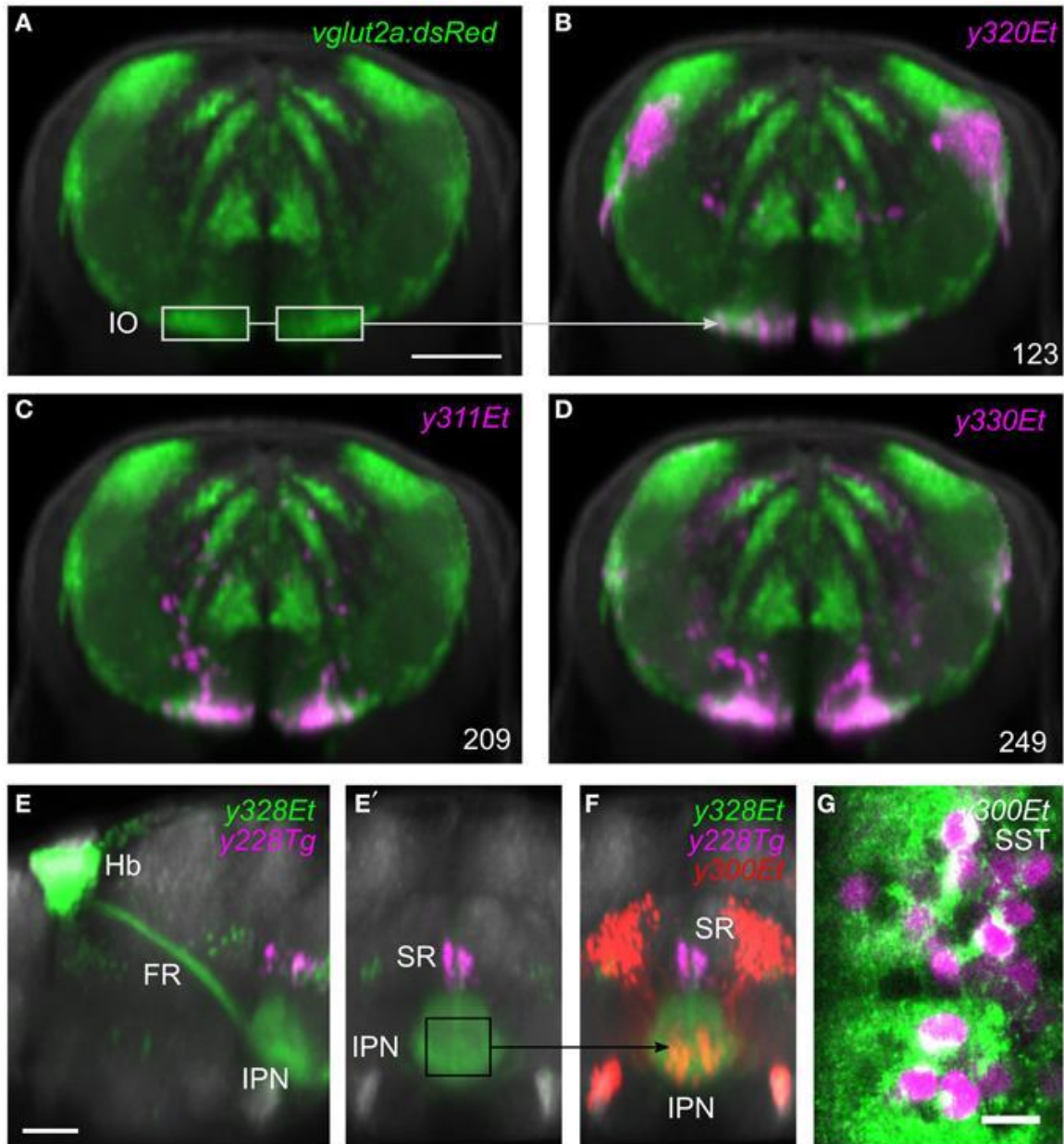


Figure 2.4. Region of interest search with the brain browser.

(A) Transverse view through caudal medulla of vglut2a:DsRed average brain (green). The boxed regions were used to draw a region of interest around the inferior olive (IO) to search the database for Gal4 lines labeling IO neurons. Scale bar 50 μ m. (B–D) The three Gal4 enhancer trap lines that most strongly matched the search area (magenta). Each line contained neurons in the region of the IO. (E) Sagittal and (E') transverse projections of

line *y328Et* (green) which labels the habenula (Hb) and fasciculus retroflexus (FR) including termination zone in the interpeduncular nucleus (IPN). For orientation, a line labeling the superior raphe (SR) is also shown (*y228Tg*, magenta). The termination zone of habenula neurons in the IPN was used to create a 3D search region. Scale bar 50 μm . **(F)** Brain browser image showing the result of the 3D search: enhancer trap line *y300Et* (red) which contained strongly fluorescent cell bodies within the IPN. **(G)** Single confocal plane showing immunostaining against somatostatin (SST, green) and transgene expression in *y300Et* (Kaede fluorescence, magenta) within the IPN. Scale bar 10 μm .

At present, the most widely used neuroanatomical atlas of the larval zebrafish brain contains limited molecularly defined detail for up to 5 dpf larvae [38] and therefore the neuroanatomical annotation of each enhancer trap line is not complete. Nevertheless, we extracted neuroanatomical terms from the Zebrafish Anatomical Ontology [39] and provide these as search terms from a series of drop-down menus in the browser. Selection of a given term searches neuroanatomical annotations for Gal4 lines, and activates a corresponding ROI that is used to conduct a spatial search of the image data.

Refining Gal4 reporter domains using Cre intersectional expression

We estimated the fraction of the brain labeled by each Gal4 line using a transgenic line with pan-neuronal expression of Cerulean driven by the *elavl3* promoter (*HuC: Cer*) to demarcate the extent of the central nervous system (*Supp. Fig. 2.4*). Together, the Gal4 lines included in the database cover 70.5% of the *HuC: Cer* pattern, thus providing experimental access to a substantial fraction of the larval brain. Each line expressed Gal4 in a mean of 1.9 % of the brain (median 0.85%), ranging from 0.018 % (*y352Et* in which brain expression is primarily driven in bilateral clusters of 10-12 neurons in the caudo-lateral medulla oblongata) to 25.1% (*y365Et* in which expression is

driven throughout the neuraxis). These numbers highlight the difficulty in obtaining sufficiently spatially restricted reporter or effector gene expression for functional studies using conventional single transgene approaches. We therefore performed a screen to recover brain-specific Cre enhancer trap lines that could be used with a *UAS:loxP-GFP-loxP-RFP (UAS:GR-switch)* transgene to further restrict the expression of a Gal4 activated reporter.

We screened for Cre enhancer trap lines using RFP fluorescence from a *Tg(actb2:loxP-eGFP-loxP-ly-TagRFPT)y272 (βactin:Switch)* transgenic line [40] and recovered 30 lines after screening 113 founders. We selected 9 lines with strong brain expression for high resolution imaging. To register the expression pattern of Cre lines to the same reference space used for our Gal4 lines we used a modification of the pipeline described above. Double transgenic enhancer trap Cre, β actin:Switch fish were crossed to the *HuC: Cer* transgenic line. We co-imaged Cerulean and TagRFPT fluorescence, then registered each image stack to the averaged representation of *HuC: Cer* that had been previously transformed onto the *vglut2a:DsRed* reference brain. This enabled us to produce average representations of Cre enhancer trap lines, that could be directly compared with the expression of the Gal4 enhancer trap and transgenic lines previously imaged (**Fig. 2.5**).

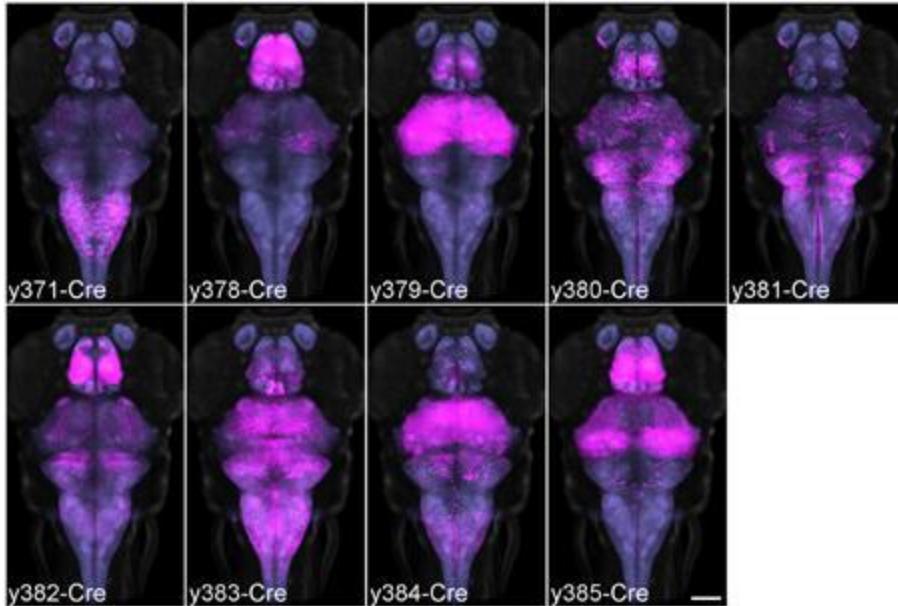


Figure 2.5. Average brain representations of Cre enhancer trap lines.

Maximum projections through the 9 Cre enhancer trap lines imaged for this study. Each line was visualized using the *beta-tubulin:Switch* transgenic line and scanned with *HuC: Cer* in order to register the pattern to the database. At least three brains were scanned and averaged for each line (magenta). Background: ubiquitous *beta-tubulin:Switch* (gray) and pan-neuronal *HuC: Cer* (blue, after brain mask applied). Scale bar 100 μm .

We then used the browser to predict *UAS:GR-switch* reporter expression in crosses between specific Cre and Gal4 lines, by selectively highlighting pixels that contained both Cre and Gal4 expression. Because of our interest in startle modulation, we focused on Gal4 enhancer trap line *y252Et* which labels neurons that regulate startle responses [31]. Two Cre lines (*y371Et* and *y385Et*) differently intersected the expression of Gal4 in *y252Et*, predicting that reporter expression would be constrained to distinct cell populations in triple transgenic larvae. In *y371Et*, Cre expression is confined to part of the medulla (**Fig. 2.6A**). Imaging of *y252-Gal4*, *y371-Cre*, *UAS:GR-switch* larvae

revealed that RFP fluorescence was also constrained to the medulla, consistent with the expected co-expression domain of Gal4 and Cre (**Fig. 2.6B,C**). Conversely, in enhancer trap line *y385Et* Cre is most prominently expressed in the midbrain and forebrain (**Fig. 2.6D**) and accordingly *y252-Gal4*, *y385-Cre*, *UAS:GR-switch* larvae showed RFP fluorescence in the thalamus, with additional scattered RFP+ neurons present in the medulla as well (**Fig. 2.6E,F**). Intersectional methods such as these will be essential for highly targeted reporter gene expression and these results further emphasize the value of integrating transgene expression patterns into a unified coordinate system.

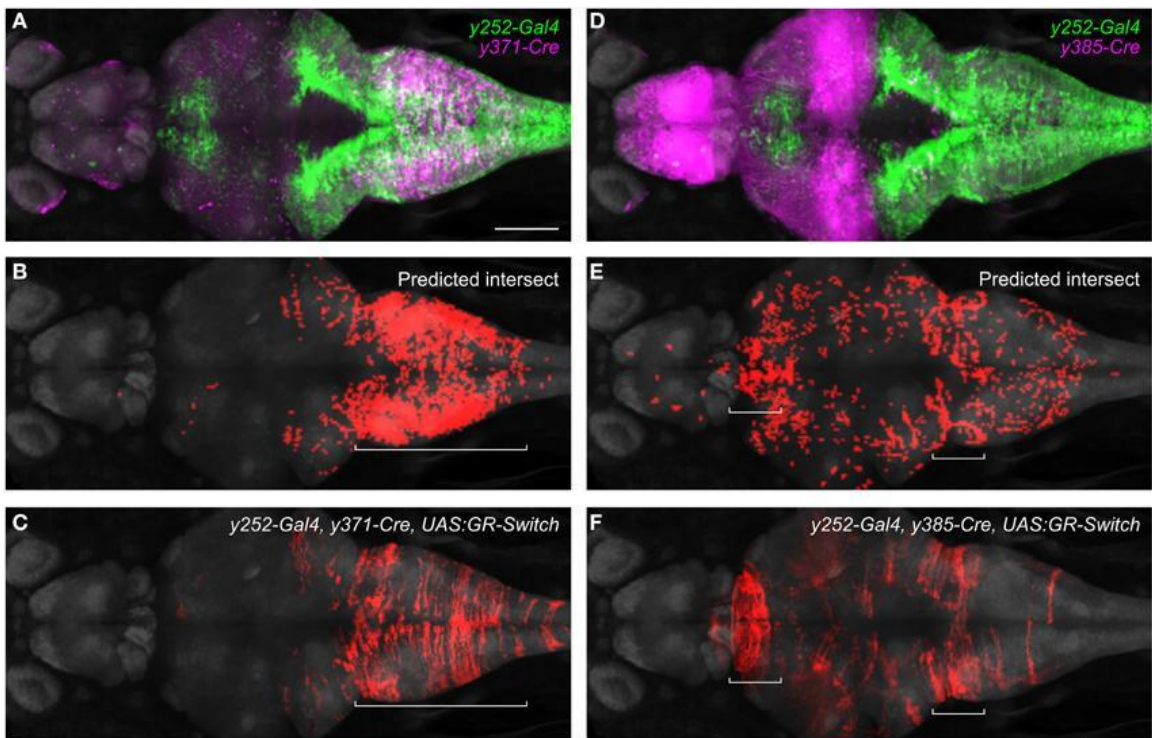


Figure 2.6. Intersectional control of reporter gene expression in neurons expressing both Gal4 and Cre.

(A) Expression patterns of *y252-Gal4* and *y371-Cre* superimposed using the brain browser. Scale bar 100 μm . (B) Predicted region of co-expression for *y252* and *y371* based on co-localization of strongly fluorescent pixels (red). (C) Actual region of co-expression of Gal4 and Cre in *y252-Gal4*, *y371-Cre*, *UAS:GR-Switch* embryos. Both predicted and actual expression is primarily confined to the median and caudal medulla. (D–F) Similar analysis using *y252-Gal4* and *y385-Cre* in which very strong Cre expression is detected in the forebrain, and weaker Cre expression is observed in the medulla. Both predicted and actual expression is seen in these regions, along with sparse labeling in additional brain regions.

Suppressing non-neuronal expression using microRNA

The majority of the enhancer trap Gal4 and Cre lines in this data set were generated using a vector that strongly enriches for brain-specific expression by inclusion of neuronal-restrictive silencing elements [22]. However, many additional lines are available which contain valuable patterns of expression in the brain accompanied by expression in non-neuronal tissue. Such lines would be of greater utility if the expression outside the brain could be suppressed. We speculated that the addition of specific microRNA target sequences to the 3' untranslated region of a UAS:reporter transgene would attenuate reporter expression outside the brain, allowing for broader use of these Gal4 lines than is currently possible.

MicroRNAs are short hairpin RNA molecules that can greatly reduce the expression of genes with cognate target sequences in the 3' UTRs of their messenger RNA. While each target site in an mRNA may reduce expression by as much as 50-80 %, strongly repressed mRNAs typically contain several target sites in their 3' UTR [41].

Many microRNAs are robustly expressed in a tissue specific manner outside the nervous system. We therefore speculated that modifying the 3' UTR of a UAS:reporter transgene to incorporate multiple target sequences for non-neuronal microRNAs, may lead to reduced expression outside the brain. In zebrafish, microRNA miR-1 is highly expressed in muscle, with little to no expression in the nervous system [42]. Similarly, miR-126 is expressed in heart and miR-199 in epidermis and skeleton, both with minimal neural expression [42]. We constructed a *UAS:epNTR-TagRFPT* reporter vector, which comprises a fusion of enhanced-potency nitroreductase to TagRFPT followed by the ocean pout antifreeze protein 3' UTR, which we modified to include miR-1, miR-126 and miR-199 target sites (utr.zb1). Reporter expression was strongly suppressed in both slow and fast muscle but remained in the heart and epidermis (**Fig. 2.7A ; Supp. Fig. 2.5**). To reduce cardiac expression, we made a new 3' UTR (utr.zb2) incorporating additional target sites for miR-499 which is highly expressed in the heart [43]. Transgenic larvae with the utr.zb2 showed suppression of reporter expression in the heart in addition to the suppression in muscle observed with utr.zb1. As these larvae retained reporter expression in skin, we added target sequences to the 3' UTR for miR-203a which is expressed in epidermis [42]. Transgenic *Tg(UAS:epNTR-TagRFPT-utr.zb3)y362* larvae with this 3' UTR (utr.zb3 ; Supp. Fig 6) showed a strong reduction in expression in muscle, heart and skin with no apparent reduction in brain expression (**Fig. 2.7A,B**). Accordingly, we anticipate that utr.zb3 will expand the usefulness of a wide range of existing Gal4 lines.

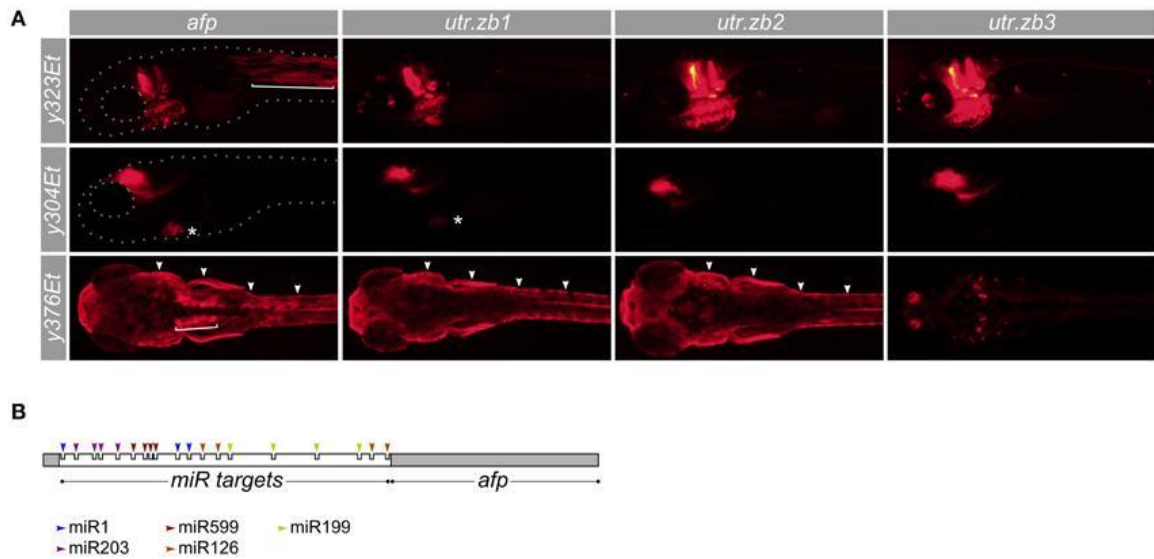


Figure 2.7. Suppression of non-neuronal expression using synthetic 3' untranslated regions.

(A) Development of synthetic utr-zb3 for suppressing Gal4 reporter expression in muscle, skin and heart. We used Gal4 enhancer trap lines *y323Et*, *y304Et*, and *y376Et* to drive expression in muscle (bracket), heart (asterisk), and skin (arrowheads) respectively—each of these lines also drives expression in the brain. The full pattern of expression is seen using a *UAS:epNTR-TagRFPT* reporter which has a standard ocean pout anti-freeze protein (*afp*) 3' UTR (left panels). Replacing the *afp* with utr-zb1 eliminates muscle but not heart or skin expression. Similarly utr-zb2 additionally eliminates cardiac expression and utr-zb3 suppresses expression in muscle, heart and skin. (B) Schematic of the 3' untranslated region in utr-zb3. MicroRNA sites are placed at the beginning of the 3' UTR, ahead of the *afp* sequence.

Discussion

Binary transgenic expression systems such as Gal4/UAS are powerful tools for dissecting neuronal circuitry and consequently, enhancer trap screens have provided the zebrafish community with many valuable Gal4 lines. Here we offer a solution to a practical obstacle to working with Gal4 lines: the difficulty in finding a line that labels a specific population of neurons. The 80 Gal4 lines presented in this database were

registered onto a common reference brain, and, using our browser software, can be easily searched to identify a line that labels a specific brain region.

The pipeline we have established for registering brains into a common reference space produces average brain images that are accurate to around one cell diameter, which is similar to the accuracy achieved by two other large-scale confocal registration projects in larval zebrafish [2,4]. Because our confocal images were acquired from a single orientation, there is pronounced fluorescence attenuation in the Z-dimension due to effects of absorption and light-scattering. For example, the resolution in our image stacks is notably less clear in the hypothalamus, than in dorsal regions such as the tectum. This problem was addressed in an earlier study in zebrafish that developed ViBE-Z software for image registration [2]. ViBE-Z achieves highly accurate reconstruction of brain expression by combining a light attenuation model with dual high and low intensity brain scans at four positions, and thus requires significant imaging time per embryo. In addition, ViBE-Z was limited to 2-4 dpf brains, whereas most larval zebrafish behavioral studies are performed at 5-7 dpf. Thus, as for the Z-Brain database [4], we imaged larvae at 6 dpf. Whereas Z-Brain used antibody staining in fixed tissue, our pipeline used live imaging of fluorescent transgenic reporters. Although we recognize that live imaging limits the scope of available markers, it avoids artifacts associated with fixation and staining and increases throughput. Indeed, by employing an optimized scanning protocol that required only two image stacks per embryo, image acquisition time for each transgenic line (for the minimum of 3 larvae) was 120 min, and using a parallel

computing resource, an additional 60 min for image processing. An additional strength of Z-Brain is an extensive effort at manual segmentation of neuroanatomical regions, which facilitates annotation. Our preliminary studies suggest that by imaging larvae co-stained for multiple reference channels (e.g., DsRed and total ERK in *vglut2a:DsRed* larvae) it is feasible to align expression data acquired from live imaging and immunostaining. Thus data from independent registration projects performed at the same developmental stage may be merged, and take advantage of the complementary strengths of different approaches.

The brain browser software provides a simple way to identify enhancer trap Gal4 lines that label a specific 3-dimensional region of the brain. To assist with this, the current data set includes 20 transgenic lines that were generated with defined promoters or BAC transgenesis that reproduce known neuroanatomical expression patterns of specific genes. These lines provide landmarks for interpreting expression patterns in the enhancer trap lines, as illustrated above by the use of ventral medulla *vglut2a:DsRed* expression to identify Gal4 lines that label the inferior olive. The database we present is easily extendable: new lines can be added simply by copying registered image stacks to the browser data directory and manually annotated within the browser. The browser can search the neuroanatomical annotations, using terms from the zebrafish anatomical ontology. For several search terms (e.g., inferior olive) we have generated a mask that is additionally used to conduct a spatial search for lines with fluorescence in the corresponding region. Such masks are ROIs that can be created from within the browser

and can be easily generated by users of the software, providing the possibility of expanding and refining spatial annotation as more detailed neuroanatomical information becomes available [4].

A major impetus for this work has been our effort to conduct circuit breaking screens in larval zebrafish. Circuit breaking, or 'neurotrapping' screens which use libraries of Gal4 lines to inactivate cohorts of neurons are a standard method in *Drosophila* for identifying behaviorally relevant circuitry [44,45]. Such screens are also feasible in zebrafish [31], however they require maintaining a large number of transgenic lines. In principle, a more systematic screen for behaviorally relevant neurons could be performed, by using a small set of transgenic lines with non-overlapping expression patterns that together would target every neuron in the brain. A hit from this initial set could then be interrogated using either a second set of Gal4 lines that subdivide the initial expression domain or by using Cre lines that further constrain reporter expression. To facilitate testing of a 'nested' set of lines, the brain browser can automatically delineate a set of lines that together, subdivide the expression domain of any given selected line. For instance, using the HuC:Cre transgenic line image as a template, the browser identifies a set of 8 lines that together express Gal4 in 50% of the brain with minimal overlap. This set of lines may be a valuable starting point for screening lines with a functional role in behavior. An important caveat is that while neurons labeled in most enhancer trap lines show reproducible overall morphologies, the actual locations of specific cells may differ between individuals. Thus in some cases enhancer trap lines that appear to overlap in a

discrete brain region may nevertheless label closely intermingled but distinct neuronal cell types. Thus, while computational predictions of overlapping expression may be useful for selecting transgenic lines, they will require empirical validation.

Transgenic technologies alone do not yet enable neuroscientists to interrogate the nervous system on a cell-by-cell basis. Most transgenic lines have expression in thousands of cells, and more often than not, this expression is not limited to the nervous system. This study provides partial solutions to these two problems. We confirm that Cre enhancer trap lines can successfully constrain Gal4 expression domains, and have designed a novel UAS transgenic line that suppresses reporter expression in heart, muscle and skin. Using the *UAS:GR-switch* reporter, the Cre enhancer trap lines presented here enable Gal4 expression domains to be limited to cells co-expressing Cre and Gal4. With a larger set of Cre lines, obtained by further screening or incorporation of existing resources [46], Gal4 expression domains may be more systematically subdivided.

Robust expression outside the brain limits the experimental utility of many enhancer trap lines. Previously, we attempted to address this by constraining transgene expression to the nervous system through the incorporation of neuronal restrictive silencing elements (NRSEs) [22]. Indeed, by incorporating two NRSE motifs (the REx2 element) into our Gal4 enhancer trap vector, we achieved a 5-fold increase in the recovery of enhancer trap lines with brain-specific Gal4 expression. While this approach allows for the generation of new brain-specific enhancer trap lines, there are many existing Gal4 lines with extremely useful expression patterns in the brain that are

accompanied by strong expression in non-neuronal tissue. To better utilize existing Gal4 lines that lack NRSEs, we attempted to make a brain-specific Gal4 reporter by incorporating the REx2 element into the promoter or intron of a UAS:mCherry transgene. Unfortunately, this was ineffective at suppressing non-neural mCherry expression. Here we describe a different strategy to reduce UAS reporter expression outside the brain, by constructing a synthetic 3' untranslated region that contains target sites for microRNAs that are strongly expressed in muscle, heart and epidermis. Several microRNAs have been reported that are strongly expressed in these tissues with low or undetectable expression in the larval brain. By incorporating 3-4 target sequences for each such microRNA into the 3' untranslated region of a UAS reporter transgene, expression was strongly suppressed in heart, muscle, and epidermis. Importantly, expression in the brain was not also reduced. In contrast, we noticed an apparent increase in expression for the utr.zb2 and utr.zb3 containing transgenes, which we attribute to differences in the site of transgene insertion. This new method expands the usefulness of a wide range of existing Gal4 lines, enabling such lines to be used for ablation, bioluminescent imaging or optogenetic experiments. However expression is only suppressed in the specific cell-types that express high levels of the microRNAs that we selected at larval stages. Thus a limitation of our current best synthetic 3' UTR (utr.zb3) is that it does not suppress expression in the notochord and suppression in the heart is most robust after 5 dpf. We will continue to test microRNA target sequences that may more strongly and broadly suppress reporter expression outside the brain.

Current genetic methods already enable both non-invasive visualization and functional interrogation of neurons. However, further refinements of transgenic technologies will allow for more precise selective targeting of neuronal cell populations. The new Gal4 and Cre transgenic reporter lines described here, together with our browser software will therefore facilitate the use of zebrafish in mapping the neuronal circuits that control physiology and behavior.

Materials and Methods

Software and data availability

The transgenic brain browser is written as IDL runtime code and can run under the IDL Virtual Machine which is freely available (www.exelisvis.com). The software, reference brain, registered brain averages and epifluorescent images can be downloaded from our website (<https://science.nichd.nih.gov/confluence/display/burgess/Software>). Download and extract the zbb.zip file. Instructions for the operation of the browser are included in the download. Epifluorescent images and mapping data for enhancer trap lines are available at zfin.org

Animal husbandry

The Gal4 and Cre enhancer trap lines in this study were maintained on a Tübingen long fin strain background. Embryos were raised in E3 medium supplemented with 1.5 mM HEPES pH 7.3 (E3h) at 28°C on a 14h:10h light:dark cycle with medium changes at

least every 2 days. All in vivo experimental procedures were conducted according to National Institutes of Health guidelines for animal research and were approved by the NICHD animal care and use committee.

Transgenic lines

74 of the Gal4 enhancer trap lines described here were generated by our laboratory as previously described [22]. Briefly, either *cfos* or SCP1 basal promoter sequences were used together with the Gal4 variant Gal4ff. Most lines also included a sequence derived from juxtaposing two neuronal restrictive silencing elements (the REx2 motif) in order to restrict expression to the nervous system. Six additional Gal4 lines were recovered by chance: we observed a strong position effect while generating transgenic lines using the tryptophan hydroxylase and dopamine beta hydroxylase promoters [47], necessitating the screening of multiple founders to isolate a line with the expression pattern matching that of the endogenous gene. Lines with robust expression in the brain outside the expected domain are thus included as enhancer traps in this paper. Since most founder fish contained several *tol2*-mediated integrations that resulted in multiple overlapping patterns of expression, fish were outcrossed over at least four generations in order to isolate transgenic lines with single reproducible expression patterns that segregated in Mendelian ratios. Enhancer trap Gal4 expression patterns were maintained and visualized using the *Tg(UAS-E1b:Kaede)*s1999t* (UAS:Kaede)* reporter

line [11]. Other transgenic Gal4 fish were visualized using *Tg2(14xUAS:GFP)nns19* [48].

For the Cre enhancer trap screen, we used the REx2-SCP1 synthetic promoter that we previously created for Gal4 enhancer trapping [22], as a basal promoter for a fusion gene containing zebrafish-optimized (zf1) Cre and Cerulean linked by a porcine teschovirus-1 2A peptide to yield separate proteins (Cre.zf1-2a-Cer.zf1) [40,49]. The *REx2-SCP1:Cre.zf1-2a-Cer.zf1* cassette was placed in a mini-tol2 backbone [50] and injected with tol2 to generate founders. Some additional Cre lines were based on a modification of this vector, where we added 60 bp attP sites flanking the transgene cassette (inside the tol2 arms) [51]. In principle the presence of attP sites will enable the Cre trap to be replaced by another reporter using PhiC31 recombinase-mediated cassette exchange [52], similar to the InSite system used in *Drosophila* [53], however we have not yet tested the efficiency of reporter replacement. We initially screened for founders using the Cerulean protein in the vector; however, this was not successful, presumably because the Cerulean fluorescence was in most cases too dim to detect with an epifluorescent microscope. Instead, we screened and maintain lines using the *βactin:Switch* transgenic line (*Tg(actb2:loxP-eGFP-loxP-ly-TagRFPT)y272*) previously described [40].

The plasmid used to make *Tg(elavl3:ubci-Cer-sv40)y342 (HuC:Cer)* uses a 3.1 kb fragment from the elavl3 promoter [54,55] to drive pan-neuronal expression of Cerulean fluorescent protein and includes the ubiquitin C intron for stronger expression [40]. As the optimized woodchuck hepatitis virus post-transcriptional element (oPre) does not

increase expression levels in zebrafish [40], we used inverse PCR to remove oPre from the *UAS:BGi-epNTR-TagRFPT-oPre* plasmid which contains enhanced-potency nitroreductase (epNTR) fused to TagRFPT and the rabbit β -globin intron (BGi) for stronger expression [29]. We then generated a new transgenic line for ablation studies *Tg(UAS-E1b:BGi-epNTR-TagRFPT)y361*. To target noradrenergic neurons, we isolated a 3007 bp fragment from the dopamine beta-hydroxylase gene, including promoter and first exon up to the ATG (chr10:10572957-10575963) from BAC.CH211-270H11, which we subcloned into pT2MCSkG4FF [22], then used tol2 transgenesis to generate founders. *Tg(-3.0dbh:Gal4ff)y360* shows expression in the dorsal caudal hindbrain consistent with the position of noradrenergic neurons of the vagal area [56]. To make the *UAS:BGi-lox-emGFP.zfl-lox-lyn-TagRFPT-afp* plasmid, we PCR amplified codon optimized emerald GFP (emGFP) [31], adding loxP sites and recombined the product into *UAS:BGi-lynTagRFPT* [47] using SLiCE [57]. This plasmid was injected with tol1 transposase to make the line *Tg(UAS:BGi-loxP-eGFP.zfl-loxP-lyn-TagRFPT)y363 (UAS:GR-Switch)*. *Tg(evx2:Gal4)nns52* and *Tg(shox2:Gal4)nns51* lines were generated by CRISPR/Cas9-mediated knock-in [58] using donor constructs that either contained (*evx2:Gal4*) or did not contain the hsp70 promoter (*shox2:Gal4*). A target sequence for sgRNA of GGGGCTCGCGGTGAGGGAAGG (-78~-90) was used for *evx2:Gal4*, while GGCGGCAGCTGAGCTGAATGCGG (+274~+276) was used for *shox2:Gal4*.

Other transgenic lines used were: *Tg(tph2:Gal4ff)y228* [47], *Tg(-3.2fev:EGFP)ne0214 (pet1:GFP)* [59], *TgBAC(slc17a6b:loxP-DsRed-loxP-GFP)nns14*

(*vglut2a:DsRed*) [36], *Tg(slc6a3:EGFP)ot80 (dat:GFP)* [60], *Tg(kdr:GFP)la116 (flk:GFP)* [61], *Tg(ato7:GFP)rw021 (ath5:GFP)* [62], *Tg(gfap:GFP)mi2001 (gfap:GFP)* [63], *Tg(slc6a5:GFP)cf3 (glyt2:GFP)* [64], *Tg(-17.6isl2b:GFP)zc7 (isl2b:GFP)* [65], *Tg(phox2b:EGFP)w37 (phox2b:GFP)* [66], *TgBAC(vsx2:Gal4ff)nns18 (chx10:Gal4)* [48], *Tg(eng1b:Gal4)nns40 (eng1b:GFP)* [58], *TgBAC(gsx1:GFP)nns32 (gsx1:GFP)*, *TgBAC(gad1b:GFP)nns25 (gad1b:GFP)* [20] and *Gt(T2KSAG)j1229* [28].

Imaging

Lines included in our database were crossed to *vglut2a:DsRed*, which broadly labels glutamatergic neurons throughout the brain [36,67], providing a suitable channel for image registration. Embryos from these crosses were raised in E3h media containing 300 μ M N-Phenylthiourea (PTU) starting at 8 to 22 hours post fertilization (hpf) to suppress melanophore formation and sorted for fluorescence at 2 days post fertilization (2 dpf). An inverted laser-scanning confocal microscope (Leica TCS SP5 II) equipped with an automated stage and 25x / 0.95 numerical aperture apochromatic water immersion lens (Leica # 11506340) was used to acquire confocal stacks of transgenic fish and immunofluorescently labeled samples. Live larvae were anesthetized in 0.24 mg/mL tricaine methanesulfonate (MS-222) for 3 minutes prior to mounting at 6 dpf. Live or fixed embryos were then mounted in 2.5% low melting point agarose placed in a 3D printed ABS 4-well plastic insert (Stratasys uPrint) within a cell culture chamber with a number 1.5 thickness (0.17 +/- 0.005 mm) cover glass bottom (Lab-Tek II 155379). A

488 nm argon laser line and a 561 nm diode-pumped solid state (DPSS) laser were used to excite fluorophores with images acquired as serial sections along the z-axis at 2.0 μm intervals between dorsal and ventral surfaces of the brain in a 1 x 2 tiled array to visualize the brain and a portion of the spinal cord. To shorten scan duration and allow for laser compensation over the z-dimension, channels were acquired simultaneously at a 1 x 1 x 2 μm ; xyz pixel spacing. Laser illumination was increased via acousto-optic tunable filter with z-position to counter attenuation with ramp points set every $\sim 70 \mu\text{m}$. Fluorescent emission from the 488 nm excitation was collected with a hybrid detector with a spectral window of 500-550 nm and emission from the 561 nm excitation collected by a second hybrid detector set at 571-700 nm. In order to minimize the cross-channel contamination present between imaged fluorophores, dye separation was performed in the Leica acquisition software (Leica Application Suite - Advanced Fluorescence, LAS AF) with coefficients based on published spectra of imaged fluorophores and the spectral windows used for acquisition. Resulting rostral and caudal stacks were stitched together [68] and channels split in Fiji [69] prior to registration.

Registration

The Computational Morphometry Toolkit (CMTK) `convertx`, `registrationx`, `warpx`, `reformatx`, `average_images`, and `levelset` commands were used to process and register image stacks (<http://www.nitrc.org/projects/cmtk/>). As reference choice can impact the quality of registration, we used the normalized cross-correlation (NCC)

between duplicate scans of the brains from a 'calibration set' (i.e., two *tph2:Gal4* and two *y307Et* larvae) to identify the best performing reference as well as optimal registration parameters. We reasoned that successive scans of the same fish, initially and following removal and remounting, would approximate the ideal registration case (i.e., alignment of an identical underlying pattern), and that use of the best reference and optimal registration parameters should maximize the NCC. As potential optimal reference brains, we tested the *vglut2a:DsRed* channels from the scans of 255 enhancer trap and transgenic fish as well as iteratively shaped averages derived from the top 5, 10, and 20 performing channels.

We first registered all 8 scans (i.e. the two scans for each of the four fish in the calibration set) to each potential reference brain. Then, for each reference brain, we computed the NCC for both the *vglut2a:DsRed* channel and the Gal4/Kaede channel for all four calibration larvae (i.e. the first DsRed scan versus the second DsRed scan for fish #1, the first Kaede scan versus the second Kaede scan for fish #1, etc for a total of eight comparisons per reference brain). We then ranked reference brains by the mean of the four NCCs for the *vglut2a:DsRed* comparison (Supp Fig 1A) and the mean NCC for the Gal4/Kaede comparison (Supp Fig 1A'). As expected, the *vglut2a:DsRed* average NCC and the Gal4/Kaede average NCC were correlated (not shown). In computing the NCC for the *vglut2a:DsRed* channel, we were able to calculate a more stringent NCC by excluding pixels outside the expression pattern, by using the reference brain *vglut2a:DsRed* pattern as a mask. This procedure, however, could not be applied to the

Gal4/Kaede channel because the Gal4/Kaede expression does not overlap entirely with the *vglut2a:DsRed* pattern. Therefore the NCC values in *Supp. Fig. 2.1A'* are not masked. Averaged brains performed worse than their constituents (*Supp. Fig. 2.1A*). The specific reference brain chosen for all subsequent registrations had the highest rank among the 255 *vglut2a:DsRed* brains, was 9th ranked for Kaede comparisons, and was close to symmetrically oriented in horizontal and transverse sections.

Next, we used the calibration set to systematically test and identify parameters that yielded the most accurate registrations (e.g., *Supp. Fig. 2.1B*) while minimizing computation time when the impact on accuracy was negligible (e.g., *Supp. Fig. 2.1C & D*). Parameters were adjusted in isolation and the NCCs and walltimes. A full list of the settings we tested and the parameters we recommend for registration of similar confocal stacks with *vglut2a:DsRed* as a reference are listed in *Suppl. Table 3*.

For registrations using *vglut2a:DsRed* as a reference, "--dofs 12 --min-stepsize 1" was used for the initial rigid alignment while "--fast --grid-spacing 100 --smoothness-constraint-weight 1e-1 --grid-refine 2 --min-stepsize 0.25 --adaptive-fix-thresh 0.25 " was used for the subsequent nonrigid registration. For Cre enhancer trap lines, *HuC:Cre* was used as the reference pattern for registration instead. For these registrations, the same rigid parameters were used (i.e., "--dofs 12 --min-stepsize 1") while "--fast --grid-spacing 100 --smoothness-constraint-weight 1e-1 --grid-refine 0 --min-stepsize 0.25 --adaptive-fix-thresh 0.25 " was used for the *HuC:Cre* nonrigid registration. For the intersection of Cre lines to *y252*, the *y252* mean was used as a reference and a rigid

registration was performed without an additional nonrigid component. Resulting image stacks were normalized and averaged using the `average_images` command. To mask images, an initial mask was generated with CMTK's `levelset` command from binarizations of the mean of the *HuC:Cer* and *vglut2a:DsRed* scans. This initial mask was then manually expanded to encompass regions with weak *HuC:Cer* transgene expression such as the retina and pituitary and refined in order to minimize the inclusion of skin and other non-neural tissue in problematic lines. For example, lines with weak fluorescence required higher laser levels which often resulted in greater reflectance from skin. Finally, we linearly adjusted pixel intensities to saturate the top 0.01% of pixels in each averaged image stack for visualization and analysis.

Annotation

Neuroanatomical annotation was based primarily on Mueller and Wullimann [38], using the *HuC:Cer* and *vglut2a:DsRed* transgenic line channels in the brain browser as anatomical references. Due to the nature of transgene expression patterns, in some cases, patterns may be broader than the corresponding neuroanatomical region annotated. We used terms from the Zebrafish Anatomical Ontology where possible, supplemented by more up to data terminology where available [70,71].

Synthetic 3' UTR constructs.

To make *utr.zb1*, we designed a DNA fragment with target sequences for miR1-3p, miR126-3p and miR199-5p. MicroRNA targeting is primarily driven by the 7 bp seed sequence, however context outside this region may influence pairing [24]. For each microRNA, we therefore used TargetScanFish (release 6.2) [72] to identify an endogenous zebrafish transcript with a 3' UTR enriched in its predicted target sequences: respectively *tagln2* (miR1), *clcn6* (miR126) and *BX927290.1* (miR499). Regions of each gene's UTR that contained multiple microRNA targets were combined into a single 472 nucleotide sequence, which we then edited to remove all other microRNA targets and to make synthesizable. We synthesized this sequence as a gblock (IDT) and cloned it into the *HpaI* site in the ocean pout antifreeze protein 3' UTR contained in *UAS:BGi-epNTR-TagRFPT*. This was used to make *Tg(UAS:BGi-epNTR-TagRFPT-utr.zb1)* using toll transgenesis using *toll.zf1* mRNA [40,73]. For *utr.zb2* we searched TargetScanFish for a 3' UTR enriched in target sequences for miR-499-5p, which is strongly expressed in zebrafish heart [43]. We synthesized a 68 nucleotide fragment from the *shroom1* gene, edited it to remove other microRNA targets and cloned it into *UAS:BGi-epNTR-TagRFPT-utr.zb1*. This was used to make *Tg(UAS:BGi-epNTR-TagRFPT-utr.zb2)*. Next we added target sequences for miR-203a-3p, which is strongly expressed in zebrafish epidermis [42]. A 105 nucleotide sequence with multiple miR203 targets was copied from the *dntt* gene 3' UTR, and cloned into *UAS:BGi-epNTR-TagRFPT-utr.zb2* (see

Supp. Fig. 2.6 for the annotated sequence of *utr.zb3*). The resulting plasmid was used to make *Tg(UAS:BGi-epNTR-TagRFPT-utr.zb3)y362*.

Transgene insertion site mapping. Insertion site mapping for Gal4 enhancer trap lines was performed as described previously [32] with the following modifications. Genomic DNA was digested with *Mse*I and *Bfa*I and barcoded linkers ligated to digested products. The first round of PCR was performed using Tol2 ITR primer 5'-AATTTTCCCTAAGTACTTGTACTTTCACCTTGAGTAA and a linker primer 5'-GTAATACGACTCACTATAGGGCACGCGTG using cycle conditions:

95°C 120 s, 25 cycles of: 95°C 15 s, 55°C 30 s, 72°C 60 s. PCR amplicons from the first round were diluted 1:50 and a second round of PCR was performed using a nested Tol2 ITR primer: 5'-TCACTTGAGTAAAATTTTTGAGTACTTTTTACACCTC and nested linker primer 5'-GCGTGGTCGACTGCGCAT with cycle conditions: 95°C 120 s, then 20 cycles of: 95°C 15 s, 58°C 30 s, 72°C 60 s. Amplicons from the second round were pooled and the sequencing library was prepared for the Illumina Miseq sequencing platform. The insertion sites were mapped using GeIST mapping pipeline [74]. We then used Primer3 [75] to design primers against the flanking region (outside the sequence obtained by high throughput sequencing) and performed PCR to verify the insertion sites.

Supplementary Material

The Supplementary Material for this article can be found online at:

<http://journal.frontiersin.org/article/10.3389/fncir.2015.00078>

Supplemental Table 2.1. Neuroanatomical annotation and integration site mapping for Gal4 enhancer trap lines imaged as part of this study.

Annotations use terms from the zebrafish anatomical ontology, except where available terms are insufficiently specific. Lines which subjectively appear to most prominently label a single neuroanatomical structure are annotated as ‘selective’. Many lines include expression in retina and/or spinal cord. Because of the limitations of our confocal and epifluorescent analysis, we have not generally included further annotation of cells within these structures. We also provide limited annotation of structures outside the nervous system. Abbreviations: anterior lateral line ganglion, aLLg; nucleus of the medial longitudinal fasciculus, Nuc MLF; posterior lateral line ganglion, pLLg. Genes with accession numbers “ENS...” can be queried at Ensembl (<http://www.ensembl.org>). * Line y372Et contains a second linked integration in atp11a at Chr1:46822150.

Supplemental Table 2.2. Anatomical annotation for additional Gal4 lines with verified integration sites.

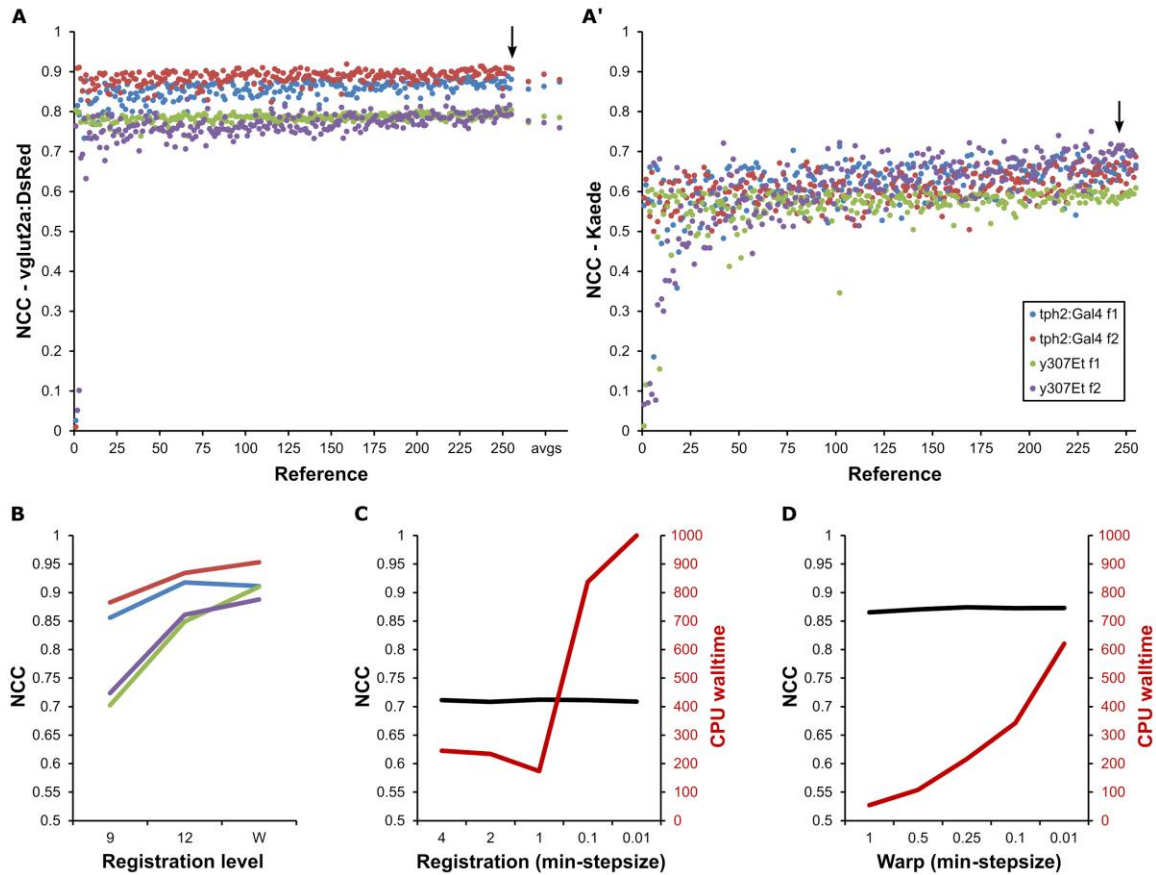
These lines were not used for high resolution imaging in this study. For each line, at least two lines of evidence support the integration site: either high throughput mapping and targeted PCR confirmation, or high throughput mapping and independent mapping data obtained using linker mediated PCR.

Supplemental Table 2.3. Summary of recommended CMTK parameters for registration of image stacks acquired using live vglut2a:DsRed fluorescence as the reference channel.

Parameters	Recommended	Rationale
registrationx		
--dofs	12	improved NCC
--max-stepsize	32	minimizes % failed registrations, but increases CPU time
--min-stepsize	1	reduces CPU time with negligible impact on NCC
--stepfactor	0.5 (default)	
--delta-f-threshold	0 (default)	

<i>--sampling</i>	1 (default)	
<i>--coarsest</i>	-1 (default)	
<i>--init</i>	--fov (default)	
<i>--registration-metric</i>	--nmi (default)	
<i>--interpolation</i>	--linear (default)	
warpx		
<i>--grid-spacing</i>	100	for reference dimensions ~1000 x 600 x 400 pixels
<i>--grid-refine</i>	2	
<i>--delay-refine</i>	no (default)	
<i>--ignore-edge</i>	0 (default)	
<i>--no-adaptive-fix</i>	no (default)	
<i>--adaptive-fix-thresh</i>	0.25	reduces CPU time
<i>--jacobian-constraint-weight</i>	0 (default)	
<i>--smoothness-constraint-weight</i>	0.1	maximizes inter-NCC / intra-NCC
<i>--inverse-consistency-weight</i>	0 (default)	
<i>--constraint-relaxation-factor</i>	-1 (default)	
<i>--max-stepsize</i>	-1 (default)	
<i>--min-stepsize</i>	0.25	reduces CPU time
<i>--stepfactor</i>	0.5 (default)	
<i>--delta-f-threshold</i>	0 (default)	
<i>--no-maxnorm</i>	no	
<i>--sampling</i>	1 (default)	
<i>--coarsest</i>	-1 (default)	
<i>--omit-original-data</i>	no	
<i>--accurate/--fast</i>	--fast	
<i>--registration-metric</i>	--nmi (default)	
<i>--interpolation</i>	--linear (default)	

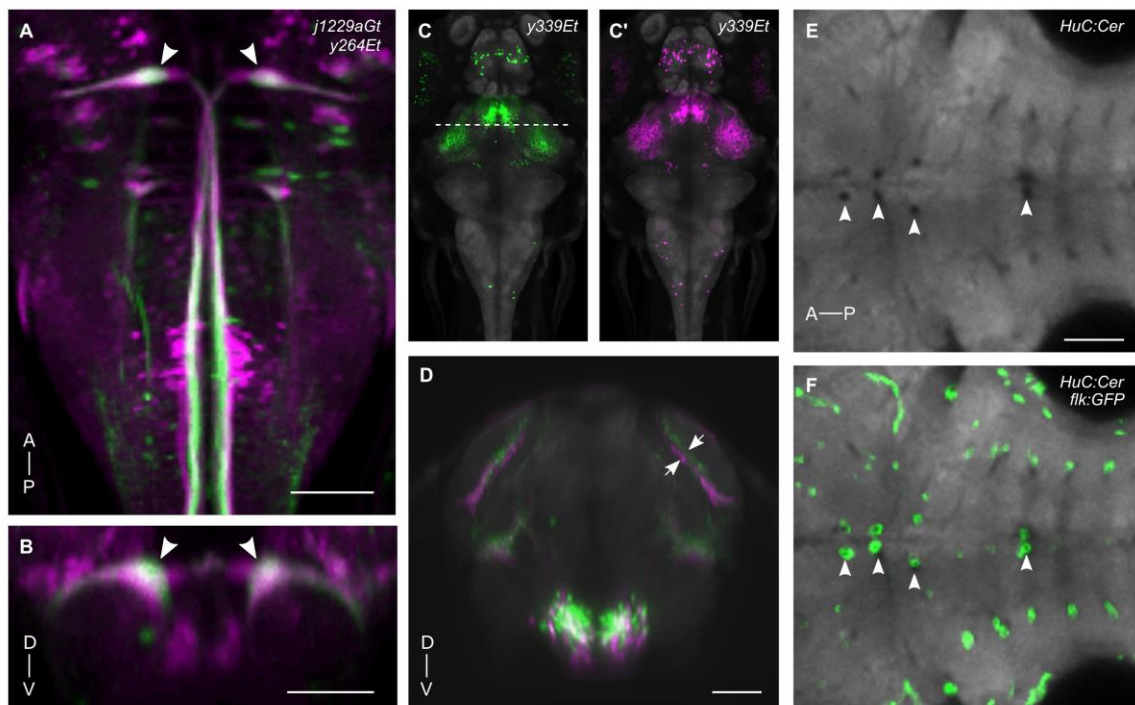
Supplemental Figure 2.1. Optimization of brain registration using CMTK.



(A) Normalized cross-correlation (NCC) for duplicate confocal scans of the vglut2a:DsRed channel in each of four brains in the calibration set (blue: tph:gal4 fish 1; red: tph2:gal4 fish 2; green: y307Et fish 1; purple: y307Et fish 2), after registration by full affine transformation to each of 255 vglut2a:DsRed expressing reference brains. Empty pixels were excluded from the computation using the reference brains as a mask. For each reference, the mean of the four NCCs was taken, and used to provide a rank (higher ranks to the right). In addition, the top 5, 10, and 20 reference brains (based on mean NCC) were used to generate iterative shaped averages (a5, a10, and a20 respectively) whose performance as a reference was also assessed. (A') NCC for the Gal4/Kaede channel from the same set of calibration and reference brains, however no mask was used before the NCC computation (see Methods). Arrows in (A,A') indicate the reference brain we selected to use for subsequent registrations. (B) Comparison of the average NCC of the calibration set using 9° of freedom rigid transformation (9: translation, rotation, and anisotropic scale), full affine transformation (12: translation, rotation, anisotropic scale, and shear), and affine plus warp transformation (W: translation, rotation, anisotropic scale, and shear), and affine plus warp transformation (W: translation, rotation, anisotropic scale, and shear), and affine plus warp transformation (W: translation, rotation, anisotropic scale, and shear).

translation, rotation, anisotropic scale, shear, and nonrigid). Line colors indicate larvae as in (A). While a number of registration parameters were optimized to maximize the average NCC of the calibration set (see Supplemental Table 3 for full list of tested and recommended parameters), a number of parameters showed no improvement in the average NCC of the calibration set, and so settings that minimized CPU walltime were selected instead. (C) Rigid registrations showed negligible improvement in NCC beyond a min-stepsize of 1 while greatly increasing the CPU time. Thus, a min-stepsize setting of 1 was used for registrations. (D) Nonrigid registrations showed negligible improvement in NCC beyond a min-stepsize of 0.25 while greatly increasing the CPU time. Thus, a min-stepsize setting of 0.25 was used for registrations.

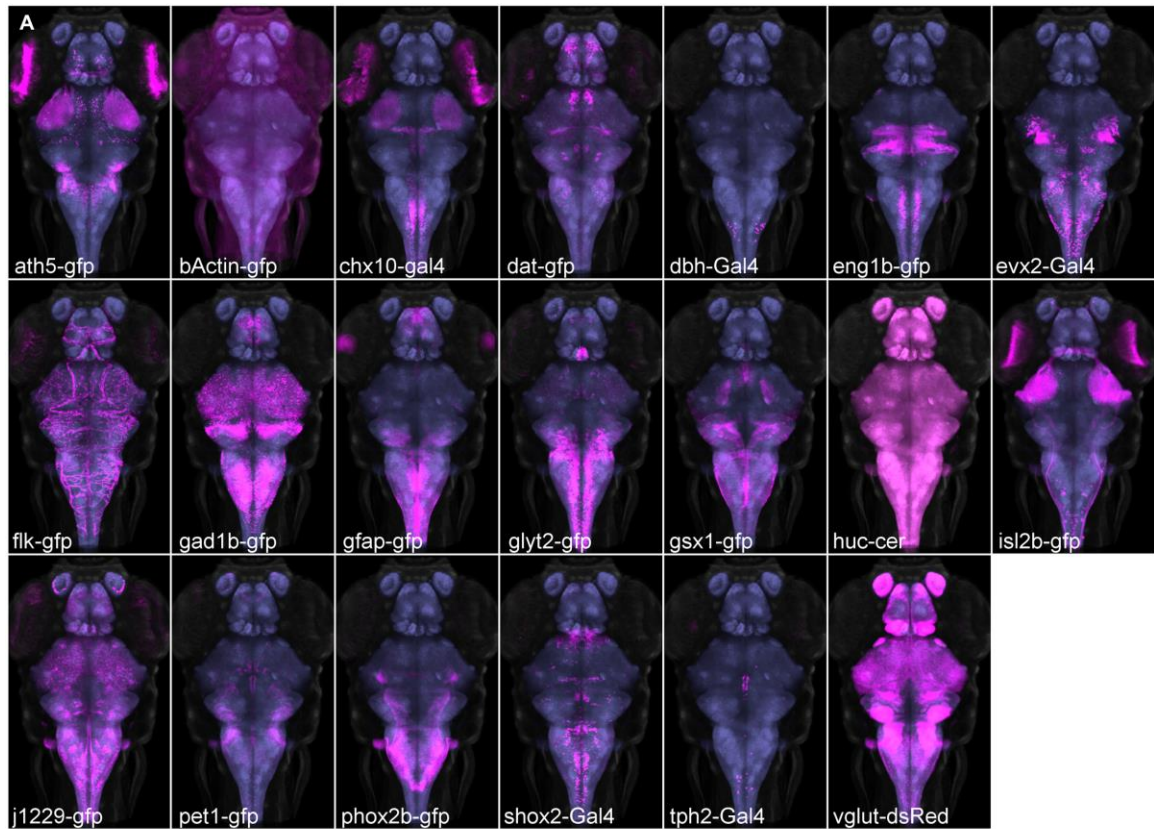
Supplemental Figure 2.2. Assessing registration accuracy by co-localized *Gal4* reporter gene expression.



Dorsal (A) and transverse (B) views of brain browser projections for enhancer trap line *y264Tg* (green) and transgenic line *j1229aGt* (magenta) in the region including the Mauthner cells (arrowheads). (C,C') Dorsal view of maximum projection of average representations of *y339Et*, made from two independent sets of three embryos each. Dotted line shows location of transverse slice shown in (D). (D) Slice through the midbrain and diencephalon of superimposed *y339Et* averages. In the right optic tectum, a neuropil layer (arrows) in the averages is misaligned by 1–2 cell diameters. (E) Horizontal view of a slice through the hindbrain from *HuC: Cer* average brain.

Arrowheads indicate gaps in the tissue lacking neuronal Cer expression. *flk:GFP* expression, which labels blood vessels, is superimposed in **(F)**. Anterior (A), Posterior (P), Dorsal (D), Ventral (V). All scale bars 50 μm .

Supplemental Figure 2.3. Transgenic lines providing neuroanatomical markers.

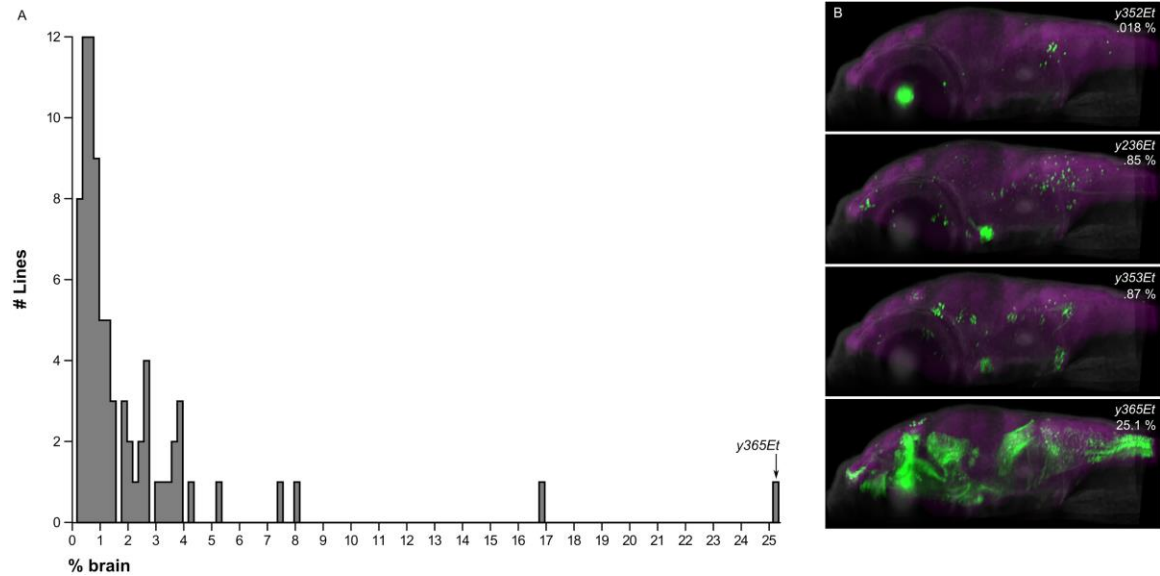


B	Line	Official designation	Marker for
	ath5-GFP	<i>Tg(ato7:GFP)rw021</i>	retinal ganglion cells
	bActin-GFP	<i>Tg(bActin:loxP-GFP-loxP-IynTagRFPT)y252</i>	ubiquitous
	chx10-gal4	<i>TgBAC(vsx2:Gal4ff)nns18</i>	medulla longitudinal stripe 2
	dat-GFP	<i>Tg(slc6a3:EGFP)ot80</i>	dopaminergic neurons
	dbh-Gal4	<i>Tg(-3.0dbh:Gal4ff)y360</i>	noradrenergic neurons
	eng1b-gal4	<i>Tg(eng1b:Gal4)nns40</i>	cerebellum, medulla glycinergic medial stripe 3
	evx2-gal4	<i>Tg(evx2-Gal4)nns52Tg</i>	medulla longitudinal stripe
	flk-GFP	<i>Tg(kdr:GFP)a116</i>	vasculature
	gad1b-gfp	<i>TgBAC(gad1b:GFP)nns25</i>	gabaergic neurons
	gfap-GFP	<i>Tg(gfap:GFP)mi2001</i>	glia
	glyt2-GFP	<i>Tg(slc6a5:GFP)cf3</i>	glycinergic neurons
	gsx1-gfp	<i>TgBAC(gsx1:GFP)nns32</i>	medulla longitudinal stripe 5
	huC-Cer	<i>Tg(elav13:ubci-Cer-sv40)y342</i>	pan-neuronal
	isl2b-gfp	<i>Tg(-17.6isl2b:GFP)zc7</i>	sensory neurons
	j1229-gfp	<i>Gt(T2KSAG)j1229</i>	Mauthner cell
	pet1-GFP	<i>Tg(-3.2fev:EGFP)ne0214</i>	serotonergic neurons
	phox2b-GFP	<i>Tg(phox2b:EGFP)w37</i>	vagal ganglia
	shox2-gal4	<i>Tg(shox2-gal4)nns51Tg</i>	medulla longitudinal stripe
	tph2-Gal4	<i>Tg(tph2:Gal4ff)y228</i>	superior raphe, serotonergic neurons
	vglut-dsRed	<i>TgBAC(slc17a6b:loxP-DsRed-loxP-GFP)nns14</i>	glutamatergic neurons

Maximum projections (A) and expression domains (B) of transgenic lines that were imaged as part of this study. Gal4 lines were visualized using *UAS:GFP* (magenta).

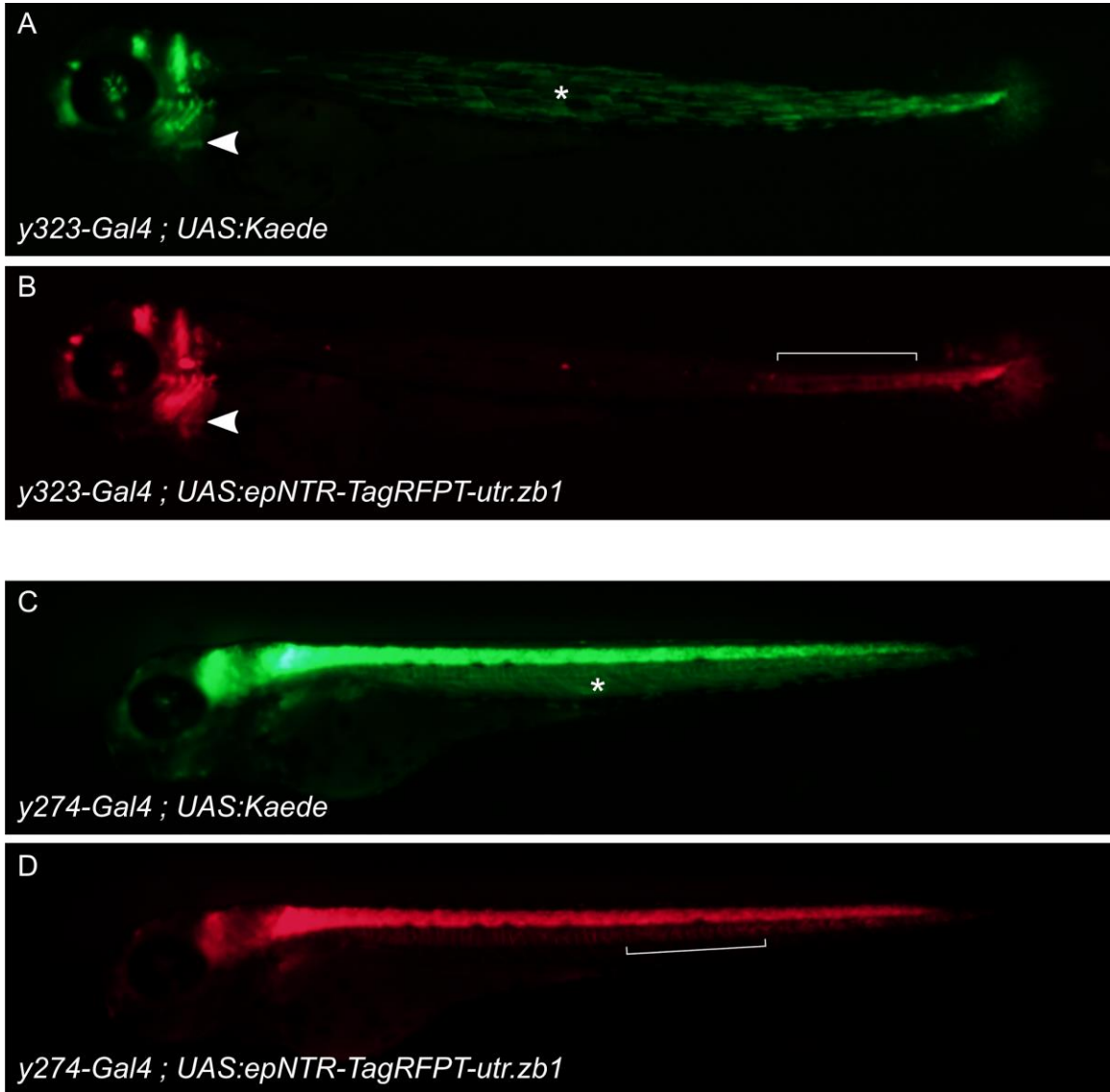
Background: ubiquitous *βactin:Switch* (gray) and pan-neuronal *HuC:Cer* (blue, after brain mask applied).

Supplemental Figure 2.4. Extent of brain expression in Gal4 enhancer trap lines.



(A) Histogram of the extent of brain coverage for the 80 Gal4 enhancer trap lines imaged in this study. (B) Sagittal hemi-projection for the line with the most restricted Gal4 expression pattern *y352Et*, for two lines with close to the median extent of Gal4 expression (*y236Et* and *y353Et*) and for the line with the broadest Gal4 expression pattern included in the database, *y365Et*.

Supplemental Figure 2.5. Synthetic 3' UTR *utr.zb1* suppresses transgene expression in muscle.



The synthetic 3' untranslated region *utr.zb1* reduces expression in both slow and fast muscle, but not in heart or notochord. Epifluorescence from Kaede (green) and TagRFPT (red) in *y323-Gal4, UAS:Kaede, UAS:epNTR-TagRFPT-utr.zb1* (**A,B**) or *y274-Gal4, UAS:Kaede, UAS:epNTR-TagRFPT-utr.zb1* (**C,D**) embryos imaged at 3 dpf. In *y323Et*, Gal4 is expressed outside the brain in slow muscle, notochord, heart and caudal fin. Slow muscle (**A**, asterisk) expression is suppressed by *utr.zb1* but expression in notochord (**B**, bracket), heart (arrowhead), and caudal fin remains intact. Similarly expression of Gal4

in fast muscle is suppressed by *utr.zb1* in *y274Et* (**C**, asterisk), but notochord expression (**D**, bracket) is not diminished.

```

at taagtctcagccaccggttGAGCAGGTGTTCCATACATTCCATTaaGATCTATTTCAgTT CATTTCAAgTC
AATTAATTTCAgCTCAAGTTTTTCATTTCATTTCA TTTCAAATAAAT TACATTCACCTAATTTCAgAT CAT
TTCAAATTggatcTTTAGCaCTGTAAAGTCTTAAATTTCACTCAGATTGGTCTTAAATGGTCTTAAGAGTCTTAAg
TTGATCTCAATTCTATTATGGCGCAGACAGACAT ACATTCCATTATcCTATTAcTAACATTCCA GAGAGTAT
CAGAATTTCAcGGTACGA TAATACCTCGATATGAATGGCACGGTACGCaACACATGAAGACCCACACTGGAG
GGAAACTATTCACATGCAC TCAgTGTGGAAAGAGTTTCAACTGATCAGCAAACCTTAATGAACACATAAAGA
TCCACACTGGTGTGAAAGAGTATATGTGCTTTAGTGTGAGAAGACTTTTATTACACCTCCAAATTC AAAAC
CACACCAGACGATTACACTGGAGAGACCGTACAAGTGTTCAAACaAGTGACAAGAGGTTTAAATCAGTTAACA
CATCTGAAAACACAAAAGAGGATTACACTGGACaagcTCAGAATcTCAcGGTACGA TcAaTCCaCGcTATG
AATcGCAcGGTACCaactgaacatgtcaaaaccgtggagactgttgagatttgatgtctgaaaagataa
agcctataaataaaaatggtgccc aaatttccctgcctgatgttttctttgtctttgctacatggctttgctg
ctcggatcggctcactctgtgtatgccacgttcaacttgtactctccttctcaggttaggtttattttt
agatgtgcagttagtttctgtgaaataaacacaccacacactgatattgtctgtgcattgacttggtgagtg
acattgtttttgatctgacatatattatattgattgatcaggtgaactgtgtgaaatcctaagtgctccata
cagatgttctgcatgaaaatattctcat tttat tagtggaagtgagtgtatgcca

```

Key

Grey lower case: Ocean pout antifreeze protein 3' untranslated region

Black/highlighted region: microRNA targets from zebrafish genes

- Match to full 8mer seed sequence
- Match to 7mer-1a
- Target regions for:

- dre-mir-1-3p
- dre-mir-203a-3p
- dre-mir-599-5p
- dre-mir-126-3p
- dre-mir-199-5p
- dre-mir-126-3p

Supplemental Figure 2.6. Annotated sequence of *utr.zb3*.

Chapter 3: High-precision registration between zebrafish brain atlases using symmetric diffeomorphic normalization

The work presented in this chapter has been edited for stylistic consistency and to conform with Graduate School guidelines, but has been published previously as:

Marquart GD, Tabor KM, Horstick EJ, Brown M, Geoca AK, Polys NF, Nogare DD, Burgess HA. High-precision registration between zebrafish brain atlases using symmetric diffeomorphic normalization. *GigaScience* (2017) gix056.

Abstract

Atlases provide a framework for spatially-mapping information from diverse sources into a common reference space. Specifically, brain atlases allow annotation of gene expression, cell morphology, connectivity, and activity. In larval zebrafish, advances in genetics, imaging, and computational methods now allow the collection of such information brain-wide. However, due to technical considerations, disparate datasets may use different references and may not be aligned to the same coordinate space. Two recent larval zebrafish atlases exemplify this problem: Z-Brain, containing gene expression, neural activity and neuroanatomical segmentations, was acquired using immunohistochemical stains, while the Zebrafish Brain Browser (ZBB) was constructed from live scans of fluorescent reporters in transgenic larvae. Although different references were used, the atlases included several common transgenic patterns that provide potential 'bridges' for transforming each into the other's coordinate space. We tested multiple bridging channels and registration algorithms and found that the symmetric diffeomorphic normalization (SyN) algorithm improved live brain registration

precision while better preserving cell morphology than B-spline based registrations. SyN also corrected for tissue distortion introduced during fixation. Multi-reference channel optimization provided a transformation that enabled Z-Brain and ZBB to be co-aligned with precision of approximately a single cell diameter and minimal perturbation of cell and tissue morphology. Finally, we developed software to visualize brain regions in 3-dimensions, including a virtual reality neuroanatomy explorer. This study demonstrates the feasibility of integrating whole brain datasets, despite disparate reference templates and acquisition protocols, when sufficient information is present for bridging. Increased accuracy and interoperability of zebrafish digital brain atlases will facilitate neurobiological studies.

Background

With a brain that contains an estimated 10^5 neurons, larvae are similar in complexity to adult *Drosophila*, another established neuroscience model. In both systems, researchers can deploy a wide range of genetic tools in efforts to decode patterns of neural structure and connectivity. In larval zebrafish, optical transparency and constrained physical dimensions (fitting within an imaging volume of 1000 x 600 x 350 μm) allow the entire brain to be rapidly scanned at cellular resolution using diffraction-limited microscopy. In principle, this enables researchers to systematically analyze effects of manipulations on a brain-wide level. However, such efforts have been hampered by the absence of a comprehensive digital atlas that would provide researchers

with a unified framework in which to aggregate data from different experiments and gain deeper insights from correlations between neuronal cell identity, connectivity, gene expression and function within the brain. Additionally, digital atlases may more clearly delineate structural boundaries that are difficult to accurately identify within individual brains, allowing for a more rigorous mapping of neuroanatomical regions onto experimental data.

These longstanding problems in zebrafish neuroscience have recently been addressed by the construction of digital atlases using 3-dimensional (3D) image registration techniques: the Virtual Brain Explorer for Zebrafish (ViBE-Z), Z-Brain and the Zebrafish Brain Browser (ZBB) [2,4,76]. In these atlases, information on gene expression, structure (neuronal cell bodies, glia, vasculature, ventricles, neuropil or axon tracts) and measures of activity (calcium or secondary messenger activity) are consolidated within a common spatial framework. By using widely-available transgenic lines or immunohistochemical stains as reference templates for brain alignment, each of these atlases provides other researchers the opportunity to register their own datasets into these digital spaces and take advantage of the information contained within.

ViBE-Z was the first comprehensive 3D digital brain atlas in zebrafish that used a nuclear stain for the alignment of 85 high resolution scans comprising 17 immunohistochemical patterns at 2-4 days post-fertilization (dpf) [2,27]. In ViBE-Z, custom algorithms were developed to correct for variations in fluorescent intensity with scan depth, and a

landmark approach taken to perform accurate image registration and segmentation into 73 neuroanatomic regions.

In contrast, two more recent approaches (Z-Brain and ZBB) have generated brain atlases at 6 dpf through non-linear B-spline registration using the freely available Computational Morphometry Toolkit (CMTK) [3,77]. Z-Brain includes 29 immunohistochemical patterns from 899 scans which form the basis for expert manual segmentation of the brain into 294 neuroanatomic regions. These partitions facilitate the analysis of phospho-ERK expression for mapping neural activity [2]. In Z-Brain, each expression pattern was co-scanned with tERK immunoreactivity, and registered to a single tERK-stained reference brain. For ZBB, we live-imaged 354 brains from 109 transgenic lines and manually annotated the expression found in each [76]. In place of tERK, a single *vglut2a:dsRed* transgenic brain was used as the reference in ZBB with transgenic lines crossed and co-imaged with this channel for registration. Brain browser software enables researchers to select a transgenic line labeling a selected set of neurons for monitoring and manipulating circuit function.

While Z-Brain and ZBB are powerful datasets on their own, we saw an opportunity to merge the two atlases because they are both based on confocal scans of 6 dpf larvae. This would bring to Z-Brain a large number of additional transgenic lines and to ZBB, the expert manual segmentation of Z-Brain. Several similarities between Z-Brain and ZBB suggested that bridging the atlases would be possible. First as zebrafish rearing conditions are standardized across laboratories and fish were imaged at the same time

post-fertilization, Z-Brain and ZBB likely reflect the same developmental timepoint. Second, images in both atlases were acquired at similar resolution ($0.8 \times 0.8 \times 2 \mu\text{m}$ for Z-Brain; $1 \times 1 \times 1$ or $1 \times 1 \times 2 \mu\text{m}$ for ZBB) and orientation (dorsal to ventral horizontal scans). Third, despite using distinct templates (tERK for Z-Brain and vglut2a for ZBB), Z-Brain and ZBB have several transgenic markers in common, which provide the possibility of bridging the datasets by using these shared patterns as references for a secondary registration step.

One of the strengths of larval zebrafish is the ability to rapidly image at cellular resolution and visualize brain-wide neuronal morphology, providing valuable information on cell type and potential connectivity. Z-Brain and ZBB both illustrate the feasibility of performing whole-brain registration with precision sufficient to ensure that the 'same' neurons from different fish are aligned to within a cell diameter ($\sim 8 \mu\text{m}$). However, a challenge for brain registration in zebrafish is to minimize local distortions, so that cellular morphology is preserved while still allowing sufficient deformation to overcome biological variability between individual brains or malformations due to tissue processing.

Here we describe a method to co-register ZBB and Z-Brain, bridging the two existing 6 dpf larval zebrafish brain atlases. By using the diffeomorphic algorithm SyN in the Advanced Normalization Tools (ANTs) software package [78,79], we were able to overcome differences in tissue shape due to fixation, optimize the trade-off between preservation of cell morphology and global alignment, and provide precise registration in

all tested brain regions. Additionally, ANTs provided superior image registration for live-scanned larvae, enabling us to improve the precision of registration and neuron morphology within our original ZBB atlas, allowing us to compile a new version with increased fidelity (ZBB_{1.2}).

Methods

Zebrafish lines

In order to provide additional options for bridging ZBB and Z-Brain, we scanned two transgenic lines that were not in the original ZBB release: *Et(gata2a:EGFP)zf81 (vmat2:GFP)* and *Tg(isl1:GFP)rw0 (isl1:GFP)* [80,81]. Other lines referenced in this study are *Tg(slc6a3:EGFP)ot80 (DAT:GFP)* [60], *Tg(-3.2fev:EGFP)ne0214 (pet1:GFP)* [59], *y264Et* [29], *s1181tEt* [14], *Tg(gad1b:GFP)nns25 (gad1b:GFP)* [20], *Tg(slc6a5:GFP)cf3 (glyT2:GFP)* [64], *Tg(-17.6isl2b:GFP)zc7 (isl2b:GFP)* [65], *Tg(-3.4tph2:Gal4ff)y228 (tph2:Gal4)* [47], *TgBAC(slc17a6b:lox-DsRed-lox-GFP)nns14 (vglut2a:DsRed)* [36], *Tg(slc17a6:EGFP)zf139* [35], *Tg(elavl3:CaMPARI(W391F+V3987L))jf9* [82], *Tg(phox2b:GFP)w37* [66], *J1229aGt* [83] and several Gal4 enhancer traps from ZBB: *y304Et*, *y332Et*, *y341Et*, *y351Et* and *y393Et* [76]. All in vivo experimental protocols were approved by the NICHD animal care and use committee.

Immunohistochemistry

Immunolabeling was as described [4] with the following adaptations. Larvae were fixed overnight at 4°C in PBS with 4% paraformaldehyde and 0.25% Triton X-100. Samples were then washed in PBS containing 0.1% Triton X-100 (PBT) 3 times for 5 min. For antigen retrieval, samples were incubated in 150 mM Tris-HCl pH 9.0 for 5 min at room temperature (RT), followed by 15 min at 70°C and washed in PBT 2 times for 5 min at RT [84]. Critically, samples were then permeabilized on ice in fresh 0.05% trypsin-EDTA for no more than 5 minutes. If pigmented, samples were incubated in PBT with 1.5% H₂O₂ and 50 mM KOH for 15 min, rinsed 2 times in PBT and washed again for 10 min, all at RT. Samples were then blocked in PBT containing 5% normal goat serum (NGS) and 0.2% bovine serum albumin (BSA) for 1 hr at RT before incubation at 4°C with tERK antibodies (Cell Signaling, 4696) diluted 1:500 in PBT with 5% NGS and 0.2% BSA for a minimum of 6 hr. Samples were then washed with PBT 4 times for 30 min at RT before incubation at 4°C for a minimum of 2 hr with fluorescent secondary antibodies (Alexa Fluor 488 or 548) diluted 1:1000 in PBT with 5% NGS and 0.2% BSA. Samples were finally rinsed 4 times for 30 min at RT prior to imaging.

Registration

Registrations were performed using the Computational Morphometry Toolkit (CMTK) version 3.2.3 (Computational Morphometry Toolkit, RRID:SCR_002234) and ANTs version 2.1.0 (ANTs - Advanced Normalization Tools, RRID:SCR_004757)

running on the National Institute of Health's Biowulf Linux computing cluster. Registrations were parallelized using Slurm-based bash scripts available upon request. For CMTK, previously optimized registration parameters that minimize computation time while maximizing precision were used (affine parameters: `registrationx --dofs 12 --min-stepsize 1`; elastic parameters: `warpx --fast --grid-spacing 100 --smoothness-constraint-weight 1e-1 --grid-refine 2 --min-stepsize 0.25 --adaptive-fix-thresh 0.25`). For ANTs registrations, the parameters used are cited in the relevant text and figures with optimized parameters listed in Table 1. All deformable transformations are initiated with a rigid and affine step (parameters included in *Table 3.1*). Aside from the use of ANTs, the basic imaging and registration workflow was performed as previously described [76]. Image volumes were rendered within the Zebrafish Brain Browser (ZBB), ImageJ [33] or code written in IDL (Harris Geospatial Solutions). For the conversion to/from NIFTi format required for ANTs, we used the ImageJ plugin `nifti_io.jar` written by Guy Williams [26].

Volume rendering & 3D visualization

Binary masks corresponding to 25 anatomical regions from Z-Brain aligned to ZBB were converted into meshes using the Create Surfaces tool in the `IntSeg_3D.jar` plugin for ImageJ [27]. Edges for individual meshes were iteratively reduced below 5000 and vertices (single-precision floating-points of the triangular meshes) written as OBJ files. As there is no intrinsic color or color conventions as of yet for these brain structures, we used color hue as a nominal categorical coding for each region. To

maximize accessibility, we rendered meshes in Extensible 3D (X3D) format, an ISO (International Organization for Standardization) standard developed by the not-for-profit Web3D Consortium [28]. This format allows portability between numerous tools and applications as well as deployment across a broad spectrum of platforms. For the rendering, OBJs were transcoded into ImageTextureAtlas PNGs using X3D's standard IndexedFaceSet to represent mesh information and then tiled at different resolutions (4096 & 8192 pixels squared) using AtlasConversionScripts [29]. Additionally, dask and pyimg python libraries were used to generate volume norms (image and ImageTextureAtlas files) by gradient descent. All renderings were then merged into a single X3D XML scene which was losslessly compressed (in SRC/glTF) to a final size of 4.5 MB. This makes the scene compact enough to be visualized on a cell phone, while retaining details for visualization and editing in immersive virtual reality environments. Finally, X3D files were published to HTML5 via the X3DOM library and a simple user interface created that allows for the visibility of different structures to be toggled on and off. Brain meshes were converted to FBX files for import into Unity using Blender 2.78a (Blender foundation, Amsterdam, NL) and mobile app development for Google Cardboard VR headsets performed in Unity 5.4.2 (Unity Technologies SF, San Francisco CA) using the Google VR for Unity SDK (Google, Mountain View CA). Custom scripts controlling movement and mesh display were written for Unity in C#.

Measurements

Mean Landmark Distance (MLD). To assess registration precision using MLDs, corresponding landmarks were located and annotated on the reference brain, and on unregistered brains. In each case, landmarks were chosen to be widely distributed within the brain, and readily recognized in corresponding brain scans. In addition, to verify recognizability, the vglut2a landmarks in the reference brain were located by 3 blinded scorers ; mean distance from each of the 10 reference points ranged from 1.7 to 11.8 μm (mean, $4.5 \pm 0.9 \mu\text{m}$). Using ImageJ, we positioned a 3 micron cube centered on each landmark in a second channel for each brain scan, then, after registering the brain scan using the first channel, applied the resulting transformation matrix to the second channel, using Nearest Neighbor interpolation for both CMTK and ANTs. Landmark distance was taken as the distance between the geometrical center of the corresponding cubes in the reference image, and in the registered image.

Hausdorff distance. We manually segmented cells in a vglut:DsRed brain scan in a second channel and applied transformation matrices for registration to this second channel. Segmented cells were broadly distributed to ensure that distortion measures sampled the entire brain, and cell masks conservatively drawn within the boundaries of the soma. We then compared the morphology of cells after registration (A), to their original shape (B) by calculating the partial Hausdorff distance [85]. Briefly, for every point in a segmented cell mask before registration, we found the minimum distance to a

point in the same mask after registration. The Hausdorff distance is the maximum of all such distances, calculated for both $A \rightarrow B$ and $B \rightarrow A$. Because the Hausdorff distance is highly sensitive to cell alignment, and registration displaces cells from their original location, we found the optimal alignment for comparisons using a two-step process. First we aligned the geometric center of each cell in the original and transformed images. Second we searched for the minimal Hausdorff distance across 4940 rigid transformations of the aligned cell, within a $3 \times 3 \times 3$ micron cube, (0.25 micron steps in each dimension). Finally, as Hausdorff distances are sensitive to outliers, we used the 95th percentile distances instead of the maximum Hausdorff distance for all measures [85].

Cell volume. For each segmented cell, we calculated its change in volume as the absolute value of the fractional change in the number of pixels after application of a transformation matrix.

Elongation index. For each pixel in a segmented cell, we found the maximal distance (MD) to any other pixel in the mask. The elongation index for a given cell was the 95th percentile largest value of MD, which we take as an approximation of the diameter of the cell across its longest axis.

Cross correlation. Cross correlation between the tERK-stained reference brain, and registered tERK stains, was performed using the `c_correlate` function within IDL version 7.0. Correlations were run within eighteen $50 \mu\text{m}$ -side cube sub-regions of the image

volumes that were manually selected to encompass high contrast boundaries and the mean of the 18 values taken as the mean cross correlation (MCC) for each brain in Fig. 3. *Jaccard index*. Anti-tERK immunohistochemistry intensely stains tectal neuropil. Thus for measuring the accuracy of registration of the tectal neuropil, we manually segmented the left tectal neuropil area in 6 confocal scans of tERK stained larvae and our reference brain. We applied transformation matrices to these masks, then calculated the Jaccard index as the volume of the intersection between each registered mask (A) and the reference brain (B), divided by the total volume of the union of A and B.

Results

Optimization of ANTs based registration of live *vglut2a:DsRed* image scans

Brain registration in Z-Brain and ZBB used the B-spline elastic transformation in CMTK. Before attempting to co-align Z-Brain and ZBB, we tested an alternate algorithm for brain alignment, the diffeomorphic symmetric normalization (SyN) method in ANTs, because: (1) SyN has been shown to outperform B-spline transformations for deformable image registration in a variety of imaging modalities [86,87]. (2) ANTs permits registration using multiple reference channels, potentially allowing the use of multiple complementary expression patterns as references for improved registration fidelity. (3) By calculating forward and reverse transformations simultaneously, SyN transformation matrices are intrinsically symmetric, ensuring that bridging registrations would be

unbiased and that we could easily perform reciprocal transformations to register each dataset into the other's coordinate system.

To calibrate registration parameters, we assessed the alignment precision and distortion of cell morphology after the registration of six representative *vglut2a:DsRed* scans to the original *vglut2a:DsRed* reference brain in ZBB (*vglut2a_{ZBB}*; file *vglut-dsred-ref-01.nii.gz*, available from [33], procedure summarized in **Fig. 3.1a**). Similar to CMTK we employed a three step registration within ANTs where rigid and affine steps were used to initialize a deformable registration using the SyN diffeomorphic transformation with cross correlation (CC) as the similarity metric. We tested a range of values for each of the SyN parameters as well as the radius of the region used for cross correlation.

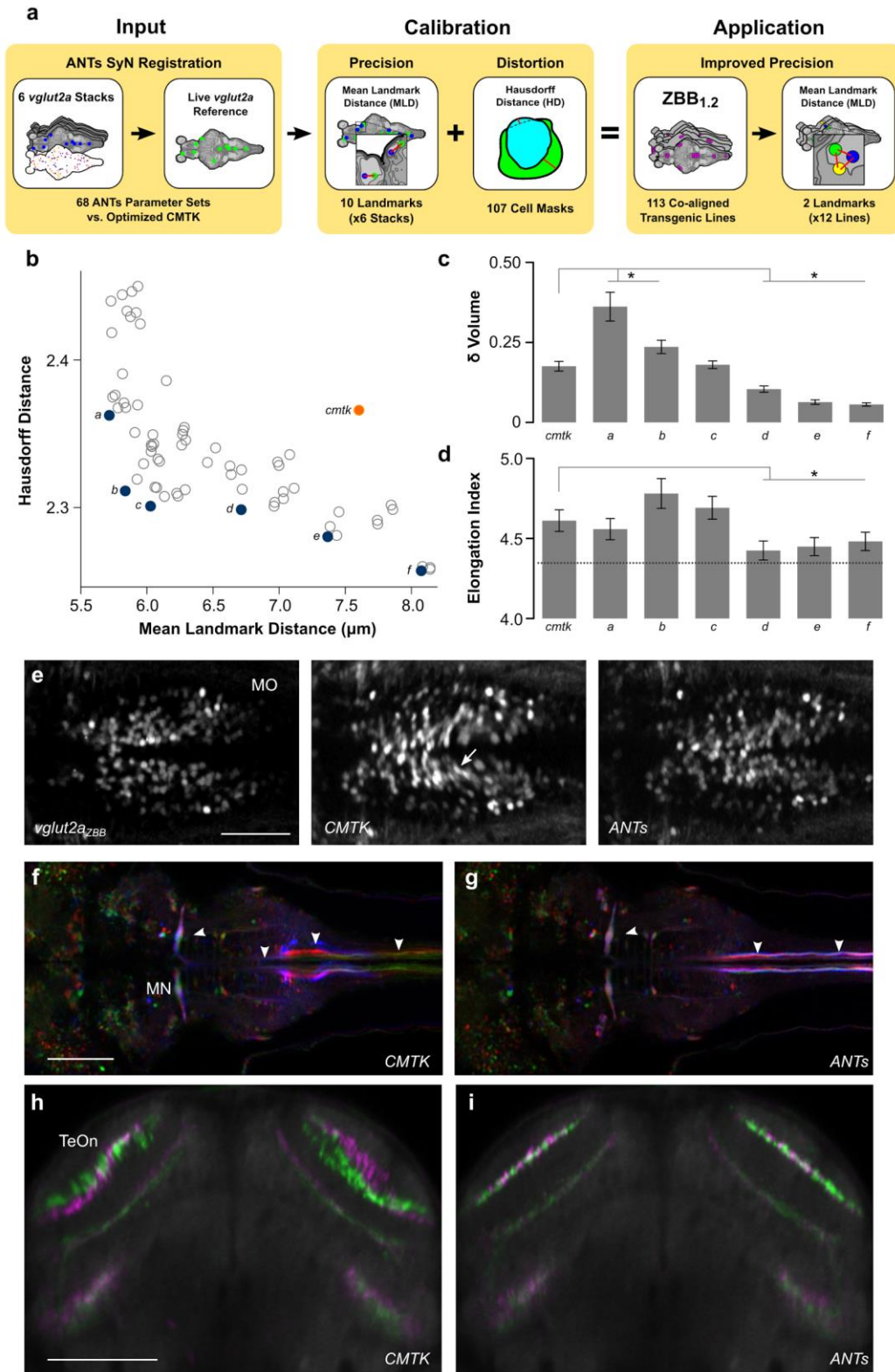
To measure registration precision, we visually located 10 point-based landmarks in the *vglut2a_{ZBB}* pattern (**Additional File 3.1a-c**; file *vglut-dsred-ref-01-landmarks.nii.gz*, available from [33]) and in each of the 6 *vglut2a:DsRed* confocal scans. We then used the *vglut2a:DsRed* channel for registration, and applied the resulting transformation matrix to the landmarks in each of the 6 brains. We measured the distance of each landmark from its location in the *vglut2a_{ZBB}* reference brain (**Additional File 3.1a,d**). We designated the average of the 10 distances the 'Mean Landmark Distance' (MLD). To assess the amount of distortion in cell shapes produced by the parameter sets, we segmented 107 cells in an unregistered *vglut2a:DsRed* confocal scan (**Additional File 3.2**), and applied each transformation matrix to this set of cell masks. Changes in cell

shape were measured using the partial Hausdorff distance for each cell after registration compared to its original shape (see *Methods*).

Next we plotted the MLD against the Hausdorff distance and located points along the Pareto frontier (*Fig. 3.1b*) of these two measures. These points represent potentially optimal transformations, where registration accuracy can only be improved by increasing distortion, or vice versa. To distinguish between these points, we examined two additional measures of distortion: the change in cell volume (*Fig. 3.1c*) and maximal elongation (*Fig. 3.1d*). Three transformations showed statistically significantly reduced distortion compared to CMTK for both measures, and we selected the one (*Fig. 3.1b*, point d) with the greatest precision for further testing. With this set of parameters (see *Table 3.1*, live registration), mean registration error was within the diameter of a single neuron for both ANTs and CMTK (MLD for ANTs $6.7 \pm 0.3 \mu\text{m}$, for CMTK $7.6 \pm 0.4 \mu\text{m}$; $N = 6$ brains, paired t-test $p=0.056$). However, cell morphology was better preserved using ANTs (Hausdorff Distance for ANTs 2.30 ± 0.14 , CMTK 2.37 ± 0.14 ; $N = 107$ cells, paired t-test $p=0.013$), especially within ventral structures such as the hypothalamus and the caudal medulla oblongata (*Fig. 3.1e*).

Table 3.1. ANTs command parameters for image registration.

Figure 3.1. Optimization of parameters for registration of live brain scans using ANTs.



(a) Overview of parameter optimization for live brain scans using ANTs. A calibration set of 6 *vglut2a:DsRed* confocal stacks with 10 point-based landmarks and 107 cell masks were registered to the *vglut2aZBB* reference with the same 10 point-based landmarks defined (left). MLDs for landmarks and Hausdorff distance for transformed cell masks compared to their originals were measured for each parameter set (middle). Optimal parameters selected from these metrics (b-d) were used to re-register all lines generating ZBB1.2 where MLD was measured from 2 additional landmarks in each of 12 co-aligned patterns (right). (b) Hausdorff distance for cell shape comparison plotted against MLD for 68 sets of parameters tested using ANTs (grey and blue circles) and after registration using CMTK (orange). Blue circles labeled a-f indicate the Pareto frontier. (c) Mean absolute change in cell volume (as a fraction of the original volume) produced by transformations resulting from parameter sets a-f and CMTK in (b). * $p < 0.05$, compared to CMTK. (d) Mean elongation index for cells after registration using parameter sets a-f and CMTK in (b). Dashed line shows index for cells before registration — all transformations produced a significant increase in compared to the untransformed cells. * $p < 0.05$, compared to CMTK. (e) Horizontal section through the medulla oblongata in *vglut2aZBB*, and of a representative *vglut2a:DsRed* brain after registration using CMTK or ANTs. Distortion artifacts are indicated (arrow). Scale bar 50 μm (f,g) Horizontal section in *J1229aGt* showing expression of GFP in the Mauthner cell and axon (arrowheads) for three individual larvae (pseudo-colored red, green and blue). Registration was performed with CMTK (f) or ANTs (g). Scale bar 100 μm . (h,i) Transverse section through the optic tectum in two separate average brain images (colored green and magenta) for *y393Et*. For each brain image, we independently scanned three individual brains and registered them using CMTK (h) or ANTs (i). Scale bar 100 μm .

We next examined whether these registration parameters also improved precision for the co-aligned transgenic lines. For ZBB, we co-scanned transgene and enhancer trap expression patterns with the *vglut2a:dsRed* transgene, allowing us to register each expression pattern to *vglut2aZBB*. We first compared the overlap and morphology of the Mauthner cells from brain scans of three different individuals of transgenic line *J1229aGt* [83]. Overlap of Mauthner cell bodies was similar for CMTK and ANTs (*Fig. 3.1f,g*). However, in CMTK registered images, the Mauthner axon was distorted in the caudal

medulla, whereas axon morphology was preserved with ANTs. Second, in our previous work, we assessed the precision of CMTK registration using line *y339Et* by independently scanning two sets of three larvae, producing an average for each set, and visually comparing the result. With CMTK we had noted misalignment of approximately 1 cell diameter in the neuropil of the optic tectum (*Fig. 3.1h*). This was substantially improved with ANTs, where there was much closer alignment of the two averages (*Fig. 3.1i*).

Improved precision of ZBB after registration using ANTs

We next recompiled ZBB using ANTs to register the entire set of 354 brain scans from 109 different transgenic lines that were part of ZBB, then as before, averaged multiple larvae to create a representation of each transgenic line, masked the average stacks to remove expression outside the brain and re-imported the resulting images into our Brain Browser software. We refer to this new recompilation of the atlas as ZBB_{1.2}. Unprocessed and registered brain images are available online [88].

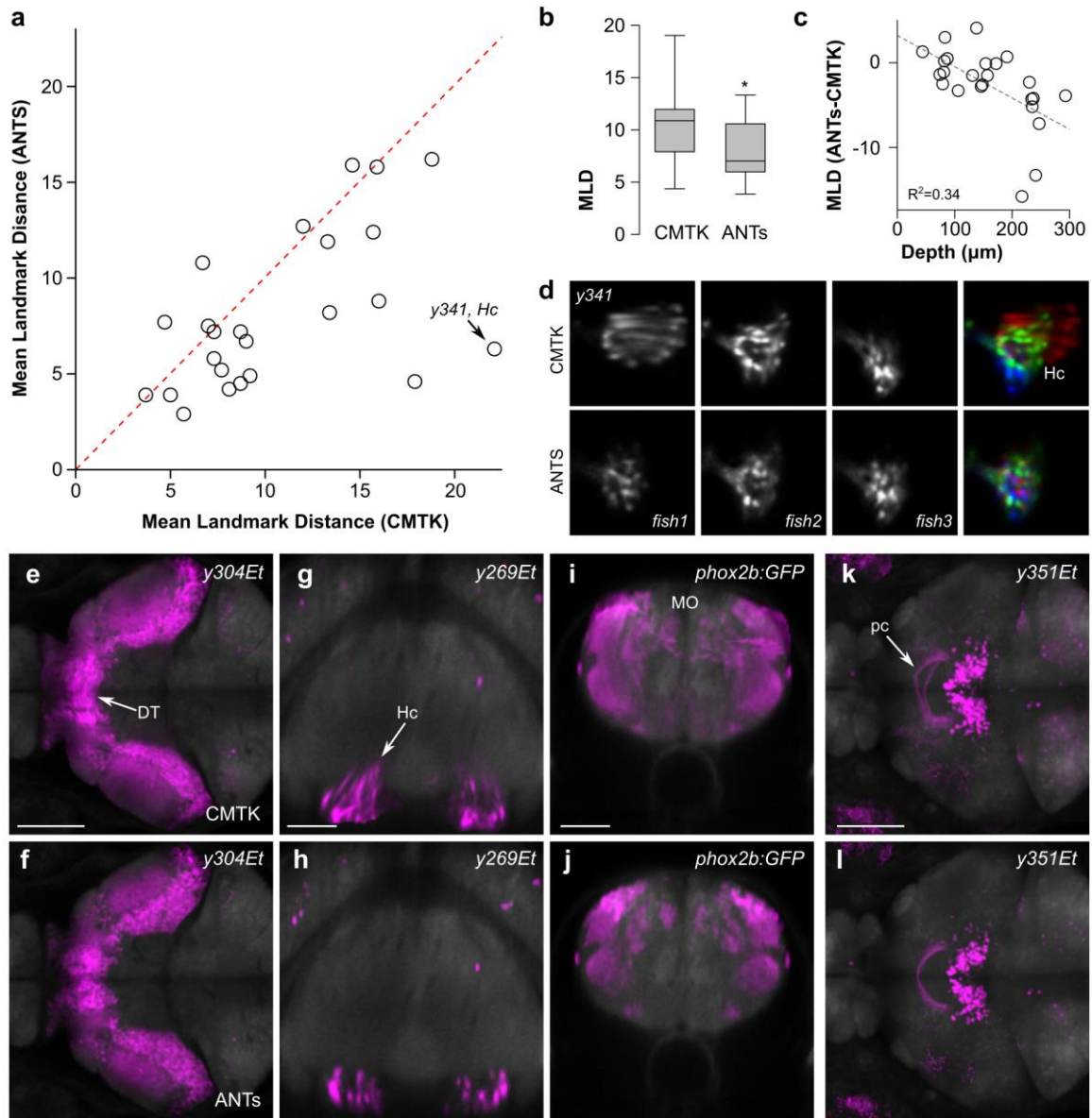
To determine whether ZBB_{1.2} was a quantitative improvement over ZBB, we identified two conspicuously labeled cells or landmarks in each of 12 transgenic lines from the atlas (*Additional File 3.3*). We marked these positions in each of the three brain scans for each line, then, after registration, calculated the distance between corresponding points in each pair of brains. The mean of these distances measures how precisely landmarks are registered across the three brains. We performed this procedure first for

brains registered using CMTK, then for the same set of brains registered using ANTs, allowing us to compare MLDs for the two methods (*Fig. 3.2a-b*). Overall, landmark distances decreased from ZBB to ZBB_{1.2} ($10.8 \pm 1.02 \mu\text{m}$ to $8.1 \pm 0.83 \mu\text{m}$; N = 24 landmarks, paired t-test $p=0.008$), indicating that ZBB_{1.2} has significantly improved precision, and confirming that the new atlas is accurate to approximately the diameter of a single neuron. The improvement was greatest deeper in the brain (*Fig. 3.2c*; linear regression, N=24, $p=0.003$) with the largest improvement for the caudal hypothalamus in line *y341*, where increased alignment precision was associated with noticeably reduced distortion between the three brain scans (*Fig. 3.2d*).

Additionally, we inspected regions of ZBB_{1.2} where we had noticed poor registration precision or pronounced cell distortion in the original ZBB. One such area was the dorsal thalamus, where cell morphology was noticeably perturbed after elastic registration with CMTK, with cell somas stretching across the midline (*Fig. 3.2e*). In ZBB_{1.2} cells retained a rounded morphology with distinct cell clusters on the left and right sides of the brain (*Fig. 3.2f*). Similarly, distortions in cell shape that were apparent in the caudal hypothalamus in ZBB, were absent in ZBB_{1.2} (*Fig. 3.2g,h*). In the caudolateral medulla, we previously obtained poor registration, with expression extending to regions outside the neural tube (*Fig. 3.2i*). In ZBB_{1.2}, patterns had improved bilateral symmetry and were correctly confined to the neural tube (*Fig. 3.2j*). Finally, we noticed that the posterior commissure was poorly aligned between larvae leading to a defasciculated appearance in ZBB (*Fig. 3.2k*), whereas this tract had the expected tightly

bundled appearance in ZBB_{1.2} (*Fig. 3.2I*). Together, these observations confirm that ZBB_{1.2} is a more faithful representation of the transgenic lines. Not only is cell morphology better preserved, but global registration precision is improved compared to the original ZBB atlas.

Figure 3.2. Improved precision of transgene representations in ZBB1.2.



(a) Mean landmark distances for 24 landmarks, after registration with CMTK and ANTs. Dotted line indicates 1:1 ratio. **(b)** Boxplot of data in **(a)**. * paired t-test, N=12 lines, $p = 0.019$ **(c)** Difference in MLD between ANTs and CMTK plotted against distance from the dorsal-most point in the brain. **(d)** Horizontal section through the caudal hypothalamus of three individual *y341Et* larvae as well as their pseudo-colored

superimposition following registration with CMTK (top row) or ANTs (bottom row). **(e,f)** Horizontal section through the thalamus showing the averaged representation of enhancer trap line *y304Et*, where individual brains were registered with CMTK for ZBB **(e)**, or with ANTs for ZBB_{1,2} **(f)**. Arrow indicates neurons that are artificially elongated across the midline. Scale bar 100 μm . **(g,h)** Transverse section through the caudal hypothalamus showing the average enhancer trap line *y269Et* brain registered with CMTK **(g)** or with ANTs **(h)**. Arrow shows distortion of cells causing the caudal hypothalamus to appear dorsally elongated. Scale bar 50 μm . **(i,j)** Transverse section through the medulla oblongata showing the average *phox2b:GFP* brain with CMTK **(i)** or ANTs **(j)**. Scale bar 50 μm . **(k,l)** Horizontal projection through the posterior commissure (arrow) for the average *y351Et* brain obtained with CMTK **(k)** or ANTs **(l)**. Scale bar 100 μm .

Optimization of ANTs registration parameters for fixed tissue

The Z-Brain atlas was derived by registering brain scans to a single brain that was fixed, permeabilized and immunostained for tERK expression. We therefore anticipated that tERK would be a useful channel for bridging the two atlases, if we could first successfully register a tERK-stained *vglut2a:DsRed* expressing brain to ZBB_{1,2}. Therefore, we fixed and stained a transgenic *vglut2a:DsRed* larva for tERK, and registered the tERK pattern to ZBB_{1,2} using the *vglut2a* pattern. We used the resulting image as our ZBB tERK reference brain (tERK_{ZBB}; file *terk-ref-02.nii.gz* available from [33]).

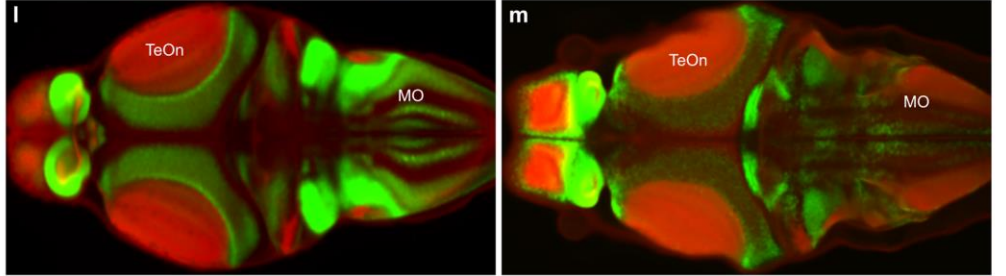
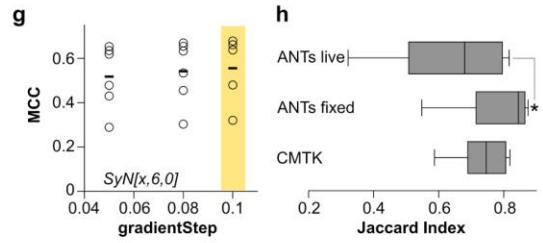
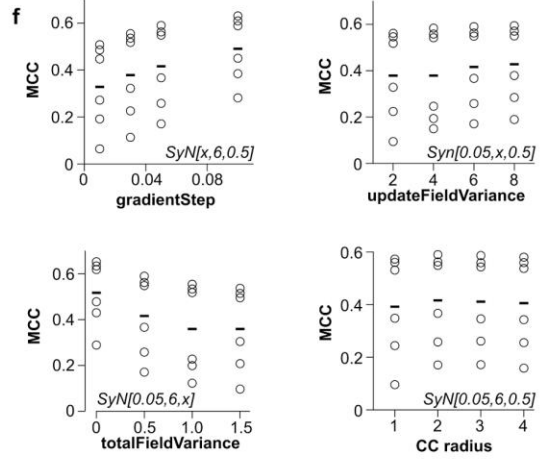
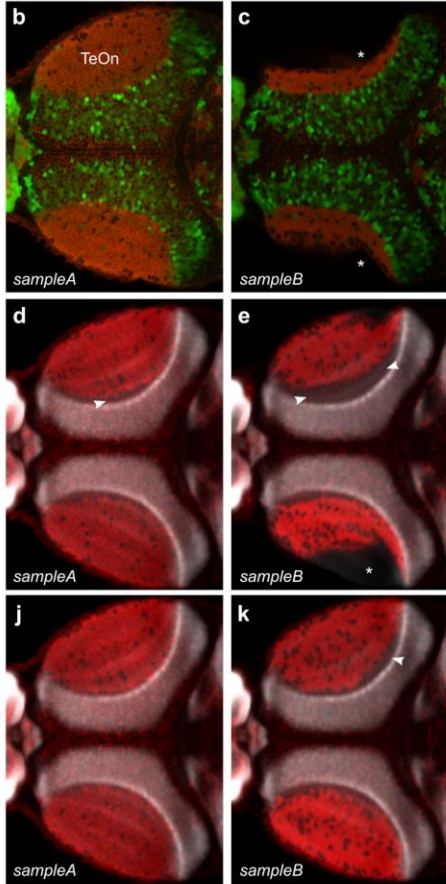
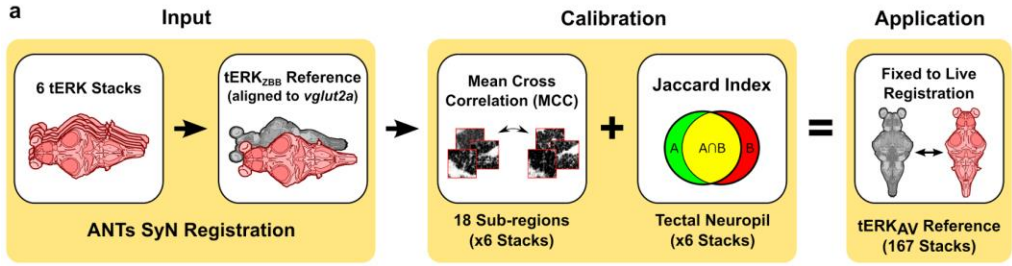
In addition to the tERK reference brain, Z-Brain contains an average tERK representation from 197 tERK stained larvae, which we thought might serve as a bridge between atlases. During studies on pERK-based activity mapping, we had previously generated a dataset of 167 tERK stained brains and therefore used these to create our own average tERK representation by registering them to tERK_{ZBB}. However, during this

process, we noticed a high degree of variability between tERK stained brains, most salient in poor labeling of ventral brain structures and in deformation of the optic tectum neuropil. Immunohistochemistry for tERK proved highly sensitive to staining parameters with the trypsin activity, permeabilization duration, and antigen retrieval having the strongest effects. Variability in fixed tissue was most apparent in the optic tectum, where high trypsin activity tended to disrupt morphology and reduce the volume of the tectal neuropil (*Fig. 3.3b,c*). These local distortions were not resolved by deformable image registration: alignment to tERK_{ZBB} with the same parameters optimized for live vglut2a based registration failed to correct the reduced tectal neuropil volume (*Fig. 3.3d,e*; asterisk) and often created an artifact where the neuropil zone failed to abut the underlying cellular layer labeled by vglut2a expression (*Fig. 3.3d,e*; arrowheads).

We therefore varied the registration parameters that were optimal for live vglut2a registration, to find settings that best rectified the variable tissue morphology following fixation and permeabilization (process summarized in *Fig. 3.3a*). For optimization of fixed tissue registration, we used a set of 6 tERK stained brains (including the Z-Brain tERK reference), iteratively varied parameters for registration to tERK_{ZBB} and assessed registration fidelity. For measuring precision, we were not able to identify unambiguous landmarks within the optic tectum, so we instead calculated the cross-correlation between each of the aligned tERK stains and tERK_{ZBB} within small volumes, including parts of the tectum (*Fig. 3.3f,g*). To verify that the 'fixed brain' parameters that yielded the greatest cross correlation did in fact improve registration within the tectum, we manually

segmented the tectal neuropil in the same 6 brains, applied the transformation matrix to each mask, and calculated the Jaccard index for overlap with the segmented neuropil in tERK_{ZBB}. Parameters for fixed brain registration produced a significant increase in overlap, compared to the live brain parameters (*Fig. 3.3h,i*) and visual inspection confirmed that the morphology of the optic tectum neuropil after registration was greatly improved (Fig. 3j,k). We therefore used ANTs with the fixed brain parameters (*Table 2.1*, fixed registration) to register our 167 tERK stained brains to tERK_{ZBB}, and generated an average tERK representation comparable to the 197 tERK average in Z-Brain (*Fig. 3.3l,m*).

Figure 3.3. Optimization of ANTs registration parameters for fixed tissue.



(a) Overview of parameter optimization for fixed brain scans using ANTs. A calibration set of 6 tERK confocal stacks with segmentations of the tectal neuropil were registered to tERK_{ZBB}, a tERK and *vglut2a:DsRed* confocal scan previously aligned to the *vglut2a*_{ZBB} reference (left). MCCs were calculated between eighteen 50 μ m-side cube high-contrast sub-regions in the calibration set and in the tERK_{ZBB} reference to identify parameters that maximized MCC (f,g) and improved the Jaccard index of tectal neuropil segmentation (h) while compensating for fixation artifacts (c,e,k) (middle). These optimized ANTs parameters allow for the accurate registration of fixed tissue and the generation of a tERK average reference (tERK_{AV}) useful for bridging live and fixed tissue registrations (right). (b,c) Horizontal section through the optic tectum of tERK immunostained (red) *vglut2a:DsRed* (green) larvae, using diluted (b, sample A) or fresh trypsin (c, sample B). Asterisk indicates missing area of tectal neuropil due to permeabilization artifact. (d,e) Horizontal section through the same stacks as in (b,c) registered to tERK_{ZBB} using the parameters previously optimized for live registration. Gray shows the ZBB_{1.2} *vglut2a:DsRed* pattern. Arrowheads highlight regions where tERK in the optic tectum neuropil fails to closely abut the adjacent glutamatergic cellular layer. (f) MCC for tERK expression after registration of 6 brains to tERK_{ZBB}, varying each of the parameters for the ANTs SyN transform, starting with the parameters that gave the best registration for live *vglut2a:DsRed* based registration (SyN[0.05,6,0.5]). Bottom right: MCCs after varying the radius of the cross-correlation metric used during registration. (g) MCCs for tERK in the same brains as in (f), after combining the two best parameter sets from (f) (SyN[0.1,6,0.5] and SyN[0.05,6,0]) to assess further improvement in registration precision. Yellow box highlights the final optimal parameter set. (h) Jaccard index for overlap of the manually segmented tectal neuropil of the reference brain, with each of the 6 brains in the calibration set. $p < 0.01$. (i) 3D view of overlap between segmented tectal neuropils from tERK_{ZBB} (red) and the Z-Brain tERK reference brain (green), after registration with ANTs using parameter optimal for live registration, fixed registration and CMTK. (j,k) Same brains as in (d,e), but after registration to tERK_{ZBB} using the parameters optimized for fixed tissue registration. (l,m) Horizontal section through the optic tectum showing tERK expression (red) and *vglut2a:DsRed* expression (green) in ZBB1.2 (l) and Z-Brain (m). Matching slices within the optic tectum were selected; because the rotation around the y-axis is slightly different, sections are different within the medulla.

Inter-atlas registration using multi-channel diffeomorphic transformation

Z-Brain and ZBB incorporated eight expression patterns that we judged sufficiently similar to act either as templates for bridging the datasets and/or to provide metrics for assessing the precision of a bridging registration (*Table 3.2, Additional File*

3.4). For example, *vglut2a*_{ZBB} is a confocal scan of DsRed in a single larva from transgenic line *TgBAC(slc17a6b:loxP-DsRed-loxP-GFP)nns14*, whereas Z-Brain includes *Tg(slc17a6:EGFP)zf139*. In both cases, reporter expression is regulated by the same bacterial artificial chromosome [20,35]. Crossing these two lines allowed us to scan DsRed and EGFP in the same larva and confirm that the patterns were largely congruous, potentially allowing us to use *vglut2a* expression to bridge the two atlases. Likewise, the expression patterns of *tERK*, *elav13*, *isl2b*, *vmat2* in Z-Brain and ZBB appeared sufficiently similar to provide templates for atlas co-registration.

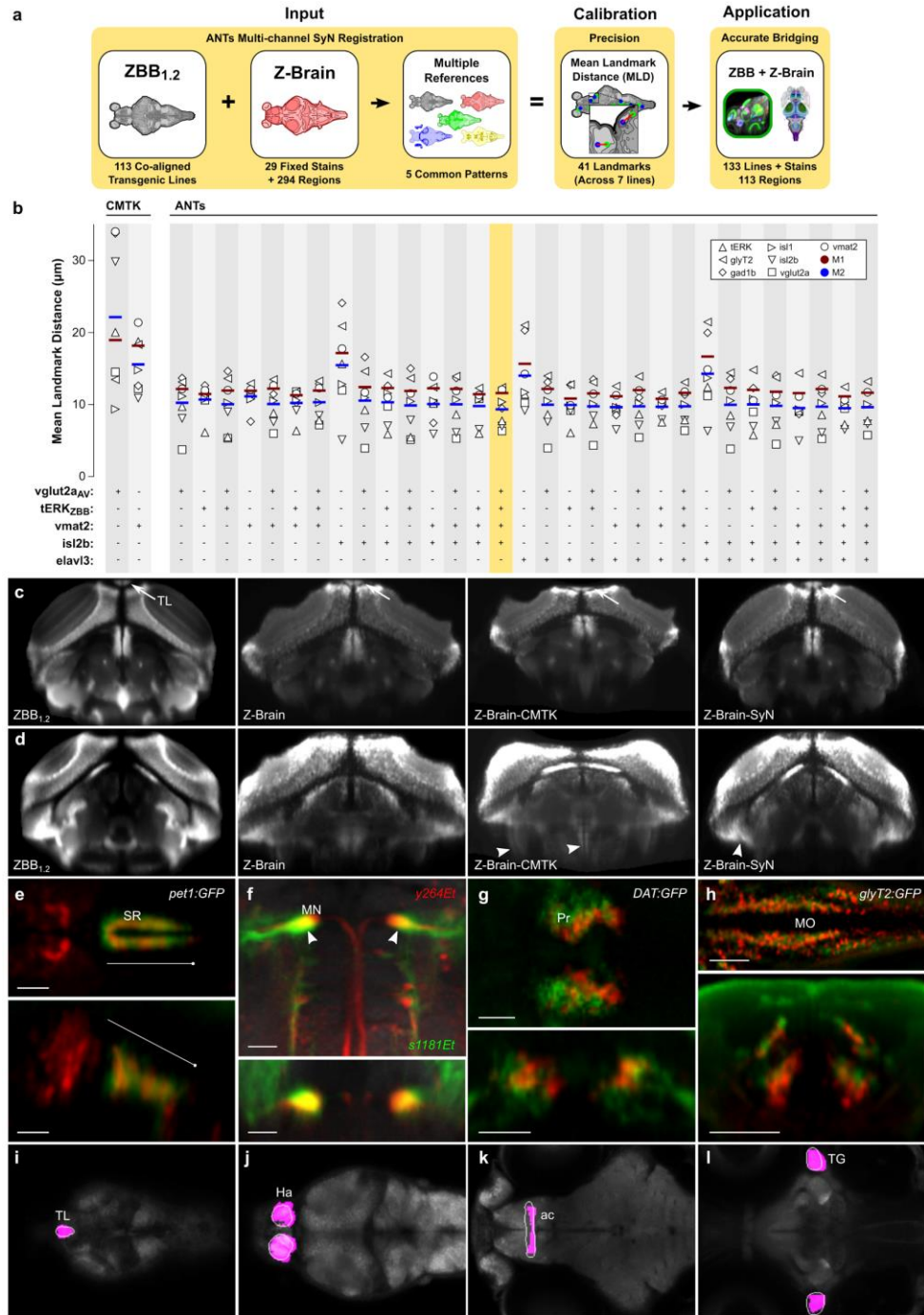
Taking advantage of the ability of ANTs to use of multiple reference channels concurrently, we compared the effect of combinatorial use of complementary reference channels for inter-atlas registration (process summarized in **Fig. 3.4a**). We used seven expression patterns to evaluate registration precision: *vglut2a*, *isl2b*, *vmat2*, *tERK*, *isl1*, *gad1b* and *glyT2*. For each pattern we identified a set of 4-10 point-based landmarks that could be identified in corresponding ZBB and Z-Brain images and that were widely distributed to represent diverse brain regions (total of 41 landmarks ; **Additional File 5**). We marked these points in each set of images, registered Z-Brain images to ZBB_{1,2} images, measured the distance between cognate landmarks and calculated the mean landmark distance for each of the seven expression patterns. We used two summary measures of registration precision. The first metric (M1) was the mean of MLDs for the three patterns that were not used to drive registration (*isl1*, *gad1b* and *glyT2*). Although these channels measure precision independent of the patterns for atlas registration, they

are relatively sparse and do not assess precision across the whole brain. Thus, to provide a global measure of precision, we also used a second metric (M2) that was the mean of all seven MLDs: those in M1 plus four of the patterns used as references for registration — vglut2a, tERK, isl2b and vmat2.

Using CMTK, minimal M1 and M2 scores were obtained using the average vmat2 pattern as the reference (*Fig. 3.4b*; mean MLD for 41 landmarks $14.9 \pm 1.3 \mu\text{m}$). We therefore registered all images in Z-Brain to ZBB using the vmat2 average in each dataset as the reference channel. We observed severe tissue distortions in several brain regions, with noticeable flattening of the torus longitudinalis as well as gross tissue distortions, particularly in ventral brain regions (*Fig. 3.4c,d*; ZBrain-CMTK). Next we used the ANTs SyN algorithm to register the atlases. Ideally, patterns for registration should include information throughout the brain. Because ANTs can use multiple concurrent reference channels to derive an optimal transformation matrix, we speculated that the best possible transformation would be achieved by a combination of channels with complementary information. We therefore produced an inter-atlas transformation matrix for every combination of the elavl3, isl2b, vglut2a_{AV} (vglut2a average brain), vmat2, tERK_{ZBB} (tERK single brain) and tERK_{AV} (tERK average brain) patterns as references. Because Z-Brain used fixed samples, we used the registration parameters optimized for the greater variability present in fixed tissue. Multi-channel registration significantly reduced M1 and M2 values compared to any single channel alone and to transformations obtained using CMTK. The registration obtained with vglut2a, tERK_{ZBB}, vmat2 and

isl2b gave the lowest global metric (M2) value and an M1 score within 10% of the lowest scoring combination (*Fig. 3.4b*). With these parameters, the MLD was $9.1 \pm 0.8 \mu\text{m}$ (N=41 landmarks) and the overt tissue distortions noted after elastic registration were far less salient (*Fig. 4c,d*; ZBrain-SyN). We therefore applied the transformation matrix obtained with this set of channels to the database of gene expression patterns in Z-Brain to align them to ZBB_{1,2}, and used the inverse of the transformation generated by SyN to register ZBB_{1,2} to the Z-Brain coordinate system. We imported all Z-Brain expression patterns not previously represented in the database into ZBB_{1,2}, producing a total of 133 expression patterns.

Figure 3.4. Transformation between Z-Brain and ZBB coordinate systems using multi-channel registration.



(a) Overview of bridging Z-Brain and ZBB using ANTs multi-channel registration. Combinations of 5 patterns common between Z-Brain and ZBB (vglut2a_{AV}, tERK_{ZBB},

vmat2, isl2b and elavl3) were used guide multi-channel bridging registrations (left). MLDs for 41 landmarks in *gad1b*, *glyT2*, *isl1*, *isl2b*, *tERK*, *vglut2a*, and *vmat2* expression were measured for all reference channel combinations (middle). The combination of *vglut2a_{AV}*, *tERK_{ZBB}*, *vmat2*, and *isl2b* enabled the most accurate bridging of ZBB and Z-Brain allowing the combination of the large collection of live transgenic lines of ZBB with the fixed tissue techniques and expert neuroanatomic segmentations of Z-Brain (right). **(b)** MLDs for the expression patterns of *gad1b*, *glyT2*, *isl1*, *isl2b*, *tERK_{ZBB}*, *vglut2a* and *vmat2* and M1 and M2 metrics after registration of Z-Brain to ZBB1.2 using either CMTK or ANTs SyN with fixed-tissue registration parameters and the indicated combination of reference channels (*vglut2a*, *tERK_{ZBB}*, *vmat2*, *isl2b*, and *elavl3*). Note, similar results were obtained using *tERK_{AV}* instead of the *tERK_{ZBB}*, but are omitted for clarity. The combination of reference channels selected for co-registration of Z-Brain and ZBB is highlighted. **(c)** Transverse section through the caudal optic tectum showing the *vglut2a* pattern in ZBB_{1.2}, Z-Brain, Z-Brain after registration to ZBB with CMTK (Z-Brain-CMTK), or with ANTs (Z-Brain-SyN). The torus longitudinalis (TL) is well separated from tectal neurons in live scans, but less so in fixed tissue (arrows). The TL appears flattened after CMTK registration, but retains normal morphology after registration with ANTs SyN. **(d)** Transverse sections as in **(c)**, but slightly more caudal with contrast increased to highlight ventral distortion artifacts produced by registration (arrowheads). **(e-h)** Brain Browser views in the ZBB_{1.2} coordinate (**e,f**) or Z-Brain coordinate (**g,h**) space. Scale bars 25 μ m except 50 μ m in **(e)**. **(e)** Horizontal (top) and sagittal (bottom) sections, comparing the *pet1:GFP* expression pattern in the superior raphe in ZBB_{1.2} (red) and Z-Brain after transformation to the ZBB coordinate system (green). **(f)** Horizontal (top) and transverse (bottom) sections through the medulla oblongata, showing the expression of *y264Et* from ZBB_{1.2} (red) and *s1181Et* from Z-Brain after transformation to ZBB_{1.2} (green), which both label the Mauthner cells (arrowhead). **(g)** Horizontal (top) and transverse (bottom) sections through the pretectum, comparing the expression of *DAT:GFP* from ZBB1.2 after transformation to Z-Brain (red) and anti-tyrosine hydroxylase staining in Z-Brain (green). **(h)** Horizontal (top) and transverse (bottom) sections through the medulla oblongata for *glyT2:GFP* from ZBB_{1.2} after transformation to Z-Brain (red) and the same transgenic line in Z-Brain (green). **(i-l)** Brain Browser horizontal sections showing manually segmented regions transformed from the Z-Brain coordinate system to ZBB_{1.2} (white outlines) compared to regions previously defined in ZBB obtained by thresholding expression patterns in transgenic lines (magenta). Regions are the torus longitudinalis **(i)**, habenula **(j)**, anterior commissure **(k)** and trigeminal ganglion **(l)**.

The accuracy of the inter-atlas registration is evident when comparing the location of cells that are present in both datasets, such as those labeled by *pet1:GFP*. The Z-Brain

transformed pattern closely matches the transgene expression pattern in ZBB_{1.2} within the superior raphe (**Fig. 3.4e** - note however that unexpectedly, the line in ZBB_{1.2} also labels a set of more rostral cells not apparent in Z-Brain). Both atlases also include lines labeling the Mauthner cells. After registration, Mauthner cells in the atlases substantially overlapped, although they were several microns more medially positioned in ZBB_{1.2} (**Fig. 3.4f**). Expression in the *DAT:GFP* line in ZBB_{1.2} overlapped well with the tyrosine hydroxylase stain from Z-Brain in the pretectum (**Fig. 3.4g**), although again, the ZBB_{1.2} pattern was slightly more medial than in Z-Brain. Caudally, the *glyT2:GFP* transgenic line labels glycinergic neurons in longitudinal columns in the medulla oblongata [67]. These columns were closely aligned after ZBB_{1.2} was registered to Z-Brain (**Fig. 3.4h**).

Although best practice is to align directly to either ZBB or Z-Brain, because many researchers will have already registered data sets to either ZBB or Z-Brain, or for cases where it may not be possible to directly register a dataset, we have provided transformation matrixes and detailed instructions to quickly re-align datasets to either of the coordinate systems ([37] ; **Additional File 3.6**).

Neuroanatomical visualization

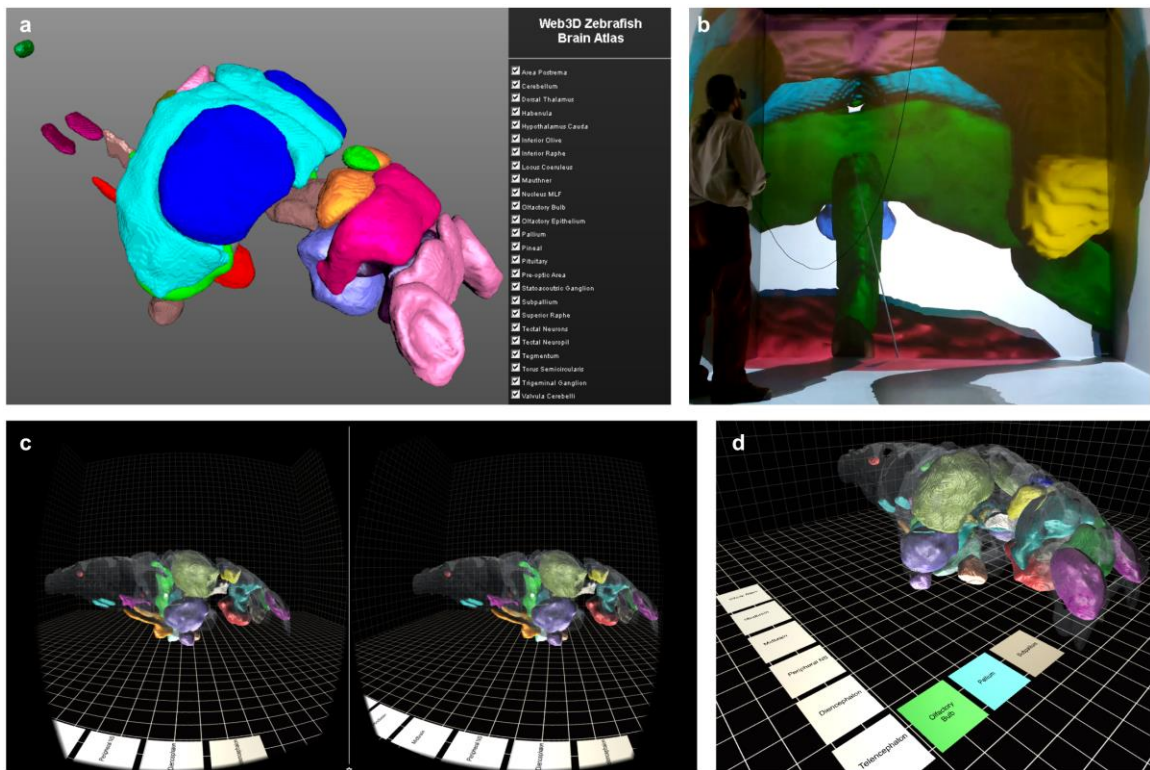
Z-Brain includes 294 masks that represent anatomically defined brain regions or discrete clusters of cells present in transgenic lines. We selected 113 of these masks that delineate neuroanatomical regions and transformed them into the ZBB_{1.2} coordinate system. We had previously defined a small number of our own anatomical masks by

thresholding clusters of neuronal cell bodies located in well-defined brain regions. However the Z-Brain masks are more comprehensive, have smoother boundaries and include both the cell bodies and neuropil for a given region (*Fig. 3.4i-l*). We therefore imported the Z-Brain masks into ZBB_{1,2}, replacing most of our existing masks. We also modified the Brain Browser software to automatically report the neuroanatomical identity of a selected pixel, or to display the boundaries of the region encompassing a selected point. The updated software and rebuilt database in ZBB_{1,2} can be downloaded from our website [38].

Finally, as the Zebrafish Brain Browser's strength is primarily in two dimensions (i.e., the visualization of horizontal, transverse, and sagittal slices through the brain), we decided to develop interactive tools to better facilitate 3D exploration. The use of 3D graphics to represent complex structure can also provide a more intuitive sensory experience that avoids cognitive bias or misinterpretation inadvertently introduced by two dimensional reductions [89,90]. By taking advantage of stereoscopy and vestibular-enhanced parallax (head tracking), the more immersive and holistic experience of Virtual Reality (VR) can also significantly improve performance of basic tasks like searching and making comparisons [91,92]. We therefore implemented our Zebrafish Brain Browser in both an open Web3D platform (X3D) and a custom game engine (Unity). First, we converted masks representing anatomical regions to meshes and built a Web3D interface using X3D to inspect the spatial relationship between different brain regions (Fig. 5a,b), available online [43]. Users can navigate within the brain using any web browser,

rotating and zooming into brain regions to better interrogate larval neuroanatomy. Second, using the Unity platform we wrote a VR app to view the brain and neuroanatomical regions. By running the app on a cell phone, and inserting it into an inexpensive Google cardboard viewer, users can 'walk into' the brain, and see from the inside the inter-relationship between neuroanatomical domains (*Fig. 3.5c,d*), available for download [44].

Figure 3.5. 3D visualization of brain browser data.



(a) X3D zebrafish brain shown in HTML5 Web browser and **(b)** Virginia Tech HyperCube (CAVE) **(c)** Virtual reality brain rendered using the Unity Game Engine for stereoscopic viewing using the Google Cardboard viewer. **(d)** In the VR browser, brain regions are selected using a menu on the floor of the virtual arena.

Discussion

Digitized data-derived brain atlases provide an opportunity to continuously integrate new information and iteratively improve data accuracy within a common spatial framework. Thus, as methods evolve and technology improves, new insights can be easily added to existing data to provide an increasingly rich view of brain structure and function. Because the entire larval zebrafish brain can be rapidly imaged at cellular resolution, it is possible to envisage an atlas that combines detailed information on cell type (including gene expression and morphology), connectivity and activity under a variety of different physiological conditions. At present, biological variability presents an obstacle, as brain regions contain multiple intermingled cell types that are not positioned in precisely the same manner between larvae. To compensate for this in the existing zebrafish brain atlases, multiple individuals of a given line are sampled and averaged to generate a representative expression pattern. Current atlases are thus essentially heat maps of gene expression or activity. Despite this spatial ambiguity, aggregating information from different sources into the same spatial framework still provides valuable indicators of cell type, gene co-expression, and neural activity under defined conditions.

Ideally different atlas projects might use the same reference brain, however in practice the choice of a reference is often dictated by study-specific experimental requirements. For example, despite the deformations introduced by fixation and permeabilization, a

fixed brain is essential for activity mapping using pERK immunohistochemistry. In contrast, we were able to take advantage of the optical transparency of larvae to rapidly scan and register several hundred individuals representing more than 100 different transgenic lines. For our purposes, the *TgBAC(slc17a6b:loxP-DsRed-loxP-GFP)nns14* line was ideal, because through Cre injection, we generated a *vglut2a:GFP* line with an almost identical pattern, allowing us to co-register lines with either GFP or RFP fluorescence. However, we have also used pan-neuronal Cerulean or mCardinal as a reference channel when green and red channels both contain useful information on transgene expression. Our work now demonstrates that it is feasible to contribute to community efforts at building an integrated map of brain structure, expression and activity, while allowing reference image selection to be guided by technical considerations.

One caveat to this conclusion is that deformable image registration can easily introduce artifacts into cell morphology if parameters are not carefully monitored and constrained. Indeed, a special challenge for brain registration in zebrafish is preserving the local morphology of neuronal cell bodies and axons, while permitting sufficient deformation to correct for biological differences and changes in brain structure arising from tissue fixation and permeabilization. Thus, while B-spline registration with CMTK produced acceptable inter-atlas alignment, it also introduced noticeable distortions into local brain structure that affected neuronal cell morphology. Such artifacts were particularly severe in ventral brain regions such as the caudal hypothalamus, and may

therefore be due to differences in ventral signal intensity between the datasets. In ZBB, in order to compensate for the increase in light diffraction with tissue depth, we systematically increased laser intensity with confocal scan progression (z-compensation). As a result, the Z-Brain and ZBB datasets are comparable in dorsal brain regions, but there is a noticeable discrepancy ventrally which may account for the loss of registration fidelity. Alternatively, although z-compensation partially corrects for reduced fluorescent intensity, there is a noticeable drop-off in image resolution in ventral regions; the resulting loss of information may lead to lower quality registration. Registration algorithms that allow parameters to vary by depth may ameliorate the effects of these physical imaging constraints.

Nevertheless, the symmetrical diffeomorphic transformation in ANTs provides a solution to these problems. For live tissue, we found parameters that allowed the ANTs SyN transform to achieve similar or better registration precision than previously achieved using CMTK, while significantly reducing distortions in tissue structure and neuronal cell morphology. In our hands, permeabilization of fixed tissue tended to produce variable changes in neuropil structure which was most salient in the optic tectum. Specifically, neuropil volume was diminished when fresh aliquots of trypsin were used for extended durations. These artifacts can be minimized by stringent oversight of reagent viridity. However, by calibrating SyN parameters to permit larger deformations, we were able to accommodate the variability introduced in tissue processing.

Currently, limitations of the SyN registration algorithm in ANTs are the large memory demands (73 GB for a single channel registration) and long computational times (3-5 hours for a single channel using 24 cores) required for registration of images with a resolution sufficient for the brain-wide visualization of neuronal morphology (e.g., 1000 x 600 x 350 pixels). For multi-channel registrations, memory demands and computation time were even greater: 106 GB for 6 channels taking over 16 hours on 24 cores. However, our present ANTs SyN parameters likely can be further optimized to reduce these demands. For instance, our parameters currently include 10 iterations of transformation matrix optimization at full image resolution. From our experience, these full resolution registration cycles do not significantly increase precision, but greatly increase computation time. Thus, computation time may be reduced by adjusting registration resolution as well as other parameters without adversely affecting registration quality. Although computational resources did not present a bottleneck for registering a small number of samples, this increase in the demands of a single registration made it difficult to optimize registration parameters as extensively as we had done previously with CMTK [1]. By reducing computation time, we would be able to explore more comprehensively the parameter space available with SyN and evaluate alternative diffeomorphic transforms available with ANTs that may provide still better registration fidelity.

An obstacle to systematically calibrating registration parameters is finding a suitable metric to quantitatively evaluate precision. This is a recognized problem, and it is

not clear that a general solution exists [93]. Here, we primarily assessed precision by measuring the distance between visually-located landmarks in the reference brain, and registered images. However, this method has two drawbacks: (1) it relies on the accuracy with which these landmarks are located, and (2) at least for our sample set, a relatively limited set of landmarks could reliably be identified. We obtained similar results when we assessed precision using cross-correlation within localized image neighborhoods that included high contrast internal image boundaries (data not shown). In registering live *vglut2a:DsRed* image stacks, we noted the trade-off between accurate global brain alignment and biologically plausible cell morphology. Thus we also used a set of measures to assess changes in the morphology of manually segmented cells (Hausdorff distance, elongation index and cell volume). Finally, we also inspected the output of every transformation to subjectively judge registration quality.

Potential implications

This study demonstrates that the ANTs diffeomorphic symmetric normalization algorithm (SyN) advances upon elastic registration for precise registration of whole brain images in larval zebrafish and is markedly better at preserving neuronal cell morphology. By systematically testing SyN registration parameters for registering images acquired using live scans, we improved the ZBB atlas. Then, after calibrating registration parameters for fixed tissue and using multi-channel optimization, we were able to align the Z-Brain atlas into the ZBB coordinate space, and vice-versa, achieving co-registration

accuracy to approximately the diameter of a single neuron. We believe that integrating the information present in each of these atlases produces a richer framework for future studies of structural and functional relationships within the nervous system. Large digital datasets such as those present in brain atlases can be used for many types of bioinformatic analysis. Z-Brain and ZBB already include software that can be used to explore the larval zebrafish brain, and we hope that integrating these datasets into a single coordinate system, will help to stimulate the development of additional computational tools and methods for querying this information.

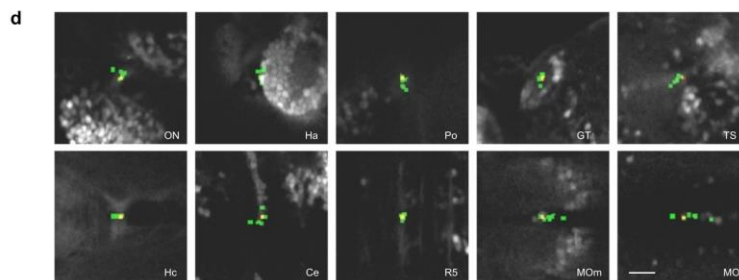
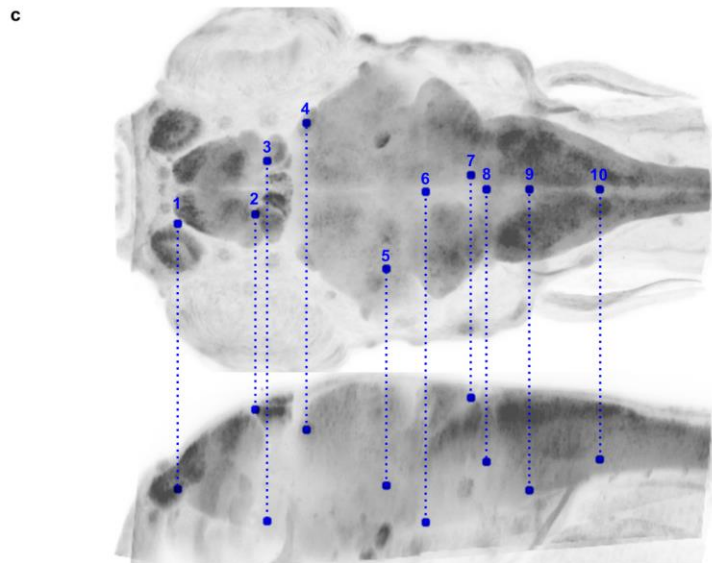
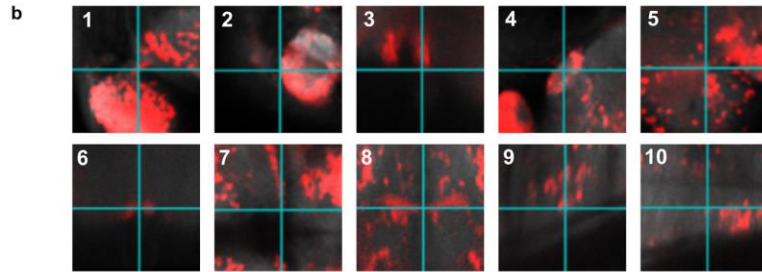
Availability of supporting data

All individual brain scans, both before and after registration to a ZBB reference brain, are available in the GigaScience repository, GigaDB [88]. The GigaDB repository also includes the set of reference brains used for ZBB [33] and the transformation matrices used to convert between ZBB and Z-Brain coordinate systems [37].

Additional Material

Additional File 3.1. Point-based landmarks for quantification of live-scan registration precision.

a #	Description	Abbrev	Position	View	MLD CMTK	MLD ANTs
1	Middle of left nerve from olfactory epithelium to brain	ON	115,251,230	H	4.7 ± 0.5	5.8 ± 1.3
2	Anterior-most extension of left habenula	Ha	245,266,98	H	9.4 ± 1.3	5.5 ± 1.1
3	Ventral-most point of right-preoptic area cell cluster	Po	263,356,288	S	6.3 ± 1.0	6.2 ± 1.0
4	Middle of neuropil zone of right tectum griseum	GT	331,423,131	H	4.5 ± 0.4	5.7 ± 0.5
5	Dorsal exit point of nerve from left torus semicircularis	TS	464,173,224	H	7.7 ± 1.5	6.6 ± 1.1
6	Mid-point of projections to caudal hypothalamus	Hc	530,305,286	T	7.9 ± 3.3	5.1 ± 1.1
7	Right medial tip of cerebellum caudal lobe tip	Ce	606,333,76	H	6.6 ± 1.3	6.9 ± 1.5
8	Middle of R5 commissure	R5	634,309,184	T	3.2 ± 0.6	2.6 ± 0.6
9	Ventral-most cluster of cells in medial/caudal medulla	MOm	707,309,233	S	13.9 ± 1.7	11.1 ± 2.6
10	Anterior-most midline cell in ventral/caudal medulla	MOc	822,308,181	S	11.9 ± 1.7	11.5 ± 2.4

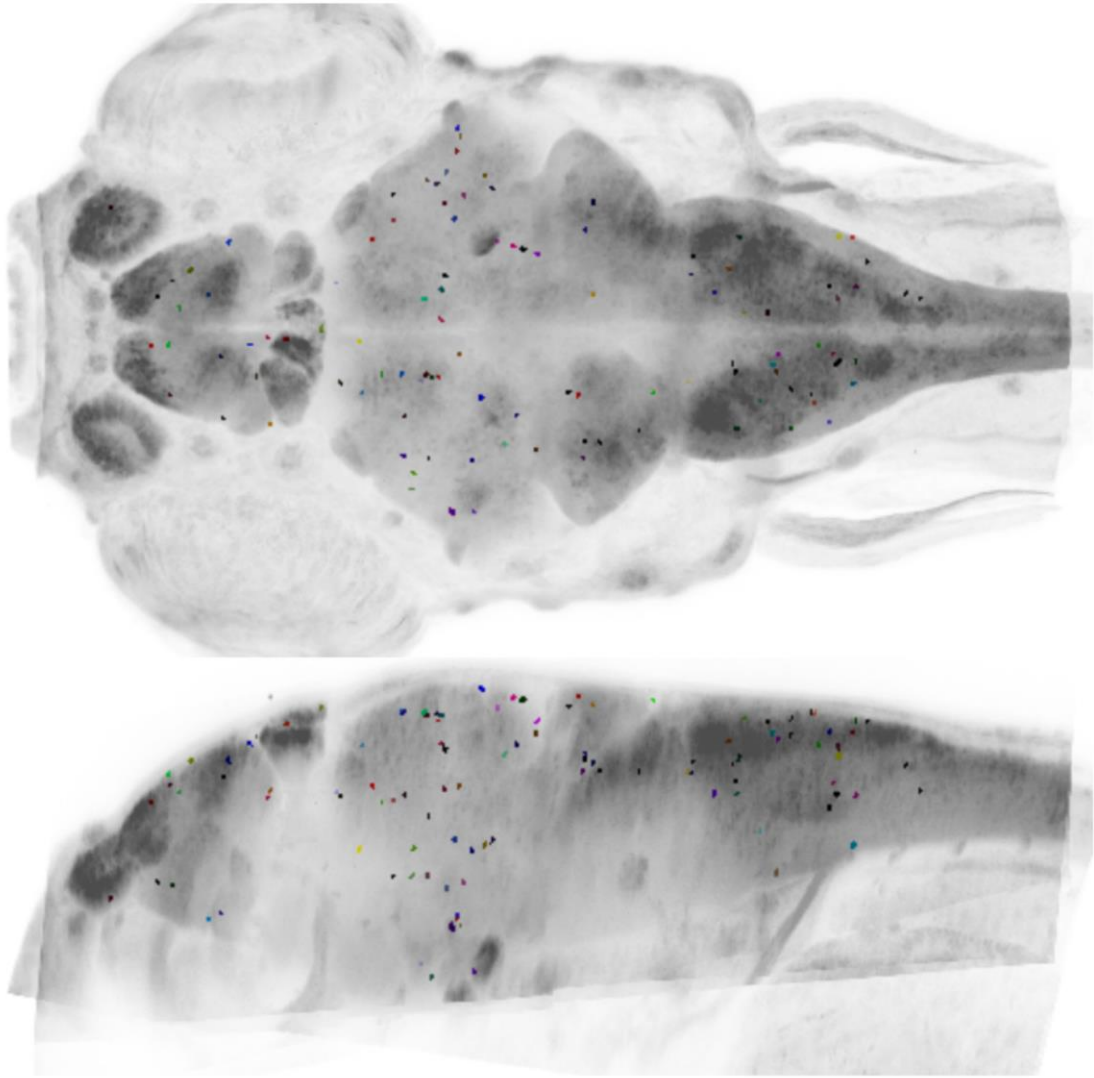


(a) Landmarks used for measuring registration precision. Position specifies the coordinates on *vglut2aZBB* (transverse, sagittal, horizontal planes). View indicates

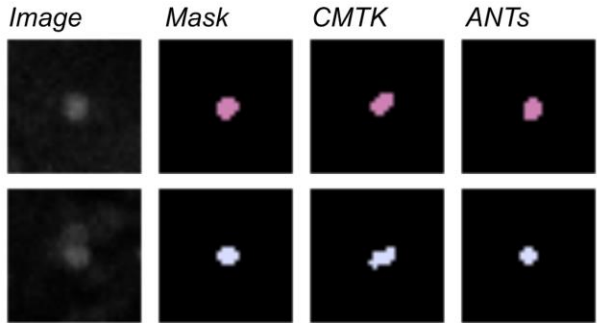
whether the image plane shown in (b) is or transverse (T), horizontal (H), or sagittal (S). MLDs represent the average precision for each landmark for the set of 6 calibration brains, after registration with CMTK or ANTs. **(b)** Images of the landmarks in vglut2aZBB (red) used for measuring precision superimposed on elavl3 (gray). **(c)** Position of the landmarks superimposed on horizontal (top) and sagittal (bottom) maximum projections of elavl3 through the brain. **(d)** Horizontal maximum projections showing the landmark point (red dot), and the position of the corresponding landmarks in the six calibration brains after registration (green dots) superimposed on vglut2aZBB. Scale bar 20 μm .

Additional File 3.2. Cells segmented for assessing distortion introduced by registration.

a



b

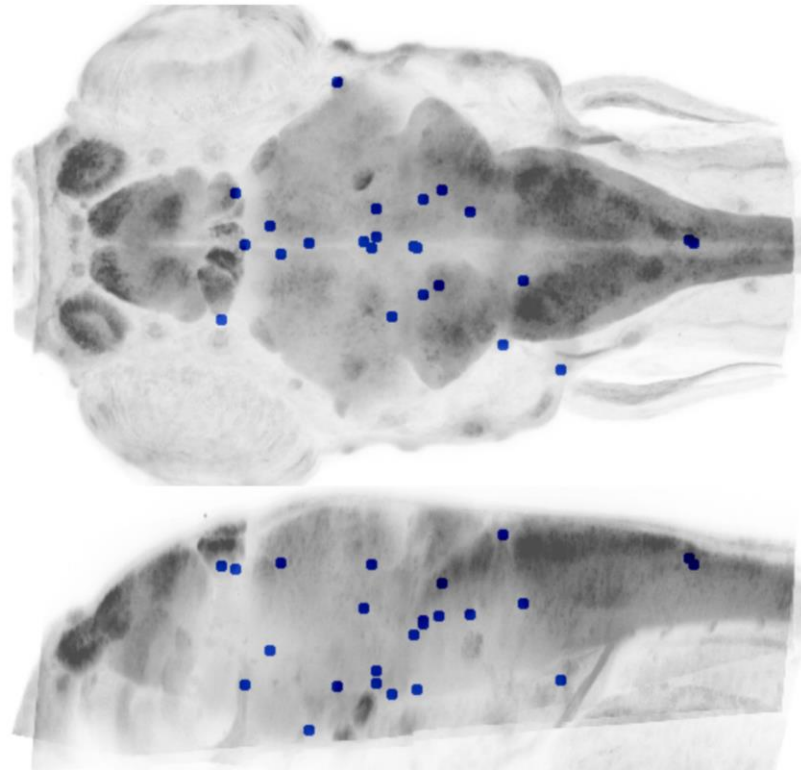


(a) Position of manually segmented cells for measurement of distortion introduced by registration. Views show the same cells (individually color coded) superimposed on horizontal (top) and sagittal (bottom) maximum elavl3 brain projections. **(b)** Two examples of cells showing (left to right): original confocal image, segmentation mask, mask after alignment with CMTK, and mask after alignment with ANTs.

Additional File 3.3. Point-based landmarks labeled by transgenic lines.

a	Transgenic line	Landmark	Coordinates	MLD CMTK	MLD ANTs
	dat:GFP	Lateral cell cluster in rhombomere 3 [R]	560,381,149	15.7 ± 3.8	12.4 ± 4.1
		Rostral tip of cell cluster in posterior tuberculum [R]	339,333,234	12 ± 3.1	12.7 ± 3.4
	j1229	MD3 [L]	663,262,174	8.7 ± 1.3	7.2 ± 1.3
		Mauthner cell soma [R]	594,351,189	5.7 ± 1.4	2.9 ± 0.3
	shox2:Gal4	Lateral cell cluster in rhombomere 3 [L]	557,258,191	18.8 ± 4.6	16.2 ± 3.9
		Midpoint of postoptic commissure [M]	307,308,278	13.4 ± 2.9	8.2 ± 1.6
	tph2:Gal4	Rostro-dorsal superior raphe [R]	459,312,181	6.7 ± 1.1	10.8 ± 0.9
		Caudal superior raphe [M]	524,308,215	15.9 ± 4.4	15.8 ± 4.1
	y234:Gal4	Lateral extent of vagal ganglion [L]	711,148,273	9 ± 2.3	6.7 ± 2.5
		Lateral extent of trigeminal ganglion [R]	427,518,280	8.7 ± 2	4.5 ± 1.2
	y244:Gal4	Lateral extent of habenula [L]	277,213,126	4.7 ± 0.8	7.7 ± 1.4
		Termination field of fasciculus retroflexus [R]	529,307,284	17.9 ± 5.8	4.6 ± 0.6
	y245:Gal4	Intersection of radial glia at mid-hindbrain boundary [M]	468,307,124	5 ± 0.8	3.9 ± 0.2
		Caudal extent of area postrema [M]	881,310,125	3.7 ± 0.2	3.9 ± 0.2
	y296:Gal4	Base of rhombomere 5 neuromast [L]	636,181,87	14.6 ± 3.6	15.9 ± 3
		Rostral tip of pituitary [M]	389,310,336	8.1 ± 2.7	4.2 ± 0.8
	y332:Gal4	Exit point fasciculus retroflexus from habenula [R]	294,376,130	7 ± 1.6	7.5 ± 1.3
		Gap in IPN neuropil [R]	475,321,277	9.2 ± 2.4	4.9 ± 1.1
	y341:Gal4	Exit point of nerve from caudal hypothalamus [R]	477,355,260	22.1 ± 6.3	6.3 ± 0.9
		Lateral tip of caudal hypothalamus [L]	496,219,290	16 ± 3.5	8.8 ± 1.3
	y351:Gal4	Ventral tip of caudal medulla cell cluster [M]	875,315,117	13.3 ± 2.6	11.9 ± 1.8
		Midpoint of posterior commissure [M]	353,299,122	7.7 ± 1.5	5.2 ± 0.6
	y359:Gal4	Exit point of nerve from trigeminal ganglion [L]	536,244,197	7.3 ± 0.3	7.2 ± 0.9
		Exit point of nerve from trigeminal ganglion [R]	537,369,200	7.3 ± 1.1	5.8 ± 1.5

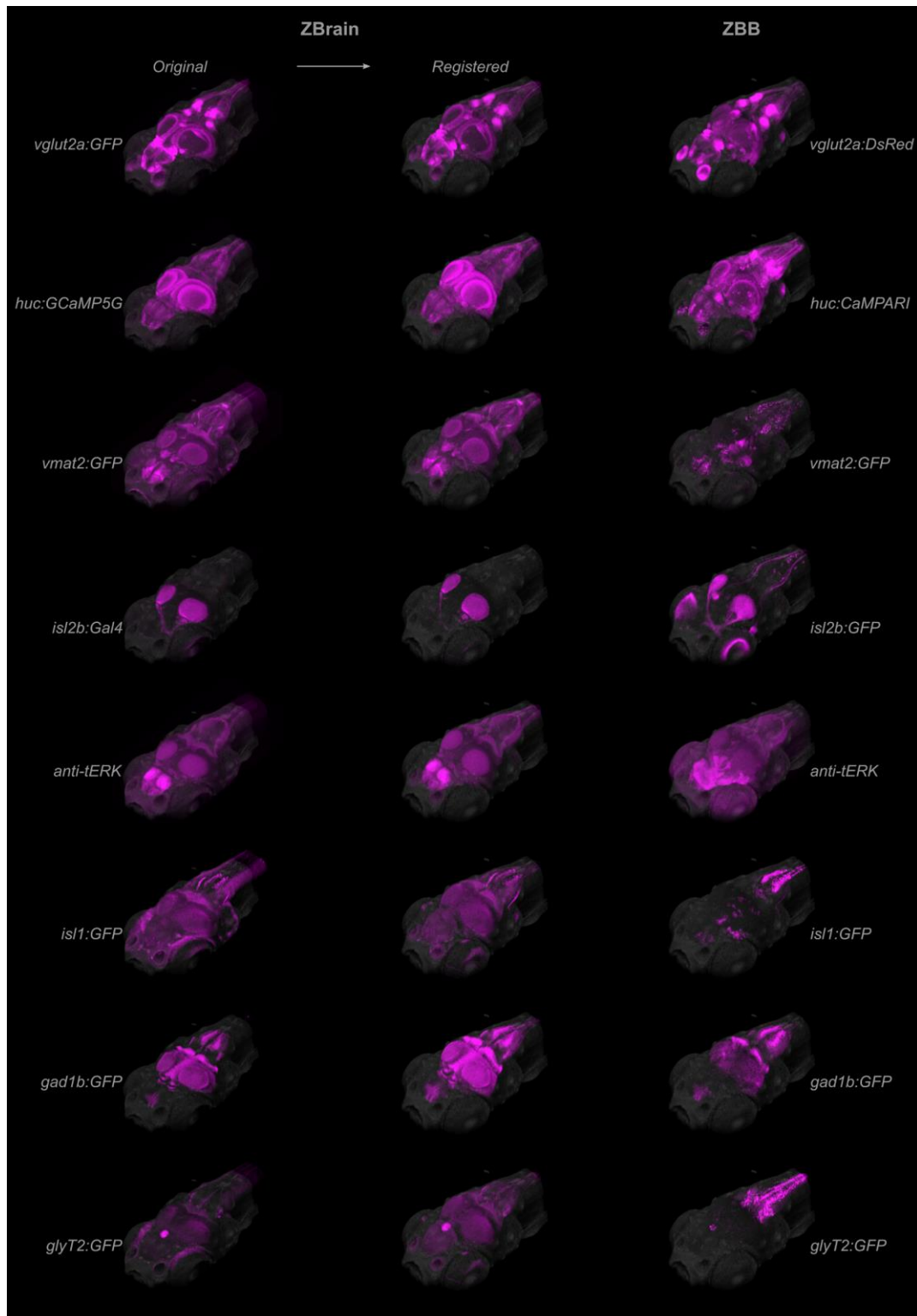
b



(a) Transgenic line landmarks used for measuring registration precision of the zebrafish brain browser atlas. Coordinates give the transverse, horizontal, sagittal position. Letter

in square brackets designates Right side [R], Left side [L], or Midline [M]. The mean and standard error of the landmark distances for the three brains per landmark are indicated for CMTK and ANTs. **(b)** Position of the landmarks superimposed on horizontal (top) and sagittal (bottom) maximum elavl3 brain projections.

Additional File 3.4. ZBB and Z-Brain expression patterns used for atlas registration.



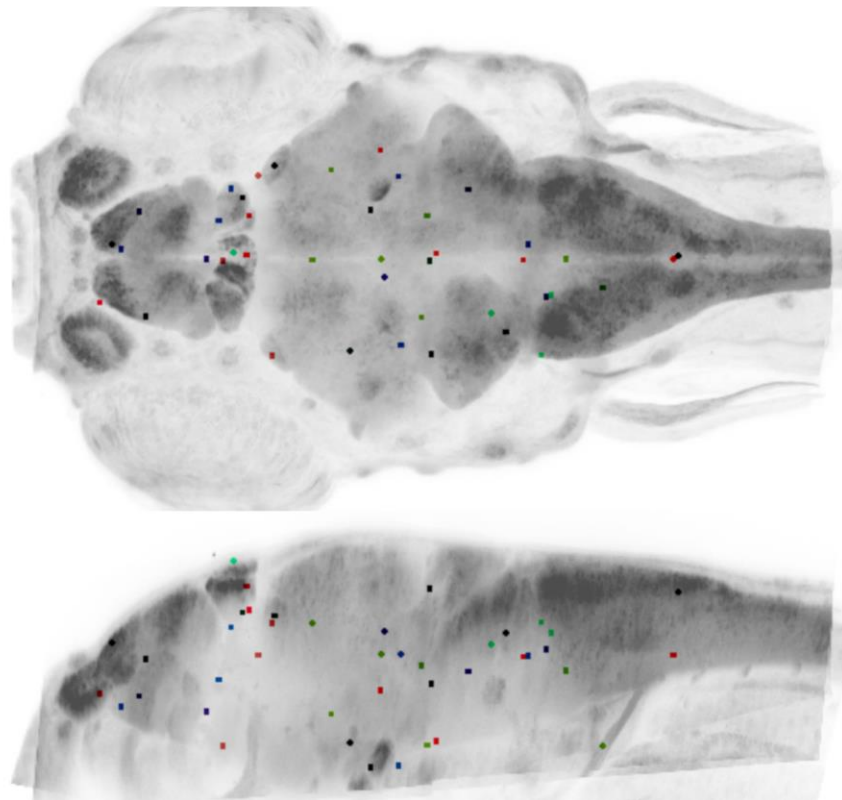
Brain Browser 3D projections of corresponding expression patterns in Z-Brain (left) and ZBB (right) used for calibrating and verifying the precision of inter-atlas registration. The top 5 patterns were combinatorially used to drive registration, while the bottom 3 were used for assessing precision. Middle images show Z-Brain patterns after registration to ZBB.

Additional File 3.5. Point-based landmarks for measuring precision of Z-Brain/ZBB co-registration.

a

Pattern	Landmark	Coordinates	Pattern	Landmark	Coordinates
gad1b:GFP	Ventral cell cluster in subpallium [R]	142,319,247	tERK	Dorsal/rostral cell cluster in olfactory bulb [R]	131,325,169
	Middle of tract lateral to preoptic area [R]	261,354,214		Caudal/lateral extent of olfactory bulb [L]	172,237,189
	Lateral extent of ventral thalamus [R]	276,393,150		Caudal/ventral tip of Hb [R]	290,382,132
	Ventral projection from H [R]	480,408,319		Middle neuropil zone tectum griseum [R]	329,421,136
	Base of dorsal tegmental cell cluster [L]	483,202,183		Medial/caudal extent hypothalamus diffuse nucleus [L]	421,195,291
	Medial cell cluster in R6 [R]	638,325,185		Medial cluster of cells in H [R]	446,367,321
glyt2:GFP	Dorsal extent pineal	279,315,69	Mid-point of commissure in valvula cerebelli	518,305,103	
	Base of commissure in R4 [L]	593,241,171	Base of tract emerging from ventral R1 [L]	520,191,219	
	Lateral extent cell cluster in R5 [L]	654,190,144	Exit point of tract from dense neuropil in R4 [L]	611,218,157	
	Caudal/medial cell cluster in R6 [L]	666,263,157	Dorsal tip of caudal MO tract	821,311,107	
is11:GFP	Lateral extent cluster in subpallium [R]	164,365,234	vglut:dsRed	Middle of nerve from olfactory epithelium to brain [L]	115,251,230
	Caudal extent of preoptic clusters [M]	246,307,253		Base of pineal	295,312,100
	Trochlear nucleus [L]	463,285,155		Exit point of fasciculus retroflexus from Hb [R]	298,360,129
	Trigeminal motor neurons [R]	565,392,204		Dorsal exit point of nerve from torus semicircularis [R]	458,440,227
	Lateral extent facial octavolateralis motor neurons [L]	660,261,177		Neuropil zone in projection to Hc [R]	526,314,289
vmat2:GFP	Dorsal/caudal midline tip of cell bands in pretectum	375,306,145	Middle of R5 commissure	634,309,184	
	Lateral cell cluster in H [R]	398,416,256	Anterior-most midline cell in ventral-caudal MO	822,308,181	
	Rostral midline of dorsal raphe	459,307,183	is12b:GFP	Middle of optic chiasm	266,305,295
	Locus coeruleus, middle of cell cluster [L]	508,236,197		Branch of optic nerve to tectum griseum [R]	309,409,184
	Exit point of dorso-caudal tract from Hc [R]	515,360,294		Middle neuropil zone tectum griseum [L]	326,189,145
	Inferior raphe, large cell cluster caudal MO	684,307,203			

b



(a) Transgenic line and tERK-stain landmarks used for measuring registration precision of registration between Z-Brain and ZBB. Coordinates are in transverse, horizontal, sagittal sections. Letters in square brackets designates Right side [R], Left side [L], or Midline [M]. Color blocks correspond to points in (b). (b) Position of the landmarks superimposed on horizontal (top) and sagittal (bottom) maximum brain projections.

Additional File 3.6. Instructions for using transformation matrices to convert between ZBB and Z-Brain coordinate systems.

Detailed steps to convert image stacks that were previously registered to Z-Brain, to the ZBB coordinate system, and vice-versa, are outlined below.

You will need:

1. To install:

- ImageJ: <https://imagej.nih.gov/ij/>
- NiFTI-1 format plugin for ImageJ: <https://imagej.nih.gov/ij/plugins/nifti.html>
- ANTS: installation directions are available at: <https://brianavants.wordpress.com/2012/04/13/updated-ants-compile-instructions-april-12-2012/>

2. The transformation matrices, available as Supplemental Data Files:

- zbtozbb_0GenericAffine.mat
- zbtozbb_1InverseWarp.nii.gz
- zbtozbb_1Warp.nii.gz

1. To convert Z-Brain images to ZBB coordinates

1.1. Invert the Z-axis of the Zbrain registered file and rotate 90 degrees left.

Using ImageJ:

Image → Transform → Flip-Z

Image → Transform → Rotate 90 Degrees left

1.2. Set the image properties.

ImageJ: Image → Properties

- Unit of length: pixel

- Pixel width: 0.7980005

- Pixel height: 0.7980005
- Voxel depth: 2.0000000

1.3. If the images have been downsampled (eg. for pERK/tERK activity maps) then resize the images to 1406 x 621 x 138

ImageJ: Image → Adjust → Size, uncheck Constrain aspect ratio

1.4. Save as NiFTI-1 format (.nii)

ImageJ: File → SaveAs → NIfTI-1

1.5. Transform the .nii file to ZBB coordinates using ANTS.

The ANTS command is, all on one line:

```
antsApplyTransforms -d 3 -v 0 -f -35000 --float -n HammingWindowedSinc  
-i ZBRAIN_FILE_TO_BE_WARPED.NII  
-r vglut2a-dsred-hb.nii  
-o OUTPUT_FILENAME.nii.gz  
-t zbtozbb_1Warp.nii.gz  
-t zbtozbb_0GenericAffine.mat
```

Notes:

- The file vglut2a-dsred-hb.nii for the -r switch is the ZBB reference brain ('refbrain.nrrd' included in the ZBB download), saved in nifti format.
- Runs with 10 Gig memory in about 10 mins.
- ANTs may try to grab all of your cores. To restrict ANTs to 16 threads before applying the transform use the bash command:
export ITK_GLOBAL_DEFAULT_NUMBER_OF_THREADS=16

1.6. (Optional) Convert the 32-bit output nii.gz file to an 8- or 16-bit tif to load into the Brain Browser.

Before converting from 32-bits, you need to adjust the contrast so that background pixels are set to zero, and the maximum signal is saturated.

ImageJ: Analyze → Histogram, check 'Stack histogram', note the Max value in the result

ImageJ: Image → Adjust → Brightness/Contrast → Set. - Then, in the pop-up window - enter minimum displayed value: 0

- enter maximum displayed value: (the Max value from histogram, above).
ImageJ: Image → Type → 16-bit
ImageJ: File → Save As → Tiff

Registering brains directly to ZBB will be more accurate. For tERK stained brains, use the tERK reference brain (terk-ants-ref-02.nii.gz) included as supplemental data with this paper, using the 'Fixed registration' parameters described in Table 1.

2. To convert ZBB images to Z-Brain coordinates

2.1. Set the image properties:

ImageJ: Image → Properties
Unit of length: pixel
Pixel width: 1.0
Pixel height: 1.0
Voxel depth: 1.0

2.2. Save as NiFTI-1 format (.nii)

ImageJ: File → SaveAs → NiftI-1

2.3. Transform the .nii file to Z-Brain coordinates using ANTS.

ANTS command is, all on one line:

```
antsApplyTransforms -d 3 -v 0 -float -n HammingWindowedSinc  
-i ZBB_FILE_TO_BE_WARPED.NII  
-r vglut2a-gfp-or.nii  
-o OUTPUT_FILENAME.nii.gz  
-t [zbtobb_0GenericAffine.mat,1]  
-t zbtobb_1InverseWarp.nii.gz
```

Notes:

- i. The file vglut2a-gfp-or.nii for the -r switch is the Z-Brain vglut2a file saved in nifti format
- ii. Runs with 10 Gig memory

2.4. Flip the Z-axis of the output file and rotate 90 degrees right.

Image → Transform → Flip-Z

Chapter 4: Neural substrates of long-latency startle response in larval zebrafish

The work presented in this chapter has yet to be published.

Abstract

Larval zebrafish respond to sudden predator movements with rapid escape responses. While intense acoustio-vibrational cues activate Mauthner cells and result in short-latency C-start (SLC) responses, weaker stimuli that fail to elicit SLCs can trigger long-latency C-start (LLC) escape responses. Although Mauthner circuitry is well known, neural substrates for LLCs have remained elusive. Through a systematic circuit-breaking screen, we identified 3 Gal4 lines (*y293Et*, *y252Et* and *y330Et*) labeling neurons critical for LLC escape. These lines drive expression in two common cell populations: adjacent to the locus coeruleus (LC), and in the dorsal hindbrain. Through laser ablation and optogenetic stimulation, we identified locus coeruleus adjacent neurons to be both necessary and sufficient for the production of LLCs. Using a novel intersectional genetic labeling method, we stochastically expressed RFP in single LC adjacent neurons, allowing characterization of their morphology and projections. This genetically-defined population of neurons were strikingly homogenous with all projecting to the same mirrored ipsi- and contralateral midbrain and hindbrain regions. Based on activation and

ablation experiments, the ipsilateral hindbrain projections are predicted to subserve LLC startle, while the contralateral neurites may feed into reciprocal inhibitory circuitry. For the first time, we have identified a core component of a neuronal circuit mediating long latency C-starts, an ethologically important behavior in zebrafish.

Introduction

Escape behavior is highly conserved and critical for survival across the animal kingdom and in fish, ‘fast start’ escape or startle responses are the principal behaviors for predator avoidance. While fast starts can be elicited by multiple modalities, responses to acousto-vibrational stimuli are the most thoroughly characterized with most research focusing on the Mauthner cell (M-cell) and associated circuitry. M-cells are large a bilateral pair of readily identifiable command-like reticulospinal neurons present in most actinopterygian fish, but also retained in some amphibians. Although M-cells are active in a range of behaviors [94,95], they are principally associated with fast start escape, the production of which they were electrophysiologically linked to in the 1960s [96].

While all circuits modulating M-cell-mediated startle are yet to be fully elucidated, primary sensory inputs and motor outputs of the M-cell are known. M-cells receive direct acousto-vibrational input from the ear through the statoacoustic ganglion as well as from the posterior lateral line. Behavioral and electrophysiological evidence suggests visual inputs are also present [97]. When these inputs reach threshold, a single spike within either M-cell is sufficient to elicit startle behavior. This spike travels

contralaterally through a large diameter axon down the spinal cord to motor neurons innervating lateral trunk muscles that following M-cell activation contract nearly simultaneously. This near simultaneous contraction causes the head and tail to rotate around the fish's center of mass resulting in the fish taking a C-like shape commonly referred to as a C-bend or C-start. This orientation bend is then followed by a burst of swimming that propels the fish forward in a directionalized escape [98].

While all fast start responses in teleost fish were initially thought to rely upon this M-cell circuit, ablation studies and high-speed behavioral analysis suggested alternative non-M-cell-mediated startle circuitry must exist. Although M-cells and their serially repeated rhombomeric homologs, MiD2cm and MiD3, are activate during startle responses [99], their collective ablation, while significantly decreasing startle performance, does not eliminate C-bend behavior [100,101]. When startle behavior is analyzed with high-speed photography, a bimodal distribution of startle responses is apparent, with the two waves commonly referred to as short-latency C-starts (SLCs) and long-latency C-starts (LLCs). Although SLCs have been shown to follow M-cell activation and be eliminated following M-cell ablation, LLC production does not correspond to M-cell activity and they persist following M-cell ablation [100]. These results suggest that an M-cell-independent alternative startle circuit capable of generating LLCs must exist. Although much is known of the circuit responsible for SLCs, virtually nothing is known of that which underlies LLC behavior.

To identify components of the circuit or circuits responsible for LLC startle, we performed a “circuit-breaking” genetic ablation screen. In this screen, Gal4 enhancer trap lines were used to drive the selective ablation of subsets of neurons and test for their potential role in startle behavior. We tested 28 Gal4 lines that cumulatively drive expression in approximately 64.6% of the larval zebrafish brain. Behavioral analysis identified three tested lines, *y252Et*, *y293Et*, and *y330Et*, in which LLC production was reduced by over 50%. Expression in these lines overlapped in two regions, just dorsal of the locus coeruleus (R1) and a neuroprogenitor region in rhombomere 6 (R2). Through selective laser ablation and optogenetic stimulation, we identified R1 as both necessary and sufficient for the production of LLC startle behavior. In tracing individual R1 neurons with a novel combinatorial genetic approach, R1 neurons were found to be strikingly homogenous, projecting bilaterally to mirrored midbrain and hindbrain regions. Based on ablation as well as activation experiments, we hypothesize that ipsilateral R1 projections activate premotor neurons responsible for LLC startle, while contralateral neurites subserve reciprocal inhibition between left and right R1 populations. For the first time, we have identified a core component of the neuronal circuit that mediates long latency C-starts, an ethologically important behavior in zebrafish.

Results

Genetic ablation in *y252Et*, *y293Et*, and *y330Et* significantly reduces LLCs

While SLC circuitry is known, neurons underlying LLC startle remain unknown (**Fig 4.1a**). To identify components responsible for LLCs, we performed a “circuit-breaking” genetic ablation screen in 28 Gal4 enhancer trap lines that based on high-resolution imaging and alignment [102] cumulatively drive expression in 64.6% of the larval zebrafish brain (**Fig 4.1b**). These enhancer trap lines were crossed to an enhanced potency nitroreductase line (*UAS:epNTR*) that with exposure to metronidazole generates a cell-impermeable cytotoxin that selectively ablates cells (**Fig 4.1c**)[103]. For behavioral testing, larvae were exposed to acousto-vibrational stimuli with the resulting behaviors recorded at 1000 fps with a high-speed camera (**Fig 4.1c, left**). In three of the tested lines, *y252Et*, *y293Et*, and *y330Et*, LLC probability was reduced by >50% (**Fig. 4.1c, right**). While LLCs were significantly reduced in all three of these lines, SLCs were significantly increased in *y252Et* and *y293Et* (**Fig 4.1d**). LLC kinematics were largely unchanged in *y293Et* and *y330Et* genetic ablations, in *y252Et* however, LLC C1 and C2 angle and maximum angular velocities were all significantly decreased (**Suppl. Fig. 4.1a**). For SLCs, C1 and C2 angle, and maximum angular velocities were all significantly reduced in *y293Et* (**Suppl. Fig. 4.1b**). Thus, with our circuit-breaking screen, we identified three Gal4 enhancer trap lines whose ablations caused defects including a significant reduction in LLCs, in addition to defects in other behavioral parameters.

Although results of our circuit-breaking screen narrows down possible neural substrates of LLCs, the sparsest of these three lines, *y293Et*, still drives expression in approximately 1% of the larval zebrafish brain. To further narrow down possible loci of LLC behavior, we compared the expression in lines with >50% LLC reduction. Although *y252Et*, *y293Et*, and *y330Et* genetic ablations may impact LLC probability through distinct circuits, alternatively ablations may affect LLCs through shared component(s) identifiable through analysis of coexpression. As Gal4 lines dependent on paired UAS reporter for visualization, the expression of *y252Et*, *y293Et*, and *y330Et* lines cannot be directly compared in the same experimental animal. Virtual overlap between expression patterns, however, can be approximated in digital atlases like the Zebrafish Brain Browser (ZBB) [76]. By calculating the expression overlap between *y252Et*, *y293Et*, and *y330Et*, we identified two regions in common between the three lines whose ablation is associated with a reduction in LLC behavior. The first region (R1), consists of a bilateral population of approximately 20 cells per side located between the locus coeruleus and cerebellum while the second region (R2) lies in a neural progenitor zone in rhombomere 6 (**Fig. 4.1e**).

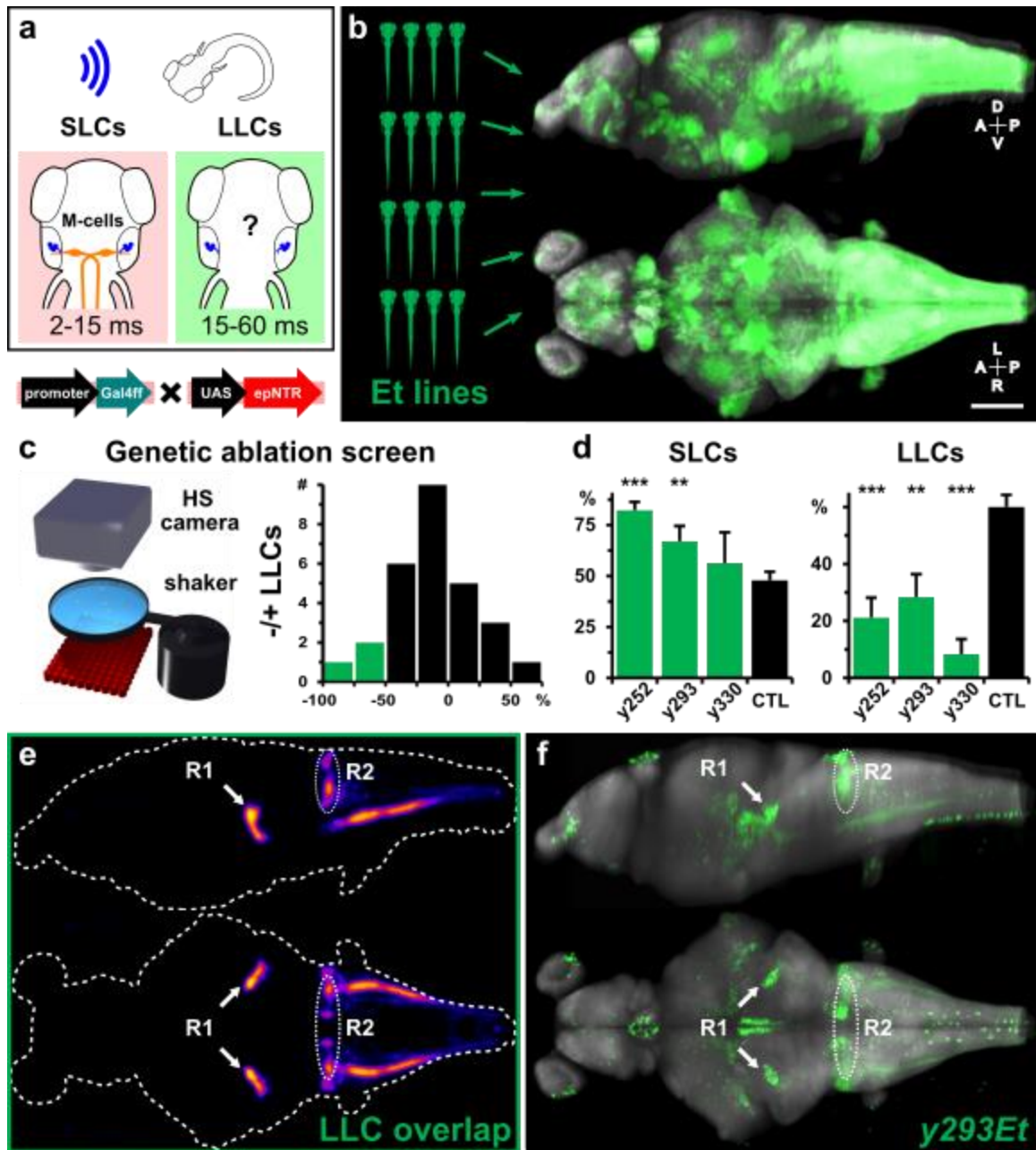


Figure 4.1. Genetic ablation of Gal4 enhancer trap lines

(a) Diagram of SLC and LLC circuits responsible for startle responses to acousto-vibrational stimuli (*above*). In SLCs, statoacoustic ganglion sensory neurons (*blue*) synapse directly onto the ipsilateral M-cell (*orange*) which projects contralaterally to motor elements responsible for a short latency (2-15ms) C-bends (*left*). In contrast, while

LLCs also rely upon statoacoustic ganglion sensory neuron input (blue), downstream central nervous system components responsible for this longer latency response (15-60ms) are unknown (*right*). **(b)** Sagittal (*top*) and dorsal (*bottom*) standard deviation projections of 28 Gal4 enhancer trap lines ablated and tested for defects in LLC behavior with cumulative enhancer trap expression (*green*) compared to larval brain morphology (*gray*). Scale bar = 100 μ m in *b,e, & f*. **(c)** Enhancer trap lines were genetically ablated by crossing to *UAS:epNTR* (*top*) and tested for startle in petri dishes mounted on a minishaker and imaged with a high-speed camera (*left*). Three of the 28 lines showed >50% LLC reduction (*right*). **(d)** While LLCs were significantly reduced in *y252Et*, *y293Et*, *y330Et* (controls: $60.1 \pm 4.82\%$ SEM vs. *y252Et*: $21.14 \pm 7.07\%$ SEM, $p=7.64 \times 10^{-5}$; *y293Et*: $28.39 \pm 7.07\%$ SEM, $p=2.4 \times 10^{-3}$; and *y330Et*: $28.39 \pm 7.07\%$ SEM, $p=7.95 \times 10^{-6}$), *y252Et* and *y293Et* ablation significantly increased SLCs (controls: $47.90 \pm 4.21\%$ SEM vs. *y252Et*: $82.13 \pm 4.11\%$ SEM, $p=1.61 \times 10^{-7}$; and *y293Et*: $67.01 \pm 7.58\%$ SEM, $p=0.037$). **(e)** Sagittal (*top*) and dorsal (*bottom*) standard deviation projections of two putative LLC regions, R1 and R2, identified by analyzing the overlap in *y252Et*, *y293Et*, and *y330Et*. R1 = superior vestibular nucleus, R2 = dorsal aspect of rhombomere 6. **(f)** Sagittal (*top*) and dorsal (*bottom*) standard deviation projections of *y293Et*, which most discretely labels R1 and R2.

Bilateral laser ablation eliminates LLCs

To test whether either of the two regions, R1 or R2, identified through analysis of the overlap of our genetic ablations were responsible on their own for the LLC reduction observed in our genetic ablations, we looked to restrict ablation to just these subdomains. More restrictive Gal4 lines or Cre lines for intersectional genetic approaches were not available to selectively test either region. Due to the small, relatively compact nature of the two regions, however, we reasoned that both could be selectively laser ablated and larvae subsequently tested for defects in behavior. As *y293Et* most discretely labeled both regions (**Fig. 4.1f**), we selectively laser ablated either R1 or R2 in *y293Et* (**Fig. 4.2a**) and tested for defects in startle behavior. Bilateral R1 laser ablation significantly reduced SLCs, but completely eliminated LLCs (**Fig. 4.2b,c**). In contrast,

R2 laser ablation did not significantly impact the probability of either LLC or SLC behaviors (*Fig. 4.2d,e*). These laser ablation results implicate R1 and not R2 in LLC behavior.

While R1 neurons appear critical for the production of LLCs, they are bilaterally distributed, suggestive that similar to other circuits (e.g., M-cell-mediated SLC startle) that the directionalized response of LLCs could be distributed between these two lateralized neural populations. To test for this, we laser ablated R1 neurons unilaterally and tested for the lateralization of startle behavior (*Fig 4.2f*). While unilateral laser ablation did not significantly change SLC or LLC probability (data not shown) and did not significantly impact the directionality of SLCs (*Fig 4.2g*), unilateral laser ablation significantly biased LLC behavior towards the un-ablated side (*Fig 4.2g*). This suggests that R1 neurons produce a lateralized response ipsilateral to the location of their cell bodies.

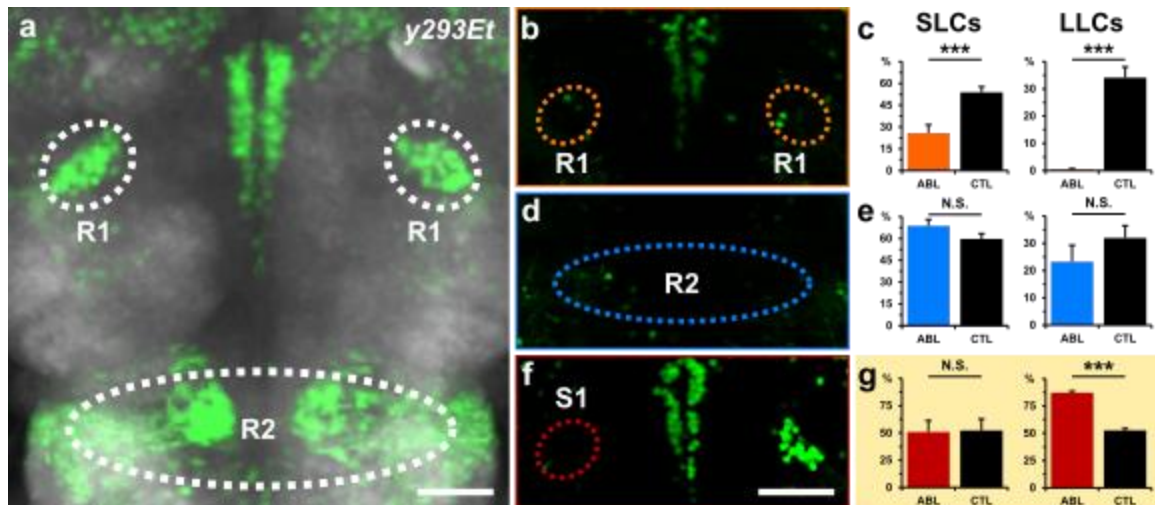


Figure 4.2. Laser ablation of regions associated with LLC startle

(a) *y293Et* discretely labels neurons in R1 and R2, two regions associated with LLCs identified in our genetic ablation screen. (b) Neurons in either the R1 or R2 were laser ablated and larvae tested for startle response behavior. (b) R1 neuron ablation reduced SLCs by 50%, while completely eliminating LLCs ($n=8$, LLCs: $0.37 \pm 0.37\%$ SEM, $n=8$ vs. $34.10 \pm 3.94\%$ SEM for controls, $p=0$; SLCs: $25.99 \pm 5.57\%$ SEM, $n=8$ vs. $53.90 \pm 3.77\%$ SEM for controls, $p=0.00012$) (d), while R2 ablation did not significantly impact either startle behavior ($n=16$; SLCs: $68.76 \pm 4.28\%$ SEM vs. $59.67 \pm 3.67\%$ SEM for controls, $p=0.11$; LLCs: $23.26 \pm 5.99\%$ SEM vs. $31.95 \pm 4.51\%$ SEM for controls, $p=0.25$) (e). Unilateral SVN ablation (f) did not significantly impact the LLC production, but resulted in the directional biasing of LLC startle behavior ($n=14$; SLCs: $50.20 \pm 10.32\%$ SEM vs. $51.66 \pm 4.25\%$ SEM for controls, $p=0.88$; LLCs: $86.23 \pm 3.03\%$ SEM vs. $52.13 \pm 1.65\%$ SEM for controls, $p=7.8 \times 10^{-13}$) (g). All scale bars = $40\mu\text{m}$.

Optogenetic stimulation of vestibular nucleus elicits startle

Bilateral R1 laser ablation results suggests the necessity of R1 in acousto-vibrationally produced LLCs. To test, however, whether R1 neurons are also sufficient to directly drive LLC startle, we expressed the channelrhodopsin variant ChEF [104] in *y293Et* neurons and selectively unilaterally stimulated R1 neurons through a digital mirror device (DMD) (Fig 4.3a). Unilateral illumination of ChEF positive R1 neurons

produced behavioral responses in 54.59% of trials, eliciting a range of behaviors, from twitches to fictive swimming to full body flexions (*Fig 4.3b*). The production of both fictive swimming as well as C-bends was significantly elevated compared to ChEF negative controls (*Fig 4.3c*). In contrast, unilateral illumination of ChEF negative R1 neurons failed to elicit any behavioral responses at comparable stimulus durations. The production of C-bends following the selective unilateral stimulation of ChEF positive R1 neurons suggests that the activation of R1 neurons is sufficient for the production of LLC-like C-bend behavior. Finally, C-bends resulting from unilateral optogenetic R1 stimulation preferentially elicited ipsilateral C-bends (ipsilateral: $76.62 \pm 6.02\%$ SEM vs. contralateral: $23.38 \pm 6.02\%$ SEM, $p=0.0031$) (*Fig 4.3d*). This observation dovetails well with unilateral R1 ablations where LLCs were directionalized toward the un-ablated side. Both observations suggest that R1 neurons project ipsilaterally where they either directly or indirectly excite motor elements responsible for driving ipsilateral C-bends.

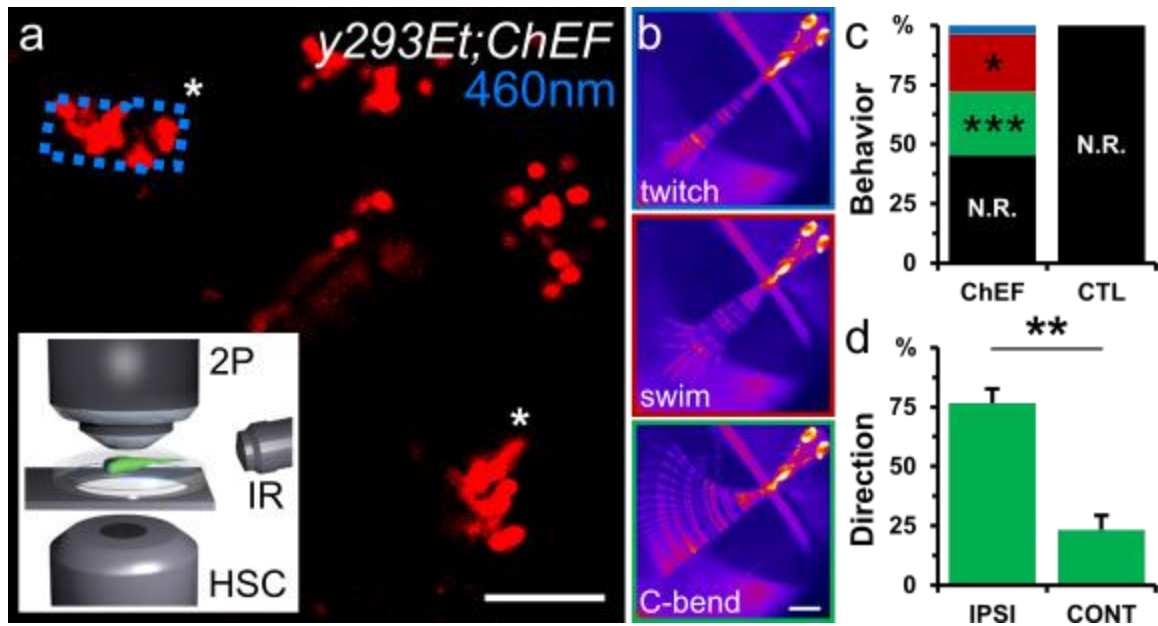


Figure 4.3. Optogenetic stimulation of *y293Et* elicits startle responses

(a) Example image of R1 neurons (*asterisks*) in *y293Et;UAS:ChEF-mCherry* larvae (*red*) unilaterally stimulated at 460 nm by a digital mirror device (DMD) (*dashed blue box*) for 10-100ms. Larvae were embedded with tails free and 2-photon imaged and stimulated from above, while infrared illumination (IR) allowed for larvae to be visualized and behavior read out from below (insert). *Scale bar = 40 μ m*. (b) Examples of behaviors, twitches, swims, and C-bends, elicited by optogenetic stimulation of R1 neurons in ChEF positive larvae. *Scale bar = 500 μ m*. (c) In contrast, ChEF negative controls failed to display any of these behaviors with similar patterned illumination (*n*=8; swimming: $24.26 \pm 7.12\%$ SEM vs. $0.00 \pm 0.00\%$ SEM for controls, *p*=0.88; C-bends: $26.71 \pm 2.09\%$ SEM vs. $0.00 \pm 0.00\%$ SEM for controls, *p*= 7.8×10^{-13}). (d) Unilateral R1 stimulation preferentially produces ipsilateral C-bends.

R1 neurons project bilaterally in both the midbrain and hindbrain

To confirm the existence of ipsilateral projections as well as to potentially identify additional circuit components upstream or downstream of R1 neurons, we visualized R1 projections by crossing *y293Et* to a membrane-tagged fluorescent marker (UAS:lynTagRFPT) (*Fig 4.4a*). While *y293Et* sparsely labels less than 1% of neurons in

the larval zebrafish brain and R1 projections can be seen descending ventrally, here they are joined by mediolateral projections emanating from the superior raphe (**Fig 4.4a, arrowheads**), labeled in *y293Et* due to inclusion of a *tph2* promoter, which makes it difficult to unambiguously trace individual R1 projections. Nevertheless, by comparing *y293Et* projections to those in *y228Tg* (**Fig 4.4b**), a *tph2* Gal4 driver line lacking discernable enhancer trap expression, prominent fiber tracts in the lateral hindbrain potentially belonging to R1 neurons are apparent (**Fig 4.4a, square brackets**).

To selectively and unambiguously visualize the morphology of individual R1 neurons, we crossed *y293Et* to a UAS reporter with B3 recombinase recognition sites [105] as well as a heatshock-inducible B3 recombinase (**Fig 4.4c**). While functional in larval zebrafish, B3 is inefficient and its activation results in stochastic recombination in a subset of cells (Kathryn Tabor, personal communication). For our purposes, however, this stochasticism is beneficial, and allows for the sparse labeling of random subsets of neurons. Thus, following a brief heatshock, we were able to stochastically label subsets of *y293Et* neurons and in larvae where the stochastic expression labeled R1 neurons, unambiguously trace the projections of individual R1 neurons.

R1 neurons projected ventrally through the locus coeruleus below which their neurites bifurcated and projected both laterally and medially. The lateral neurites from R1 neurons arborized locally in the midbrain below the eminentia granularis (EG) while medial neurites split again into a projection continuing medially across the midline as well as one that projected back ipsilaterally into the caudal hindbrain. The midline

projection crossed through the superior raphe and extended below the contralateral R1 before splitting into contralateral midbrain and hindbrain projections (*Fig. 4.4d,e*). Although *y293Et* R1 are genetically defined, they may consist of a heterogeneous population of functionally and morphologically distinct subgroups. Surprisingly, this complex quadripartite morphology was consistent across all observed (n=20) as well as traceable (n=5) neurons. This suggests that genetically-defined R1 neurons critical for LLC startle behavior are highly morphologically homogenous (*Fig 4.4f,g*).

Despite R1 neurons having highly conserved structure (i.e., ipsilateral and contralateral projections to both the midbrain and hindbrain), two morphological characteristics appear variable: (i) the level to which the neurons project into the caudal hindbrain and (ii) whether neurites project into the EG and if so whether this projection was ipsi- or contralateral. While all neurons projected into the posterior half of the hindbrain (R7-8), their point of termination varied among neurons as well as between ipsi- and contralateral projections. And while some neurons projected only to the start of R7, others projected all the way to the start of the spinal cord (*Fig 4.4g*).

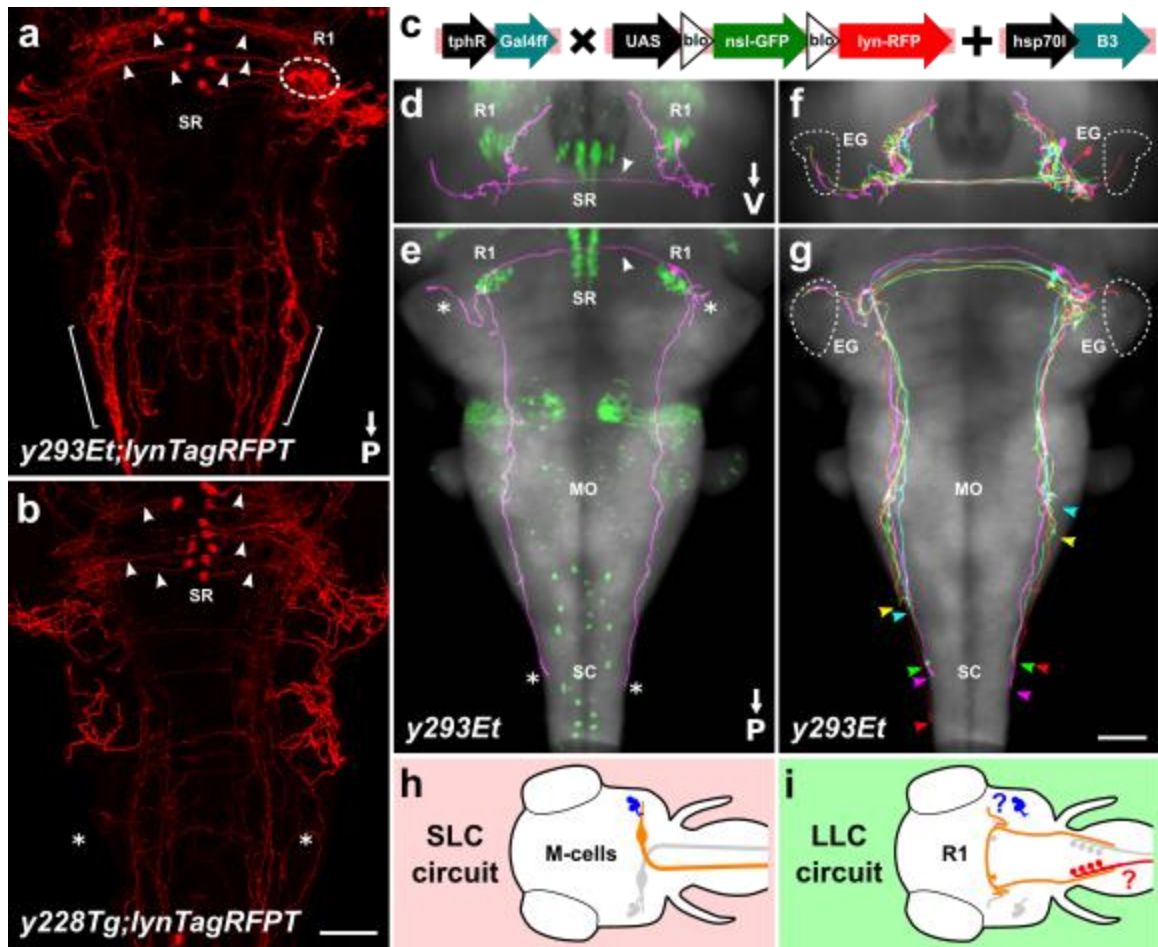


Figure 4.4. Morphology of individual R1 neurons associated with LLCs

(a) Maximum projection of *y293Et;UAS:lynTagRFPT* showing superior raphe (SR) fiber projections (*arrowheads*) projecting toward the R1 (*dashed circle*). *y293Et* has additional lateral hindbrain projections (*brackets*) not present in *y228Tg*. (b) Maximum projection of *y228Tg;UAS:lynTagRFPT* showing absence of lateral fibers (*asterisks*). (c) *y293Et* was crossed to *UAS:blo-nsI-GFP-blo-lynTagRFPT* and *hsp70l:B3* to stochastically membrane label neural subsets. A coronal (d) and dorsal (e) standard deviation projection of a representative R1 neuron (*magenta*) aligned to the *y293Et* (*green*) with overall larval brain morphology in gray (*elavl3:Cer*). A coronal (d) and dorsal (e) standard deviation projection with 5 traced R1 neurons in false color (*red, green, cyan, magenta, and yellow*). (h) Diagram of the SLC circuit with M-cell (*orange*) for comparison to LLC circuit. (i) Diagram of proposed LLC circuit: R1 neurons (*orange*) receive contralateral acousto-vibrational sensory inputs through an unknown pathway (*blue question mark*)

and drive LLC behavior ipsilaterally through unknown hindbrain motor elements (*red question mark*). Scale bars = 40 μ m. Scale of a same as b; scale of d, e, and f, same as g.

Discussion

In this work, we used a “circuit-breaking” genetic ablation screen to identify regions in the larval zebrafish brain involved in LLC startle behavior. By comparing expression in Gal4 lines whose ablation strongly reduced LLC startle probability, we identified two regions, R1 and R2, potentially associated with LLCs. Laser ablation and optogenetic stimulation of these neurons showed that neurons in the R1, a bilateral population of neurons dorsal to the locus coeruleus in rhombomere 1, are both necessary and sufficient for LLC behavior.

The bilateral distribution of R1 neurons is suggestive of behavioral lateralization, which we confirmed through unilateral ablation and unilateral optogenetic activation. Unilateral ablation produced a significant contralateral bias in LLCs, while unilateral activation resulted preferentially in ipsilateral LLCs. This suggests that R1 neurons project ipsilaterally to activate either downstream motor neurons or directly activate ipsilateral motor elements. While these optogenetic and ablation experiments biased the direction of LLC behavior, neither resulted in the complete loss of a contralateral LLC response. While this could be due to incomplete contralateral R1 ablation or nonspecific contralateral optogenetic activation; alternatively, while the majority of R1 neurons may excite ipsilateral C-bends, a subset of R1 neurons may in fact be capable of contralateral rather ipsilateral C-bend activation.

SLC startle is the result of the sensory aggregation and a single spiking of the M-cell where a single spike is capable of eliciting behavior. In contrast, we do not know how sensory information is aggregated, encoded, and transmitted for the production of LLC startle by R1 neurons. Similar to M-cells, R1 neurons may be able to individually elicit startle or alternatively the collective activity of some fraction of the R1 population may be necessary in order for LLCs to be performed. Additionally, while SLC behavior is all or none due to it being the product of a single M-cell, the ~20 R1 neurons may be a mechanism for the more graded or variable response of LLCs. Whether a single R1 neuron is sufficient to elicit startle behavior was not assessed in this work, but could be addressed with more spatially constrained optogenetic stimulation or by restricting optogenetic protein expression to a single cell in a manner similar to our stochastic labeling of individual R1 neurons.

In order to understand how R1 neurons encode information, they will need to be recorded from. While M-cells can be interrogated electrophysiologically, the size and location of R1 neurons make them less amenable to direct electrophysiological recordings. Imaging with calcium or voltage indicators; however, provide an attractive alternative to electrophysiology. Unfortunately, neither of our Gal4 lines that selectively label R1 (i.e., *y293Et* and *y330Et*) drove sufficient GCaMP6s expression to accurately measure R1 activity. The identification of additional Gal4 lines that selectively label R1 or generation of stronger UAS calcium or voltage reporter lines would resolve this current limitation.

Upstream and downstream components of an LLC circuit

We selectively labeled and traced individual R1 neurons to identify potential downstream targets as well as upstream sensory input sources of R1 neurons. Although the polarity of R1 neuron neurites remains unknown, projections from individual R1 neurons split while descending through the LC. The first of these projections arborizes locally in ipsilateral rhombomeres 1 and 2, while the second projection gives rise to three neurites: a contralateral midbrain projection, as well as ipsi- and contralateral hindbrain projections. Given its morphology, we predict this first local ipsilateral neurite, i.e., that projecting locally into rhombomere 1 and 2, is a dendritic arborization where the R1 neurons receive contralateral auditory as well as potentially other sensory inputs. The less branched morphology of the remaining projections, i.e., contralateral midbrain as well as contra- and ipsilateral hindbrain neurites, is suggestive of axon morphology. Based on the directionality of C-bends resulting from optogenetic stimulation, we suspect that this ipsilateral hindbrain projection excites hindbrain motor neurons in rhombomeres 7 and 8, which are in turn responsible for the initial C-bend contraction of LLC startle. This is yet to be experimentally confirmed, however. The possible function of mid- and hindbrain contralateral projections is less clear. Given the criticality of escape behavior the necessity for inhibiting incompatible concurrent contralateral behaviors, it is possible that these projections connect to inhibitory circuits responsible for suppressing such incompatible concurrent contralateral behaviors.

R1 neurotransmitter identity

The identification of the neurotransmitter used by R1 neurons would help us elaborate on possible mechanisms of LLC circuit function and with transgenic lines labeling genetically defined neurotransmitter neuron populations, neurotransmitter identification would seem trivial. Thus far, however, we have been unsuccessful in characterizing the neurotransmitter identity of R1 neurons (*Suppl. Fig 4.2*). While transgenic lines with neurotransmitter-associated promoters have been invaluable for visualizing neurotransmitter identities, they do not necessarily faithfully recapitulate neurotransmitter expression. Consequently, while *gad1b*, *glyT2*, *vachta*, *vglut2a*, and *vmat2* transgenic lines fail to label R1 neurons, they may nevertheless prove to be GABAergic, glycinergic, cholinergic, glutamatergic, or monoaminergic respectively. Furthermore, many of these genes have paralogs that while not predominantly expressed in the brain could be involved in neurotransmitter synthesis in select neural subpopulations and one such paralog could be responsible for neurotransmitter synthesis in R1 neurons. Alternatively, less common neurotransmitters may be expressed in and be primarily responsible for R1 neuron function instead.

R1 neuron morphological variability

R1 neurons were strikingly homogenous in their overall morphology, however, subtle differences existed primarily in the extent of their projections. This variability was seen in two areas in particular. All traced R1 neurons projected both contra- and ipsilaterally into the hindbrain, but the depth at which they penetrated into the hindbrain varied. While three traced neurons projected to the beginning of the spinal cord, two

others only projected into the start of rhombomere 7 ipsilaterally. Variability was also seen in the extent to which neurons projected contra- vs. ipsilaterally. Two neurons projected to similar contra- and ipsilateral locations, however, the other three projected noticeably further contralaterally. Whether this variability has a functional significance is yet to be explored. Finally, a projection into the EG was not universally seen, but present in three of five traced neurons. Although this projection was always on side and not the other, it was contralateral in two neurons and ipsilateral in one neuron. The remaining two neurons failed to project into the EG either contra- or ipsilaterally.

The variability in R1 projections, particularly in the hindbrain where neurites terminated anywhere from rhombomere 7 to the start of the spinal cord, suggests that different R1 neurons may synapse onto non-overlapping groups of motor elements. Given the less stereotyped nature of LLCs compared to SLCs, this potential variability in the innervation could provide a simple mechanism for achieving this variability. Alternatively, the variability in R1 neuron morphology could simply be an artifact of the developing nature of the larval zebrafish where this morphological variability is simply due to a staggered maturation of R1 neurons with those that fail to project to the spinal cord or into the EG simply being immature neurons yet to be fully integrated into the LLC circuit.

LLC motor elements

As R1 neurons only project into the hindbrain and not down the spinal cord, they cannot directly elicit LLC startle behavior, but instead likely synapse onto hindbrain

motor elements responsible for initiating LLCs. While the identities of these motor elements are unknown, motor neurons adjacent to R1 hindbrain projections are likely candidates. Tabor et. al showed that overexpression of an exogenous voltage-gated sodium channel ($SCN5\alpha$) in such a population (*y270Et*) preferentially influenced LLC kinematics [29]. Strikingly, this subpopulation of reticulospinal motor neurons is juxtaposed with the R1 neuron projections. Such lines will have to be screened for a more direct role in LLC startle behavior and their possible connection to R1 neurons identified to elaborate on the motor side of a LLC circuit.

Methods

Animal Husbandry

Gal4 enhancer trap and transgenic lines used in this study were maintained in a Tubingen long fin strain background. Embryos were raised in E3 medium supplemented with 1.5 mM HEPES pH 7.3 (E3h) at 28C on a 14 h:10 h light:dark cycle with medium changes at least every 2 days. All in vivo experimental procedures were conducted according to National Institutes of Health guidelines for animal research and were approved by the NICHD animal care and use committee.

Transgenic Lines

Details on the generation of Gal4 enhancer trap lines *y252Et* (from [31]), *y240Et*, *y245Et*, *y249Et*, *y252Et*, *y275Et*, *y279Et*, *y293Et*, *y294Et*, *y298Et*, *y300Et*, *y307Et*,

y310Et, *y311Et*, *y320Et*, *y323Et*, *y326Et*, *y329Et*, *y330Et*, *y334Et*, *y341Et*, *y345Et*, *y358Et*, *y364Et*, *y375Et* (all from [76]), and *y444Et* (previously unpublished) have previously been described [22]. Briefly, enhancer trap lines contain either basal *cfos*, *SCP1*, or *tph2* (tryptophan hydroxylase) [47] promoter sequences upstream of Gal4ff. Several lines also include a REx2 motif consisting of juxtaposed neuronal restrictive silencing elements that are incorporated to restrict expression to the nervous system.

Gal4 enhancer trap expression patterns were visualized and maintained using the *Tg(UAS-E1b:Kaede)s1999t (UAS:Kaede)* reporter line [11] and crossed to nitroreductase lines (i.e., *Tg(UAS-E1b:BGi-epNTR-TagRFPT-oPre)y268Tg* [29], *Tg(UAS:epNTR-TagRFPT-utr.zb2) (UAS:epNTR-UTR.zb2)*, *Tg(UAS:epNTR-TagRFPT-utr.zb3)y362Tg (UAS:epNTR-UTR.zb3)* [76] for cell-specific genetic ablation.

To determine the neurotransmitter identity of neurons, enhancer trap lines were crossed to *TgBAC(slc17a6b:loxP-DsRed-loxP-GFP)nns14 (vglut2a:DsRed)* [36], *Tg(slc6a3:EGFP)ot80 (dat:GFP)* [60], *Tg(slc6a5:GFP)cf3 (glyt2:GFP)* [64], *TgBAC(gad1b:GFP)nns25 (gad1b:GFP)* [20], and *Tg(pou4f1-hsp70l:GFP)rw0110b (vachtb:GFP)* [106]. *Gt(T2KSAG)j1229* [28]. *Tg(gfap:GFP)mi2001 (gfap:GFP)* [63] was used for identification of neural progenitor cells.

Imaging

Embryos were raised in E3h media containing 300 μ M N-Phenylthiourea (PTU) starting at 8–22 hpf to suppress melanophore formation. After this timepoint, PTU was

changed at least every 48 hrs. At 6 dpf, larvae were anesthetized in 0.24 mg/mL tricaine methanesulfonate (MS-222) for 3 min and mounted in 2.5% low melting point agarose in 3D printed plastic inserts (ABS from Stratasys or clear resin from FormLabs) within #1.5 thickness (0.17 ± 0.005 mm) cover glass bottom cell culture chambers (Lab-Tek II 155379).

For imaging, an inverted laser-scanning confocal microscope (Leica TCS SP5 II) equipped with an automated stage and 25x/0.95 numerical aperture apochromatic water immersion lens (Leica # 11506340) was used to acquire confocal stacks of transgenic fish and immunofluorescently labeled samples. A 488nm argon laser line and a 561nm diode-pumped solid state (DPSS) laser were used to excite fluorophores with channels acquired simultaneously and laser compensation over the z-dimension. To minimize cross-channel contamination, dye separation was performed in the Leica acquisition software (Leica Application Suite—Advanced Fluorescence, LAS AF) with coefficients based on published spectra of imaged fluorophores and the spectral windows used for acquisition.

Laser ablations

Laser ablations of subsets of fluorescently-expressing neurons were performed at 4 dpf in larvae raised in PTU. Following ablation, larvae were raised in E3h until behavioral testing at 6 dpf. Laser ablations were performed on an upright laser-scanning confocal microscope (Leica TCS SP5 II) equipped with a multi-photon laser (Spectra-Physics MaiTai DeepSee), automated stage, and 20x/1.00 numerical aperture

apochromatic water dipping lens (Leica # 11507701). A 488 nm argon laser line was used to visualize target cells and confirm ablation, while the multi-photon laser tuned to 800 nm was used for selective laser ablation. Following behavioral testing, successful ablations were confirmed by confocal microscopy with only larvae with near to complete ablation of R1 neurons (i.e., 3 cells or less on either side remaining) included for analysis.

Immunohistochemistry

For pERK and tERK labeling, larvae were fixed overnight at 4°C in PBS with 4% paraformaldehyde (PFA) and 0.25% Triton X-100. Samples were then washed in PBS containing 0.1% Triton X-100 (PBT) 3 times for 5 min. For antigen retrieval, samples were incubated in 150 mM Tris-HCl pH 9.0 for 5 min, followed by 15 min at 70°C and washed in PBT 2 times for 5 min [84]. Samples were then permeabilized on ice in fresh 0.05% trypsin-EDTA for no more than 5 minutes. If pigmented, samples were incubated in PBT with 1.5% H₂O₂ and 50 mM KOH for 15 min, rinsed 2 times in PBT and washed again for 10 min. Samples were then blocked in PBT containing 5% normal goat serum (NGS) and 0.2% bovine serum albumin (BSA) for 1 hr before incubation at 4°C with tERK and pERK antibodies (4696 & 4370, Cell Signaling) diluted 1:500 in PBT with 5% NGS and 0.2% BSA for a minimum of 6 hr. Samples were then washed with PBT 4 times for 30 min before incubation at 4°C for a minimum of 2 hr with fluorescent secondary antibodies (Alexa Fluor 488 and 548) diluted 1:1000 in PBT with 5% NGS and 0.2% BSA. Samples were finally rinsed 4 times for 30 min prior to imaging.

In situ hybridization

Antisense RNA probes for *vachtb* were generated from a cDNA containing plasmid. The plasmid was linearized with EcoRI and cut DNA cleaned (Qiaquick PCR purification kit, Qiagen) prior to Digoxigenin-tagged RNA synthesis with T7 polymerase (SP6/T7 Transcription kit, Roche) for 2 hrs at 37°C. Template DNA was then removed by incubation with DNase I (Roche) for 20 min at 37°C. Subsequently, RNA was precipitated with LiCl solution (Ambion) for 30 min at -80°C, centrifuged (15min, 4°C, 16,100 g), supernatant removed, air dried, and redissolved in 100 uL ultra pure H₂O. Finally, RNA integrity was checked on a 1.5% agarose gel and RNA diluted to 50ng/uL in hybridization buffer (50% deionized formamide, 0.1% Tween 20, 5x SSC, 9.2 mM citric acid, 500 ug/mL torula RNA, 50 ug/mL heparin in DEPC water, pH 6) and stored at -20°C until use.

At 3 dpf, *y293-Gal4;UAS:UBCi-blo-nls-emGFP-blo-lynTagRFP* larvae were fixed overnight at 4°C in PBS with 4% PFA and 0.25% Triton X-100. Samples were then washed in PBT 3 times for 5 min. Samples were serially dehydrated into 100% methanol and stored overnight at -20°C before rehydrating into PBS with 0.1% Tween 20 (PBTw). Samples were then permeabilized with Proteinase K (1:1000 dilution of 20ug/mL, Roche) for 60 minutes at 37°C before rinsing twice in PBTw and refixing in PBS with 4% PFA and 0.25% Triton X-100 for 20 min at room temperature (RT). Samples were washed 3 times for 5 min before a 2 hr incubation in hybridization buffer at 68°C. This was

followed by a 14 hr incubation with 100 ng of the antisense Digoxigenin-tagged RNA probe diluted in hybridization buffer. RNA probes were retrieved and unbound probes washed away in 50% formamide and SSC, twice, for 30 min at 68°C. This was followed by a 5 min rinse in hybridization wash buffer (50% formamide, 5x SSC, and 0.25% CHAPS (3-[(3-Cholamidopropyl)dimethylammonio]-1-propanesulfonate hydrate)) and three 30 min washes at 68°C. Samples were then washed in a 1:1 mixture of hybridization wash buffer and 2x SSC for 15 min at 68°C followed by a 1:3 ratio of hybridization wash buffer and 2x SSC for 15 min at 68°C. Next, samples were rinsed for 15 minutes in 2x SSC containing 0.25% CHAPS. Finally, samples were washed in 0.2x SSC containing 0.25% CHAPS for 1 hr at 68°C, twice before washing in maleic acid buffer (100 mM maleic acid, 50mM NaCl, pH 7.5) containing 0.1% Tween 20 for 15 min at RT. Samples were then blocked for 90 minutes in maleic acid buffer containing 0.1% Tween 20 and 2mg/mL BSA (MATB) before incubation with anti-Digoxigenin-AP Fab fragments (1:4000, Roche) for 14 hr at 4°C. Then, samples were rinsed in MATB for 20 min at RT, eight times before staining with NBT / BCIP (nitro blue tetrazolium / 5-bromo-4-chloro- 3-indolyl phosphate) in N,N-dimethylformamide overnight at 4°C. Samples were rinsed twice in PBT before blocking in PBT containing 5% NGS and 0.2% BSA for 1 hr before overnight incubation at 4°C with anti-GFP antibodies (A-11122, Invitrogen) diluted 1:500 in PBT with 5% NGS and 0.2% BSA. Samples were then washed with PBT 4 times for 30 min before incubation at 4°C for a minimum of 2 hr with fluorescent secondary antibodies (Alexa Fluor 488) diluted 1:1000 in PBT with 5%

NGS and 0.2% BSA. Samples were then rinsed in PBT for 30 min, four times before refixation for 30 min in 4% paraformaldehyde in PBS with 0.25% Triton X-100. Fixative was wash off 3 times for 5 min in PBT and samples cleared in 80% glycerol in PBS prior to mounting and imaging.

Behavioral analysis

Individual larval zebrafish were tested in 9x 9mm² well grid arena above a translucent diffuser illuminated by an XXX LED array at ~ XXX lux and responses recorded at 512 x 512 with a high-speed camera (DRS Lightning RDT/1; DEL Imaging) at 1,000 frames/s and analyzed with Flote software [107]. Acousto-vibrational startle responses, elicited as previously described, occurred bimodally as short-latency C-starts (SLC) and long-latency C-starts [107]. Stimuli were generated with a digital-to-analog card (PCI-6221; National Instruments) and delivered by an electrodynamic exciter (Type 4810 Mini-shaker; Brüel & Kjær, Norcross, GA) controlled by an digital-analog data acquisition card (PCI-6221; National Instruments, Austin, TX). Stimulus waveforms were 21 to 36 dB, of 2 ms duration, and nominally 250 or 1000 Hz, although such acousto-vibrational stimuli are intrinsically broadband. Different stimuli were pseudo-randomly presented 20 times each at 15 second intervals. For behavioral analysis of larvae following PTU treatment and laser ablation, some fish were unable to be automatically tracked and in these cases behaviors were manually assessed with the scorer blinded to the identity of ablated versus control conditions. Startle responses were

considered SLCs if they occurred within 15 ms of stimulus delivery while LLC responsiveness was calculated as the number of larvae responding with long-latency C-starts as a fraction of all larvae still stationary after the the time period of SLC responsiveness. This adjustment is made as SLC production precludes the production of LLCs.

Optogenetic activation

Larval zebrafish were injected with toll mRNA and a plasmid containing *UAS:BGi-chEF-v2a-mCherry-afp* flanked by toll recognition sites at the one cell stage. Larvae expressing mCherry and presumably ChEF in the *y293Et* pattern were selected for and raised in the dark in PTU. At 6 dpf, larval zebrafish were restrained in 3% low-melting point agarose in E3h in a petri dish. Once solidified, agarose was cut away from the tail caudal to the swim bladder to allow for free tail movement and the behavioral readout of optogenetic stimulation. Larvae were then place on a custom 3D printed stage with temperature maintained at 28 °C by a ring-shaped Peltier device.

ChEF and mCherry positive R1 neurons were imaged on a custom-built multiphoton microscope with a 20x/0.90 numerical aperture water dipping lens (Olympus #) and a Ti-Sapphire laser (Coherent Chameleon Vision-S) tuned to 950 nm for excitation that was controlled in Matlab (Mathworks) by ScanImage [108]. Captured images were converted into a binary ROI that was then projected back onto the larval zebrafish brain by a digital micromirror device (DLi4130, Digital Light Innovations) during behavioral

trials. Optogenetic stimuli were generated by Clompex (pCLAMP 10.4, Molecular Devices). To track tail movements, larvae were illuminated using an 980nm LED and imaged from below at 100 frames per second using an infrared-sensitive CCD camera (Pike F-032C IRF, Allied Vision Technologies). Tail movements were acquired and tracked using custom routines in Matlab with 2000 frames collected on each stimulus trial.

Neuron tracing

To selectively label neurons, *y293Et-Gal4;UAS:bloswitch* was crossed to *hsp70l:B3*. Compared to other reporters, *UAS:bloswitch* is stochastically expressed while the *B3* transposase is weakly active. The sparse labeling of neurons in *y293Et*, stochastic labeling of *UAS:bloswitch*, and the weak activity of *B3* allows for labeling of single neurons. Larvae were heatshocked for 25-35 min at 37°C and then imaged at 6 dpf. *lynTagRFPT*

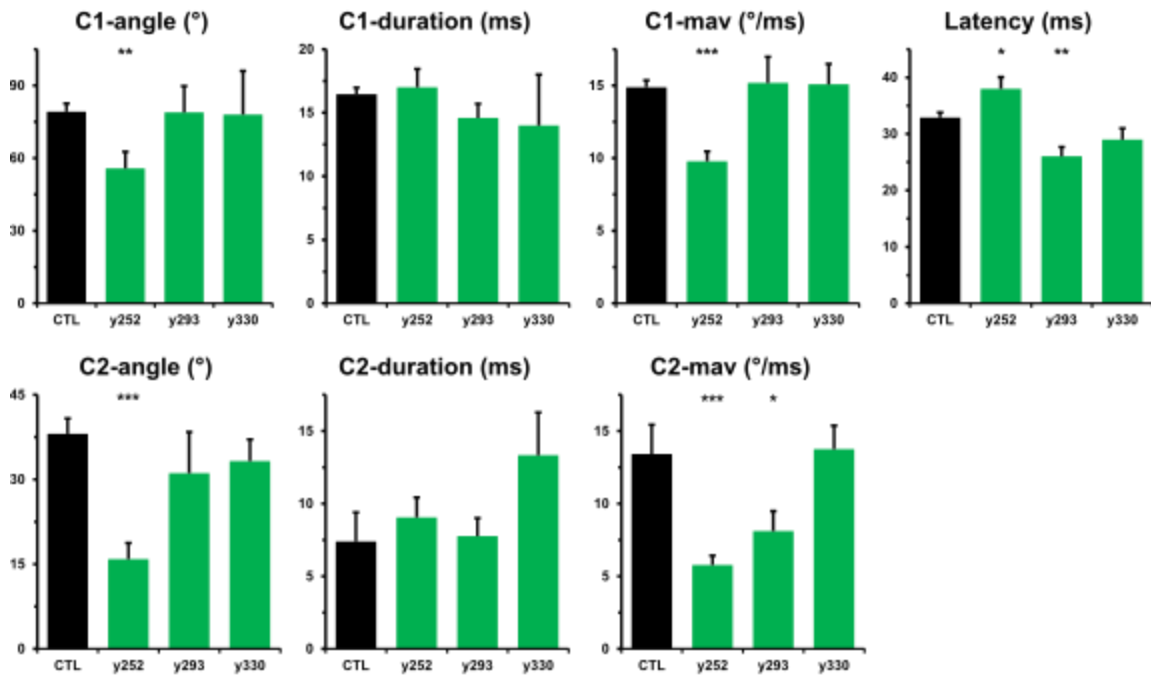
Imaris 8.4.2 was used to trace neurons that were exported as TIF files and converted to NIFTI files. NIFTI files were then affine registered with ANTs to *y293Et;lynTagRFPT* cropped average To trace neurons,

Acknowledgements

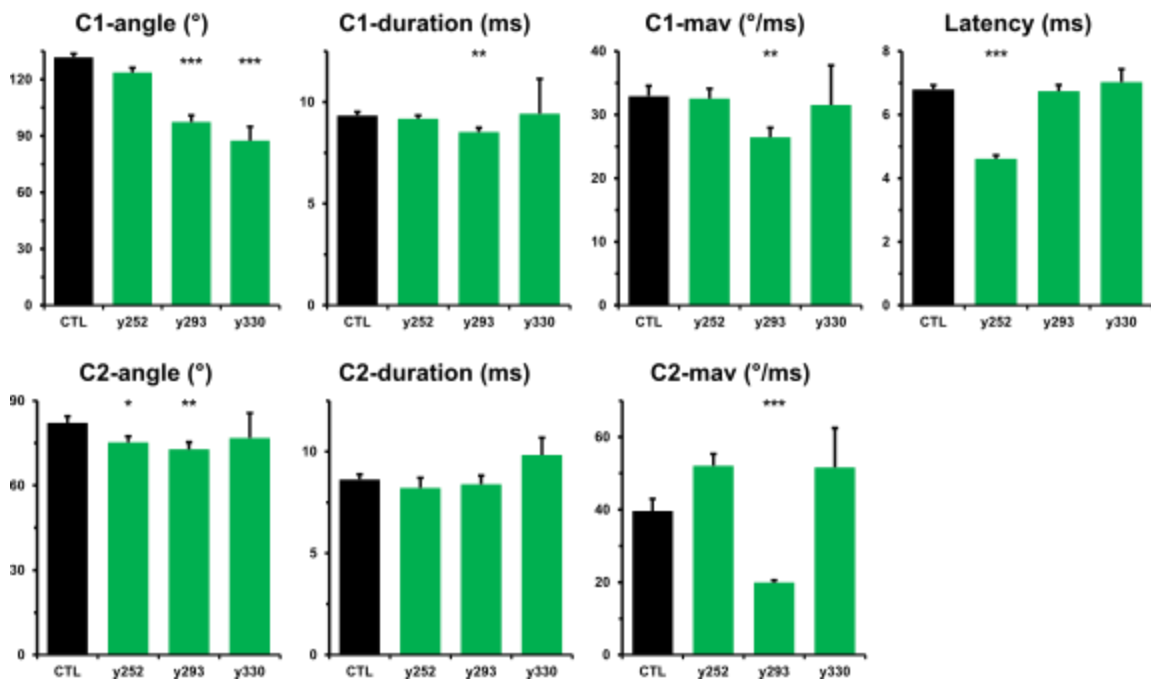
The *vachtb* plasmid used for in situ hybridization was a generous gift of Marnie Halpern.

y252Et, y293Et, y330Et genetic ablation kinematics

a LLC kinematics

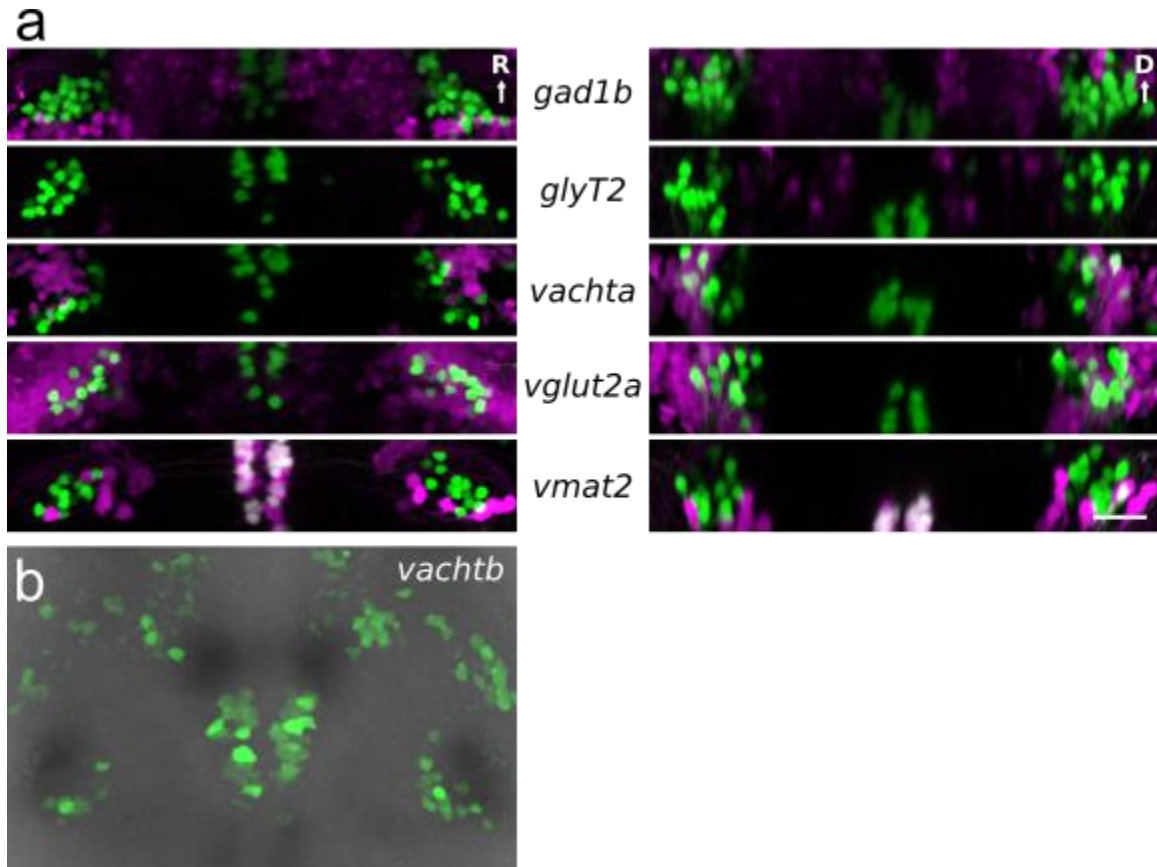


b SLC kinematics



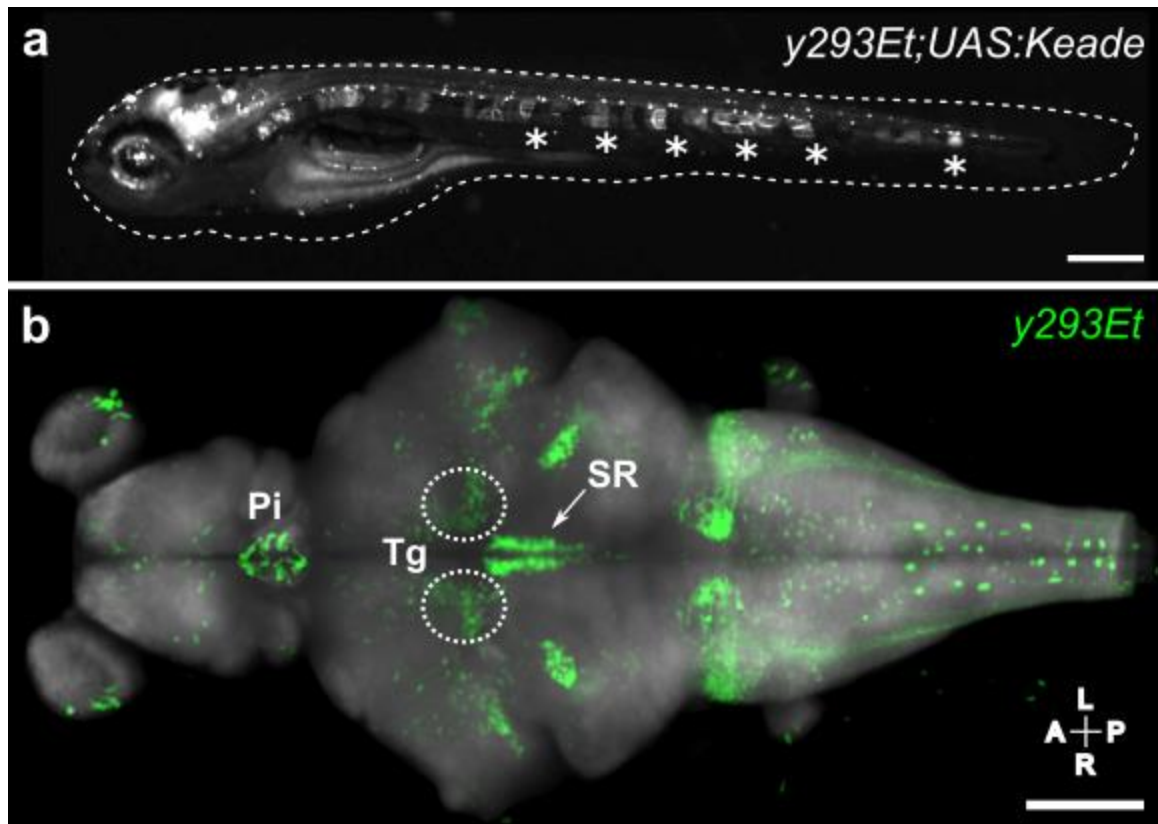
Supplemental Figure 4.1. Genetic ablation startle kinematics

(a) LLC kinematics of *y252Et*, *y293Et*, and *y330Et* genetic ablations. (b) SLC kinematics of *y252Et*, *y293Et*, and *y330Et* genetic ablations.



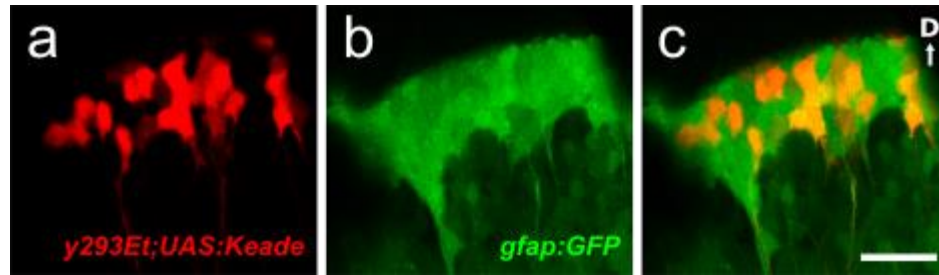
Supplemental Figure 4.2. R1 neurotransmitter identity

(a) Dorsal (*left*) and coronal (*right*) maximum projections of confocal stacks through the superior vestibular nucleus (R1) in *y293Et;UAS:Keade* larvae crossed to *gad1b*, *glyT2*, *vachta*, *vglut2a*, and *vmat2* transgenic lines (*magenta*), respectively. Scale bar = 500 μ m. (b) Anti-GFP fluorescently labeled *y293Et;UAS:GFP* larvae labeled by antisense RNA probes for *vachtb* (*dark staining*).



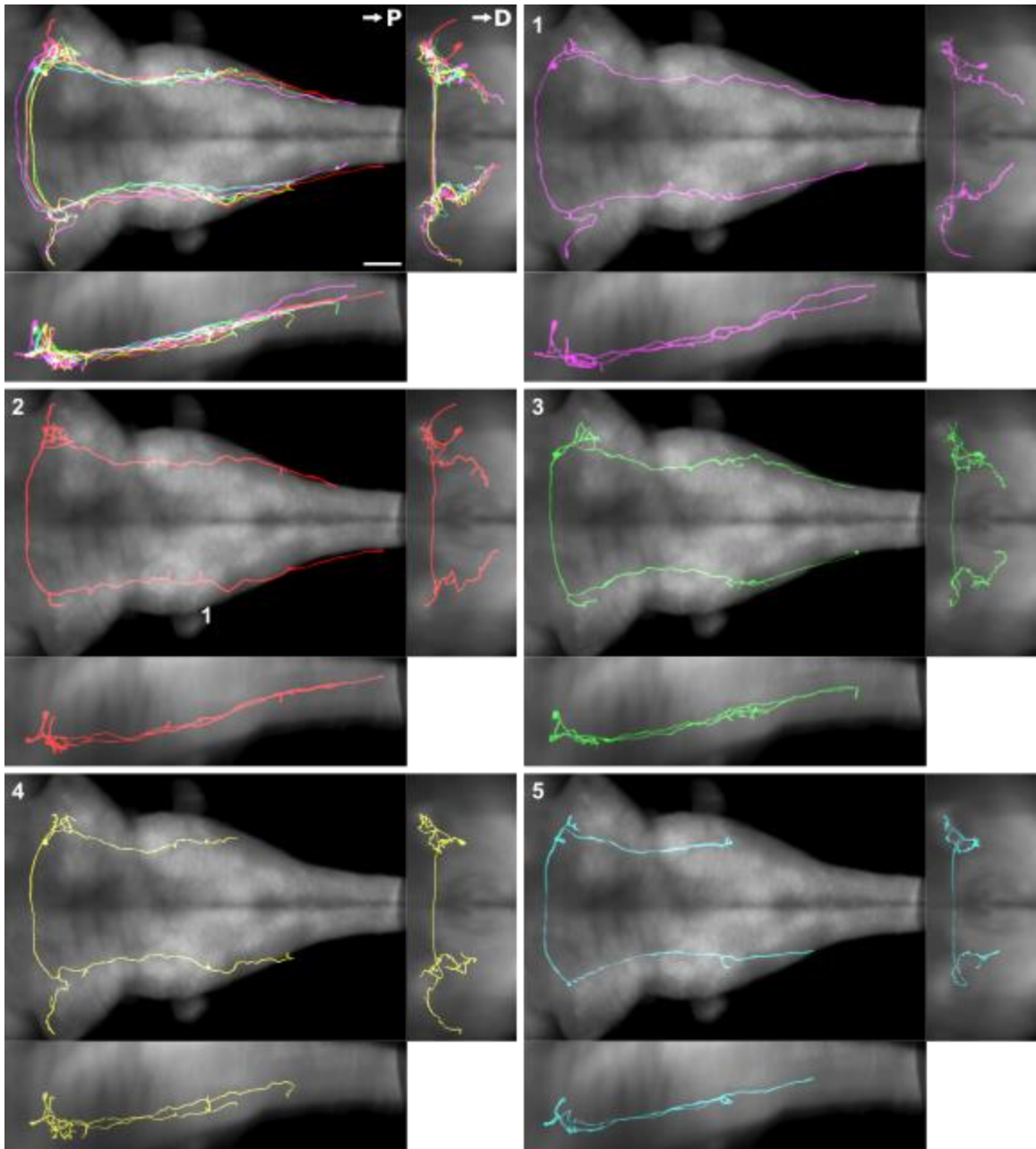
Supplemental Figure 4.3. Neural and non-neural *y293Et* expression

(a) Dissection microscope image of *y293Et;UAS:Keade* showing neural as well as non-neural expression including stochastically in the notochord (*asterisks*). Scale bar = 500 μ m. (b) Dorsal standard deviation projection of brain expression in *y293Et* shows prominent expression in the pineal gland (Pi), superior raphe (SR; arrow), and tegmentum (Tg: dashed circles). While these additional neuron populations labeled by *y293Et* could play a role in LLCs, selective genetic ablation of these regions with other lines (SR: *y228Tg*; Pi: *y227Tg*; & Tg: *y351Et*) has a negligible impact on LLCs (data not shown). Scale bar = 100 μ m.



Supplemental Figure 4.4. R2 cells in y293Et are GFAP positive

Cells in rhombomere 6 of *y293Et;UAS:Keade* are *gfap:GFP* positive suggesting that these cells are a neural progenitor population. (a) Confocal slice of photoconverted Keade driven by *y293Et* and the same slice of *gfap:GFP* expression with the overlay of both channels in (c). Scale bar = 20 μ m.



Supplemental Figure 4.5. Traces of individual R1 neurons

Dorsal, coronal, and sagittal standard deviation projections of all traced R1 neurons as well as the neurons individually. Scale bar = 100 μ m.

Supplemental Video 4.1. Optogenetic stimulation of y293Et R1 neurons

Representative optogenetic trials from three ChEF positive as a ChEF negative control larvae showing behavioral results to patterned illumination and optogenetic stimulation of R1 neurons in *y293Et*. 460nm stimulation of 10 or 100ms is indicated by a red square in the top right corner of each subframe with timestamp at the bottom right.

Chapter 5: Conclusion

Genes provide us with powerful reproducible tools to precisely, but selectively manipulate subsets of cells in the brain and for this reason, in a heterogeneous tissue like the brain, it is important to understand gene expression at a cellular level. It is often difficult, however, to characterize large numbers of genes at cellular resolution simultaneously. While transgenic lines provide tools for visualizing and manipulating gene expression, they are difficult to compare en masse and the full extent of their expression is often poorly characterized. By providing a framework to map gene expression into a common reference space, digital atlases like that constructed in Chapter 2 serve as valuable repositories of information as well as platforms for the design and interpretation of experiments. By co-imaging transgenic lines with the *vglut2a:DsRed* transgene, a broadly expressed brain marker, I was able to accurately align brains from over one hundred transgenic zebrafish lines and construct a high resolution atlas of transgene expression. By accurately aligning transgenic lines to a common reference space, we provide a solution to a common obstacle of working with Gal4 lines: finding the right line to label a specific population of neurons. Using our browser software, lines can be rapidly identified and gene expression assessed at any point within the larval zebrafish brain at near single cell resolution. This allows identification of transgenic lines that express Gal4 in almost any set of cells in the brain and provides a powerful tool for dissecting neural circuits.

Transgenic lines do not yet allow the cell-by-cell interrogation of the nervous system. Instead, most lines express in thousands of cells and frequently these cells are not exclusive to the nervous system. This broad expression is seldom discrete enough to make the kind of precise manipulations we would desire in order to implicate discrete subsets of cells for a specific role in behavior. As single transgenic lines seldom drive expression as discretely as desirable, it is consequently useful to be able to predict overlap in expression that can be exploited by genetic intersections. ZBB allows such predictions to be made. Actual cell locations may differ between individuals, however, and so while transgenic lines may appear to overlap, instead they may label closely intermingled populations. Thus, while overlap expression predictions may be useful, they need to be empirically validated.

With advances in genetics, imaging, and computational methods, we can rapidly collect brain-wide information in larval zebrafish. However, due to experimental constraints, disparate datasets may require seemingly incompatible reference brains. In larval zebrafish, multiple brain atlases have now been developed that are complementary to one another, but until now have been incompatible due to the use of different references. Although atlases would ideally use the same reference to ensure interoperability, this is not always possible. For example, Z-Brain utilized a tERK immunohistochemical stain, while ZBB utilized a *vglut2a:DsRed* transgene for reference. Both atlases contain several common expression patterns, however, that could potentially be used to bridge the databases. By using the diffeomorphic algorithm SyN in the

Advanced Normalization Tools (ANTs), we were able to overcome differences in tissue shape due to fixation, optimize the trade-off between preservation of cell morphology and global alignment, and provide precise registration in all tested brain regions. And by testing combinations of bridging channels, we found that SyN allowed for alignment of Z-Brain and ZBB with precision approaching a single cell diameter, permitting the precise combination of neural activity, neuroanatomical segmentation, and gene expression data into a single resource. This integration produces a rich platform for studying relationships between structure and function in the nervous system. While brain atlases can be used for many types of bioinformatic analysis, we predict that integrating these datasets into a single coordinate system will stimulate the development of additional computational tools and methods of analysis.

The application of SyN to our previous live scans also allowed for improved registration precision of our previous scanned lines in ZBB, which we have rereleased as an updated version of our atlas: ZBB_{1.2}. This release not only has better alignment of cell bodies, but also less distortion of neurite morphology than previous B-spline registrations. To make this dataset more accessible, we also developed a web-based browser as well as an inexpensive cell phone based virtual reality neuroanatomy explorer to better visualize brain regions in 3 dimensions. Together these tools increase the accuracy, interoperability, and accessibility of larval zebrafish brain atlases which should facilitate and accelerate neurobiological studies in larval zebrafish.

Finally, a major motivation for this dissertation was the development of tools to improve the design and analysis of circuit-breaking genetic ablation screens in larval zebrafish. And digital brain atlases like that developed in Chapter 2 provide an excellent resource for such behavioral work. By enabling the brainwide high-resolution alignment, mapping, and comparison of expression from transgenic lines, collections of lines that together drive expression throughout the entire brain can be identified and used to systematically screen neurons throughout the brain for a role in behavior. As a proof of principle to the utility of digital brain atlases in performing “circuit-breaking” genetic ablation screens, in Chapter 4 I carried out a genetic ablation screen to identify neurons responsible for long-latency C-start (LLC) behavior, a longstanding question in fish neurobiology. By comparing Gal4 expression in lines whose ablation strongly reduced LLC startle probability, I identified two regions potentially associated with LLCs. Laser ablation and optogenetic stimulation showed that neurons in one of these regions (R1) was both necessary and sufficient for LLC behavior. Unilateral R1 ablation produced a significant contralateral bias in LLCs, while unilateral activation produced an ipsilateral bias, suggesting that R1 neurons project ipsilaterally to activate downstream motor elements.

While SLC startle is the result of a single spike in a single neuron, the Mauthner cell, it is unknown what pattern of activity in R1 neurons elicits LLC responses. Similar to the Mauthner cell, is a single spike in a single R1 neuron sufficient to elicit a startle response? Or is startle behavior the result of the collective activity of some fraction of R1

neurons necessary for LLC behavior? To understand how R1 neurons encode information, we will likely need to record from them; if not electrophysiologically than through calcium imaging. Unfortunately, our current Gal4 driver lines and GCaMP reporter lines do not provide adequate expression to reliably measure R1 activity. The identification of additional lines driving expression in R1 neurons or the generation of GCaMP lines with better signal to noise ratio would overcome this current limitation and allow the exploration of these questions.

With a novel intersectional genetic approach, I was able to trace the morphology of individual R1 neurons and identify possible regions of the brain for afferent or efferent connections to R1. Based on R1 neuron morphology, I hypothesize that the ipsilateral projection in rhombomeres 1 and 2 is likely a dendritic arborization where R1 neurons receive contralateral auditory as well as potentially other sensory inputs. The three remaining projections (i.e., contralateral midbrain as well as contra- and ipsilateral hindbrain) have morphology suggestive of axons. Based the directionality of C-bends resulting from unilateral ablation or excitation, I hypothesize that R1 ipsilateral hindbrain projections excite downstream premotor elements in in rhombomeres 7 and 8. The possible function of mid- and hindbrain contralateral projections, however is less apparent. Given the likely need to inhibit incompatible contralateral behaviors, e.g., LLCs in the opposite direction, it is possible that these projections connect to inhibitory circuits responsible for reciprocal inhibition of contralateral C-starts. Until the polarity of R1 neurons is known and synaptic partners identified, however, this is speculative. Although

we have yet to identify the neurotransmitter used by R1 neurons, that optogenetic stimulation can elicits C-bends suggests a possible role for a fast-acting excitatory neurotransmitter, but this will have to be experimentally confirmed in future work.

R1 neurons were strikingly homogenous in overall morphology. Subtle differences, however, exist in the extent of their hindbrain projections. This variability in hindbrain termination suggests that different R1 neurons may synapse onto non-overlapping populations of hindbrain motor elements. Such variability in innervation could provide a simple mechanism for producing the variability seen in LLCs compared to SLC startle behavior. Whether this variability has a functional significance will need to be explored. Alternatively, this apparent variability could simply be a developmental artifact.

Recent invertebrate work suggests that stereotyped startle responses are more complex than originally appreciated and that the variability in their production thought merely stochastic is actually the result of ongoing neural calculations. In zebrafish, C-start responses that once appeared a single monolithic behavior have now been shown to be at least two distinct behaviors with only the fastest of behaviors resulting from canonical M-cell-mediated escape circuitry. With this new appreciation for the complexity of startle behavior and the identification of components for a LLC circuit, two future areas of research should be addressed. First, sensory inputs and motor outputs for the LLC circuit need to be mapped. This will provide a better understanding of the sensory pathways that drive or modulate LLC startle as well as on the motor side the

degrees of freedom in the production of LLC behavior. Second, with central components for both SLC and LLC behavior now identified, larval zebrafish should provide an opportunity to explore decision making between two circuits underlying known behavioral alternatives.

Appendix 1: Decision making and behavioral choice during predator avoidance

The work presented in this chapter has been edited for stylistic consistency and to conform with Graduate School guidelines, but has been published previously as:

Herberholz J, Marquart GD. Decision making and behavioral choice during predator avoidance. *Front Neurosci* (2012) **6**:125.

Abstract

One of the most important decisions animals have to make is how to respond to an attack from a potential predator. The response must be prompt and appropriate to ensure survival. Invertebrates have been important models in studying the underlying neurobiology of the escape response due to their accessible nervous systems and easily quantifiable behavioral output. Moreover, invertebrates provide opportunities for investigating these processes at a level of analysis not available in most other organisms. Recently, there has been a renewed focus in understanding how value-based calculations are made on the level of the nervous system, i.e., when decisions are made under conflicting circumstances, and the most desirable choice must be selected by weighing the costs and benefits for each behavioral choice. This article reviews samples from the current literature on anti-predator decision making in invertebrates, from single neurons to complex behaviors. Recent progress in understanding the mechanisms underlying value-based behavioral decisions is also discussed.

Introduction

Successful avoidance of a predatory attack is essential for survival and future reproductive success. Failure to detect a predator before an attack initiation, failure to fight off an attack, or failure to respond to an attack with an immediate escape, can be deadly. Many aspects of nervous system function must be optimized to control anti-predator behavior, including careful sensory assessment of threat stimuli, which sometimes involves multimodal integration, rapid transmission of this information within neural structures, and finally, fast and accurate motor activation. Importantly, predator avoidance is often produced under conflicting circumstances. Many daily activities that are essential for survival, such as feeding, mate search, or habitat selection, can increase visibility and thus vulnerability to predation. Animals trying to satisfy important needs while avoiding predation face a trade-off, e.g., between eating and the risk of being eaten. Thus, the selection of the most desirable behavior requires careful calculation of costs and benefits associated with different behavioral options. For example, foraging animals must accurately measure predation risk and weigh this risk against current nutritional state. Such cost-benefit analyses are made by the nervous system through the integration of external sensory signals with current internal states, and these decisions ideally lead to behavioral choices that optimize an animal's fitness.

Invertebrates are superbly suited to measure both the behavior and neural mechanisms underlying predator avoidance. In many invertebrates, an accessible nervous

system with described neural escape circuits controls discrete escape behaviors. Thus, the link between neural machinery and behavioral expression is often identifiable and quantifiable. More recently, economic decision making, i.e., costs-benefit calculations under predatory risk, has been measured and described in a number of invertebrate species. This has opened up exciting new avenues for gaining a better understanding of complex “neuroeconomic” processes at a level of analysis not feasible in vertebrates.

The first section of this review summarizes some of the foremost examples of anti-predator behavior and underlying neural circuitry found in four different arthropods. Both the specializations and shared features of these nervous systems that allow these animals to escape immediate predatory threats are discussed. The second part focuses on economic decisions made by invertebrates in situations where the risk of predation must be carefully weighed against other vitally important needs. Finally, we suggest some important future directions for the further identification of neural mechanisms underlying behavioral decisions.

Mechanisms of Predator Avoidance

While predators can provide direct cues such as visual or mechanosensory signals that alert prey to the presence of a predator, indirect cues, such as odors, also allow the assessment of a potential predatory threat. However, indirect cues are frequently more ambiguous and seldom provide information on the degree or immediacy of the danger posed. And indirect cues that signal the presence of a predator (although no predator is

currently present) can divert attention from other vital activities or suppress these activities altogether. Different risk assessment behaviors, apprehension, and vigilance, are responses to indirect predator cues commonly described in vertebrate animals [109]. Although they are likely to exist in invertebrates, these “anticipatory” predator avoidance behaviors are much less studied in invertebrates where the evolution of extremely fast and powerful escape reactions in response to immediate attack has arguably reduced the necessity for extensive predator scanning and risk assessment. Additionally, while numerous behaviors in an animal’s repertoire contribute to predator avoidance, most are subtle and difficult to subject to neurobiological analysis. For instance, an animal’s decision when and where to forage is greatly shaped by the risk of predation [110]. How an animal calculates this predatory risk and weighs it against concurrent internal and external demands is certainly an interesting question; however, the time-scale and context of such a decision make it difficult to subject to detailed electrophysiological or neuroanatomical analysis. Instead, what has overwhelmingly sufficed for the study of predator avoidance in neuroscience has been the analysis of much more discrete escape or startle behaviors. Because escape behaviors are so critical, they must interface with and frequently override the performance of any ongoing or planned behaviors. And while other behaviors may have a greater evolutionary importance over the long term, seldom are they as time-sensitive and unforgiving as escape. Thus, it is unsurprising that the circuits tasked with the sensory acquisition, computation, and action upon salient

predatory cues are frequently the largest, most robust, and most highly stereotyped neural systems in an organism.

If a predator is around, it is critical to identify and react to predatory cues at an appropriate time and in an effective manner. Consequently, escape behaviors must be fast, accurate, and robust in order to be effective countermeasures against the often rapid predatory behaviors they combat. It is believed that the time-sensitive nature of these behaviors necessitates a small number of large elements in order to both maximize conduction velocity and minimize synaptic delay. Thus, escape circuits commonly have “giant fibers (GFs),” frequently the largest axons in an animal’s nerve cord, which can be readily identified by their size, location, or morphology. These characteristics allow for rapid identification and often make these neurons accessible to a wide range of cell biological and electrophysiological studies.

Because of their simplicity and clear function, these circuits have been excellent models for the study of the neural basis of behavior. Recent work, however, has uncovered a surprising degree of flexibility not previously recognized in these “simple,” “reflexive” systems. High-speed video recordings have exposed a previously unappreciated level of complexity to arthropod escape behaviors that has made researchers question the structure and even identity of the underlying circuits that were originally assumed to be responsible for escape [111–115]. Additionally, wireless-recording techniques have been adapted to small invertebrate models allowing, for the first time, the correlation of neural activity from multiple identified neurons with the

time-course of escape behavior in unrestrained preparations [116,117]. And while neural-behavioral correlations are not uncommon, escape behavior in invertebrates provides possibly one of the few opportunities to simultaneously record from all the critical elements in a neural circuit and relate it to what is now appreciated as an increasingly complex, but still tractable, behavior. This provides quite possibly one of the best current opportunities for the comprehensive analysis of the neural underpinnings of decision making surrounding a behavior.

While there is likely a broad spectrum of complexity in the circuits embedded in even the most simple nervous system, escape circuits in invertebrates are frequently divided into two broad categories: those that contain “command” or “command-like” elements and those that do not [118–121]. In command systems, the activity of the command neuron is thought to be necessary and sufficient for the production of a behavior. Often a single spike in this neuron is sufficient for the readout of an entire escape program. While highly adaptive, these rapid behaviors are highly stereotyped, showing little variability. In contrast, the escape behaviors produced by systems ostensibly lacking a command element typically display a greater degree of complexity and flexibility and are frequently made up of a sequence of independently variable components. This flexibility affords the animal a greater degree of control over the precise timing, direction, and structure of the escape behavior. Traditionally, however, this is assumed to come at an additional computational cost that adds to the latency of the action [122]. Alternatively, variability may be added to behavioral decisions by

sequential neural processing. For example, in the medicinal leech decision neurons can be active during competing behaviors (e.g., swimming and body shortening), and stimulation of one decision neuron can produce two different behavioral outputs, swimming and crawling. Hypothesized to be organized in a hierarchical order, the first neuron in the chain would drive general behavioral action, the next one would command selection from a pool of discrete motor patterns, and the next one would initiate the most desirable behavioral choice [123].

Giant-Neuron Mediated Escape

Crayfish

Crayfish are equipped with powerful escape reactions mediated by rapidly responding neural circuits (reviewed in [120,124,125]). These circuits control at least three distinct motor programs that propel the animals in different directions, but always away from real or assumed threats. Circuits and their associated tail-flips can be divided into two major categories, giant and non-giant. Two circuits, the lateral giant (LG) and medial giant (MG) system contain giant interneurons as key “command” components, are made for speed, and require strong and phasic input for their activation. In contrast, a poorly elucidated non-giant system is believed to control slower, but more variable escape tail-flips [120]. These escape circuits have been the focus of 65 years of intensive research since they were first described by Wiersma [126,127] in his pioneering work.

The LG interneurons, two large fibers consisting of a series of gap junction-linked neurons that project from tail to head, are activated by tactile and strong hydrodynamic stimulation of sensory hairs and proprioceptors located on the abdomen. The LG interneurons also receive excitatory inputs from rostral sensory organs, but these inputs alone are insufficient to fire the LG. If these inputs sum with strong caudal inputs, however, a single LG action potential (in one of the two fibers) is sufficient to produce an escape motion that thrusts the animal upward and away from the point of caudal stimulation [128]. The motor program is activated within milliseconds after stimulation and speed and accuracy is guaranteed through several structural and functional specializations within the circuit [129]. Once activated, the LG interneurons drive giant motor neurons via rectifying electrical synapses, which activate fast flexor muscles in the last two thoracic and first three abdominal segments causing a bending of the abdomen around the thoracic-abdominal joint and thus the stereotyped “jack-knife” motion that propels the animal upward [130]. Latency is minimal, with 5–15 ms between stimulation and start of the behavioral response, and varies according to both internal (e.g., animal size: [131]) and external conditions (e.g., water temperature: [132]). This short latency is accomplished by the high transmission velocity due to the diameter of the GFs and by electrical coupling among most circuit components (*Fig. A1.5A*).

The MG interneurons, a pair of large fibers projecting from head to tail, are activated by strong, phasic visual or tactile inputs directed to the front of the animal. The MG interneurons receive their excitatory inputs in the brain where both neurons are

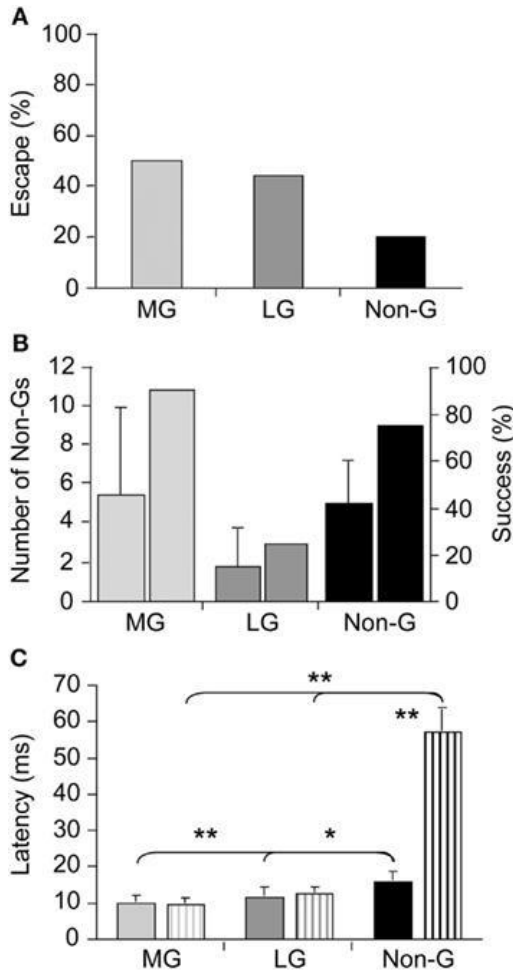
electrically coupled to each other. One action potential in one of the MGs is sufficient to drive the fast and stereotyped backward escape response. The MG interneurons connect electrically to giant motor neurons, which activate fast flexor muscles in all abdominal segments, causing the bending of the entire abdomen and propelling the animal backward away from the point of stimulation. MG tail-flips in response to tactile stimulation are as fast as LG-mediated tail-flips and happen within a few milliseconds [130]. Visually activated MG tail-flips are slower, but are still produced as quickly as 50 ms after detection of a visual danger stimulus [133,134].

Non-giant-mediated tail-flips are controlled by a circuit that lacks giant interneurons. These tail-flips are elicited by a variety of different stimuli, typically more gradual and less forceful in presentation than those activating giant-mediated tail-flips. They are produced with longer latencies, usually up to 10-fold slower than giant-mediated tail-flips, and considered, in a way, “voluntary” because the animal “chooses” to activate certain patterns of fast flexor muscle groups. Thus, the timing and direction of non-giant tail-flips can be modulated, resulting in a much more variable behavior compared to the giant-mediated tail-flips [124,135]. Non-giant tail-flips are also used during “swimming,” where a series of tail flexions and extensions propels the animal backward through the water.

Although our understanding of the neural underpinnings of tail-flip escape, especially tail-flips produced by the LG circuit, is extensive and essentially unmatched by that of other experimental models, our knowledge of escape circuit activation in response

to real predatory danger is virtually non-existent. Using dragonfly nymphs as natural predators, Herberholz et al. [136] showed that all three escape circuits of juvenile crayfish were activated in response to attacks (*Fig. A1.1A*). Initial escape responses to predatory strikes were primarily mediated by giant tail-flips; frontal attacks evoked MG tail-flips whereas attacks directed to the rear of the crayfish elicited LG tail-flips. While few attacks elicited non-giant tail-flips initially, overall escape performance improved substantially when non-giant tail-flips were produced following capture. Overall, crayfish were successful at evading dragonfly nymphs, avoiding the predator's strike with giant tail-flips in 50% of all cases and escaping, after being captured, using a series of non-giant tail-flips in more than 75% of the remaining cases (*Fig. A1.1B*). Interestingly, latencies for non-giant tail-flips that were produced as initial response to the predator strike were much shorter than latencies of non-giant tail-flips elicited by tactile stimulation with a handheld probe (*Fig. A1.1C*). This suggests that crayfish prepared the non-giant escape before the strike was delivered, possibly integrating visual and hydrodynamic cues from the approaching predator in anticipation of the attack. The study also revealed that crayfish relied entirely on their fast and powerful tail-flip escape behaviors; crayfish showed no signs of predator recognition, vigilance, or avoidance behaviors in any of the trials [136]. Thus, the decision to escape, at least from this specific predator, is based on the activation of fixed action patterns elicited by predatory stimuli. The decision to escape is made at individual decision-making neurons; if the predatory signal is sufficient to activate them, escape will inevitably follow.

Figure A1.1. Escape success and latencies measured in juvenile crayfish attacked by dragonfly nymphs.



(A) Attacks evoking tail-flips mediated by the medial giant (MG) or lateral giant (LG) interneurons are equally effective to prevent capture whereas attacks eliciting non-giant (Non-G) tail-flips are much less effective. (B) Unsuccessful MG and Non-G, but not LG responses are frequently followed by a series of Non-G tail-flips (left bars), which substantially increase the overall rate of escape (right bars). (C) Escape latencies for crayfish attacked by predators (solid bars) or stimulated with a handheld probe (striped bars) are similar for giant mediated (MG and LG) tail-flips, but significantly shorter for predator evoked Non-G tail-flips. Modified from Herberholz et al. [136].

Drosophila

There are a number of similarities between the GF system in *Drosophila* and the MG system in crayfish. Like the MG system, the GF system contains GFs originating in the brain that project down contralaterally to primary motor neurons that control the thoracic musculature responsible for the fruit fly's escape behaviors (reviewed in [137,138]). In these giant fibers, a single spike is normally sufficient for the activation of

an escape jump followed by flight initiation. Despite the motor portion of both the MG and GF being well described, comparatively little is known about the visual and mechanosensory pathways that feed into the giant fiber systems of either animal (*Fig. AI.5A,B*).

While the escape behaviors produced by these circuits are extremely fast due to high conductance velocities and the minimal synaptic delay from a preponderance of electrical synapses, this speed has generally been thought to come at the expense of flexibility [122]. Thus, giant-mediated escape behaviors are traditionally characterized as highly stereotyped with little variance in timing or direction; and whatever variance the result of stochastic properties of the system and not the consequence of neural computation [122].

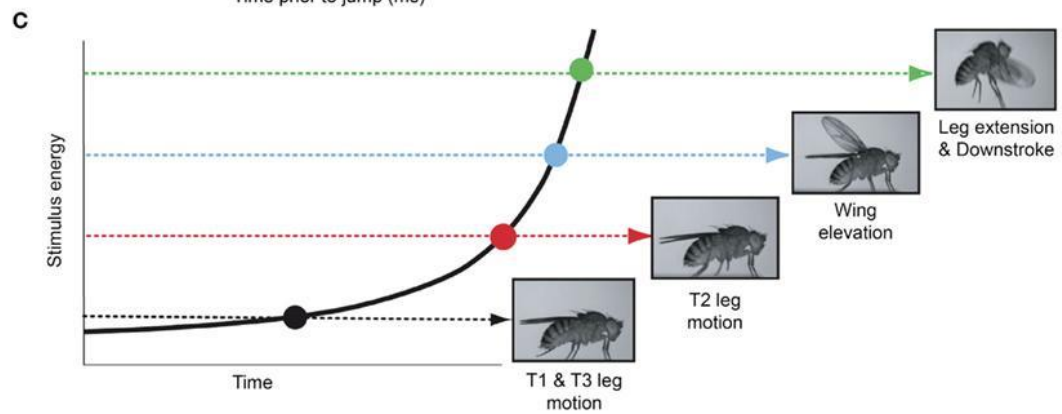
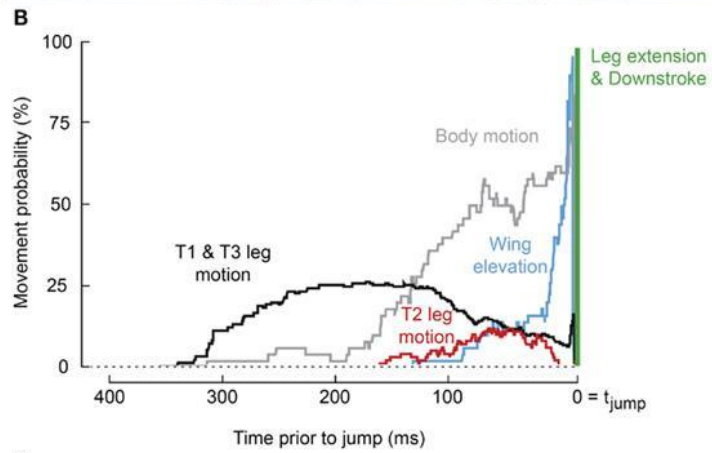
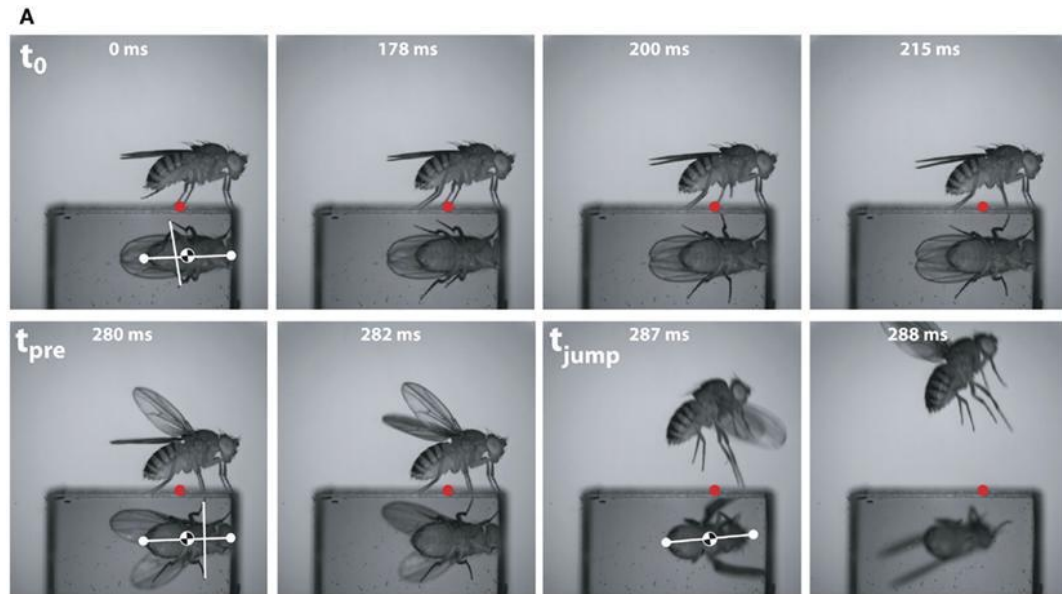
Although *Drosophila* has been a preeminent genetic model since the start of the twentieth century, its diminutive size limited its use in electrophysiology until the 1970s [139]. And while the GF system was identified in 1948 [140], it was not electrophysiologically characterized and linked to the production of escape behavior until the early 1980s [137]. This escape behavior was initially characterized as an abbreviated form of “voluntary” flight initiation [141]. While voluntary flight initiation is preceded by a series of postural adjustments that prepare the fly for stable, directional flight, escape flight lacks these preflight postural leg, and wing movements. Instead, escape initiation consists almost exclusively in the extension of the fruit fly’s mesothoracic legs that

propels the insect off of the substrate, which is only then followed by the unfolding and initiation of wing movements [113].

As the GF system was the only identified *Drosophila* escape circuit, it was assumed to mediate the escape behavior elicited by all visual, chemical, and mechanosensory stimuli that elicit an escape jump [142]. However, a number of observations have accumulated that conflicted with this canonical interpretation. For instance, in the housefly GF activity was shown not to be necessary for the production of an escape jump in response to looming stimuli [143]. Additionally, Trimarchi and Schneiderman [144] provided evidence for an olfactory-induced flight initiation reminiscent of the fruit flies' escape behavior that was also not mediated by the GFs. More recently, the simplicity of the observed escape behavior was reassessed through high-speed video analysis [111–114]. This work illustrated that these “simple” escape behaviors were far more complex and nuanced than originally assumed (*Fig. AI.2A,B*). Card and Dickinson [113] showed that rather than a simple escape jump, the escape behavior in wild-type fruit flies involves a complex sequence of events consisting of at least four distinct subcomponents: an initial freeze followed by postural adjustments, wing-elevation, and finally an escape jump coordinated with the initial down stroke of flight initiation (*Fig. AI.2C*). These behaviors do not appear to merely be a fixed action pattern as new information continues to be integrated into and affect subsequent components of the behaviors even after sequence initiation [112]. These preflight

behaviors were found to influence both the trajectory as well as initial flight stability of the escape behavior [114].

Figure A1.2. Escape flight planning and execution in *Drosophila*.



(A) High-speed video sequence shows a typical escape to a looming frontal stimulus with a prism allowing for simultaneous observation of ventral and side profiles. Time stamps are milliseconds elapsed since stimulus onset. Red dots mark the initial contact point of the second leg tarsi with substrate. White dots mark head and abdomen points. (B) Probability that body parts of the fly (black, T1 and T3 legs; red, T2 legs; blue, wings; gray, body) were moving prior to takeoff (green line). (C) As stimulus intensity increases, independent motor programs are activated eliciting discrete escape subbehaviors prior to takeoff. Adapted with permission from Card and Dickinson [114].

This newly appreciated complexity of the response suggests that this escape behavior is either not in fact mediated by the GF system or that additional unidentified pathways must be involved that are responsible for the preflight sequence that precedes the escape jump [114]. Toward this end, evidence for a previously unknown escape circuit was recorded by Fotowat et al. [115]. In the absence of GF activation, the activity of this novel circuit correlated with the production of escape behavior in response to looming stimuli. While this pathway is yet to be anatomically identified, its activity shares features similar to well-described circuits responsive to looming stimuli in both vertebrates and invertebrates (e.g., pigeon: [145,146]; crab: [147]; bullfrog: [148]). All of this strongly suggests that the GF system is not necessary for the production of escape behavior in the fruit fly, but that the GF system, possibly akin to the escape circuits in the crayfish, may be one of many present in *Drosophila*.

Being that sudden changes in luminance (light-off) are the only stimulus to reliably produce GF-mediated escape behavior, and then only in white-eyed fruit fly mutants, what role, if any, that the GF system plays in actual escape behavior of wild-type fruit flies is now unclear. Although stimuli that reliably recruit the GF system in

wild-type flies are unknown, it seems unlikely that the GF system is simply the vestige of a lost escape circuit. While the newly identified looming sensitive pathway might be tuned to a selective set of stimulus features, the GF system could still serve as a robust, broadly tuned escape circuit capable of producing rapid escape behavior when more selective systems fail [115].

Visual Interneuron Mediated Escape

Locust

While locusts produce avoidance behavior in response to a variety of noxious stimuli [149,150], the best studied of these are escape jumps in response to looming stimuli (reviewed in [151,152]; **Fig. A1.3**). Like the escape behavior of fruit flies, the locust escape jump is a complex behavior composed of a sequence of distinct components, which allow the animal to direct this jump [153]. In preparation for a jump, tilting postural movements mediated by the pro- and mesothoracic legs rotate the long axis of the locust toward the direction of the eventual jump ([153,154]; **Fig. A1.3A**). The actual jump is produced through the cocking of the hindlegs, storage of energy by the co-contraction of tibia flexor and extensor muscles, and finally the release of this energy, triggered by flexor inhibition [155]. Given the time required to store sufficient energy in the animal's hindlegs, co-contraction must begin as soon as possible in order to allow for a timely escape. In contrast, the adjustment of pro- and mesothoracic limbs can continue throughout co-contraction, allowing for alterations of escape trajectory up until the

escape jump is triggered [153]. On the other hand, if the hindlegs were used to control direction, it is thought that the decision of where to jump would have to be made over 100 ms before the jump is produced.

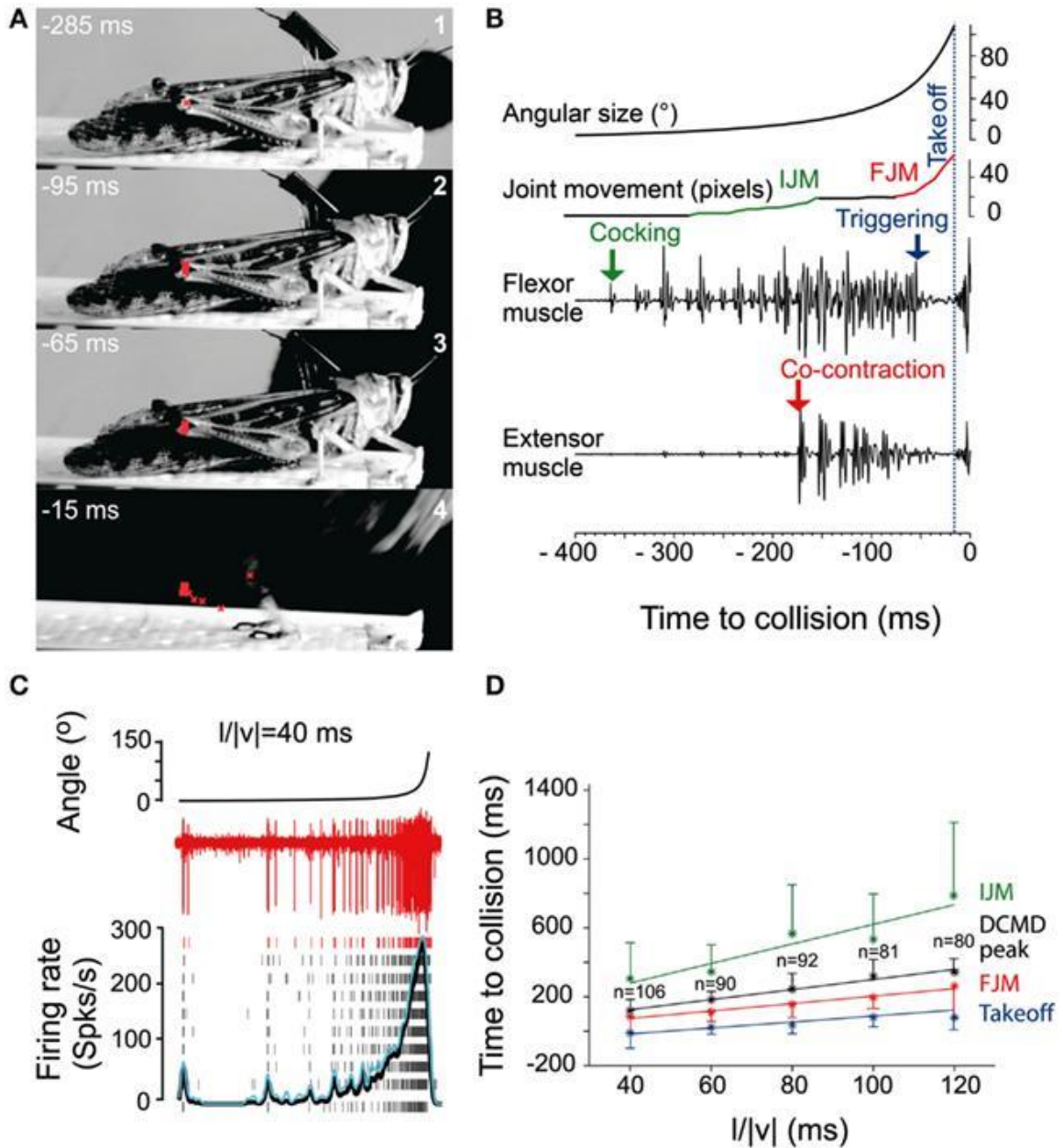
Not only are locusts able to direct these jumps up to 50° to either side of their long axis, but their escape circuitry allows them to control the timing, distance, and elevation of these jumps [153,156]. Similar to *Drosophila*, this complex sequence of events does not appear to be a fixed action pattern that once initiated must be taken to completion as the locust can relax this co-contraction and release the stored up energy without the production of an escape jump [157].

Motor areas controlling these escape jumps are innervated by a pair of large interneurons, the descending contralateral movement detectors (DCMDs) which receive excitatory inputs from lobula giant movement detector (LGMD) neurons that are responsive to looming stimuli. With a one-to-one relationship with the LGMDs, the DCMDs produce action potentials in response to looming stimuli, with their firing rate increasing as the looming object gets closer. Thus, the DCMDs were originally thought to play a major role in jump production, sometimes compared to the giant fibers in crayfish and fruit flies that control their fast escape maneuvers [152]. However, locusts prepare for jumps by co-contracting flexor and extensor tibiae muscles for ~100 ms before the jump is released by relaxation of the flexor muscles. Thus, the jump is not simply triggered by suprathreshold excitation of the DCMDs, because withdrawal of excitation and inhibition are needed during the preparatory phase of the jump (*Fig. A1.3B*).

Nevertheless, the DCMDs seem to participate in all phases of the jump. Fotowat and Gabbiani [158] compared electrophysiological recordings with high-speed video recordings and found that the rising phase of the firing rate of the DCMDs coincided with the preparatory phase of the jump, whereas the peak firing rate coincided with the co-activation period of flexor and extensor muscles, and decay of firing rate to less than 10% coincided with takeoff. This suggests that different stages of jump production could be controlled by distinct phases in the firing pattern of the DCMDs (*Fig. A1.3C,D*). Hindleg flexion in preparation for the jump, however, is not dependent on DCMD activity. When the connective containing the DCMD neuron was severed, hindleg flexion still occurred, and it could also be evoked with visual stimuli that did not cause high firing activity in the DCMDs. This showed that while the activity of the DCMDs may contribute to hindleg flexion, it was not necessary for it and, thus, other descending pathways would seem to be involved [159]. Using a telemetry system to record DCMD and motor neuron activity in freely behaving locusts, it was found that the number of recorded DCMD spikes predicted motor neuron activity and jump occurrence, and the time of peak firing rate predicted time of takeoff [116]. Although this underlined the role of the DCMDs as neurons exhibiting discrete firing responses to looming stimuli, which in turn affected discrete stages of escape motor output, jump production remained intact, and occurred at the same time as in control animals following DCMD ablation. Thus, another neuron for jump production must exist, and this may be the descending ipsilateral movement detector neuron (DIMD), which responds to looming targets, similarly to the DCMD

[116]. Additionally, another descending interneuron that responds to looming stimuli has recently been described. Thus visually mediated escape behavior in locusts is likely controlled by at least three different descending neurons [160]. How these neurons interact to produce the escape behavior remains to be determined (*Fig. A1.5C*).

Figure A1.3. Escape jump and DCMD activity in locusts in response to looming stimuli.



(A) Four high-speed video frames from a locust producing an escape jump with time to collision listed in milliseconds. The position of the femur-tibia joint is marked in red to calculate pixel movements of the joint. **(B)** Muscle recordings from the same trial.

Stimulus angular size is shown on top with joint movements and flexor and extensor recordings below. (IJM, initial joint movement; FJM, final joint movement.) (C) DCMD activity measured extracellularly in the nerve cord from one locust (red traces). Raster plots show DCMD spikes recorded in 10 repetitions of the stimulus. Black and blue traces show average DCMD firing rate and its standard deviation, respectively. (D) Timing of joint movements, DCMD peak and takeoff obtained from seven locusts. The DCMD peak occurred after the IJM and before the FJM and takeoff for all $l/|v|$ values ($l/|v|$ = ratio of stimulus radius (l) to the velocity (v) of the stimulus). Adapted with permission from Fotowat and Gabbiani [158].

Locusts also produce an avoidance behavior during flight. When looming stimuli are presented, flying locusts produce a gliding dive similar to the dives used by other insects to evade aerial predators. After DCMD neurons are activated by a looming stimulus, they produce short-latency excitatory postsynaptic potentials (EPSPs) in a motor neuron that raises the wing into the gliding posture. Stimuli that evoked high-frequency firing in the DCMDs also reliably elicited the gliding response, and the behavior was less frequently observed when high-frequency DCMD spikes were absent [161]. However, similar to the escape jump, DCMD activity was not always sufficient to evoke gliding. Most likely, its high-frequency activity must be precisely timed with wingbeat phase because glides can only be produced during wing elevation. In addition, other neurons that are implicated in jump production (e.g., the DIMDs) may also be involved in escape gliding in flying locusts [162].

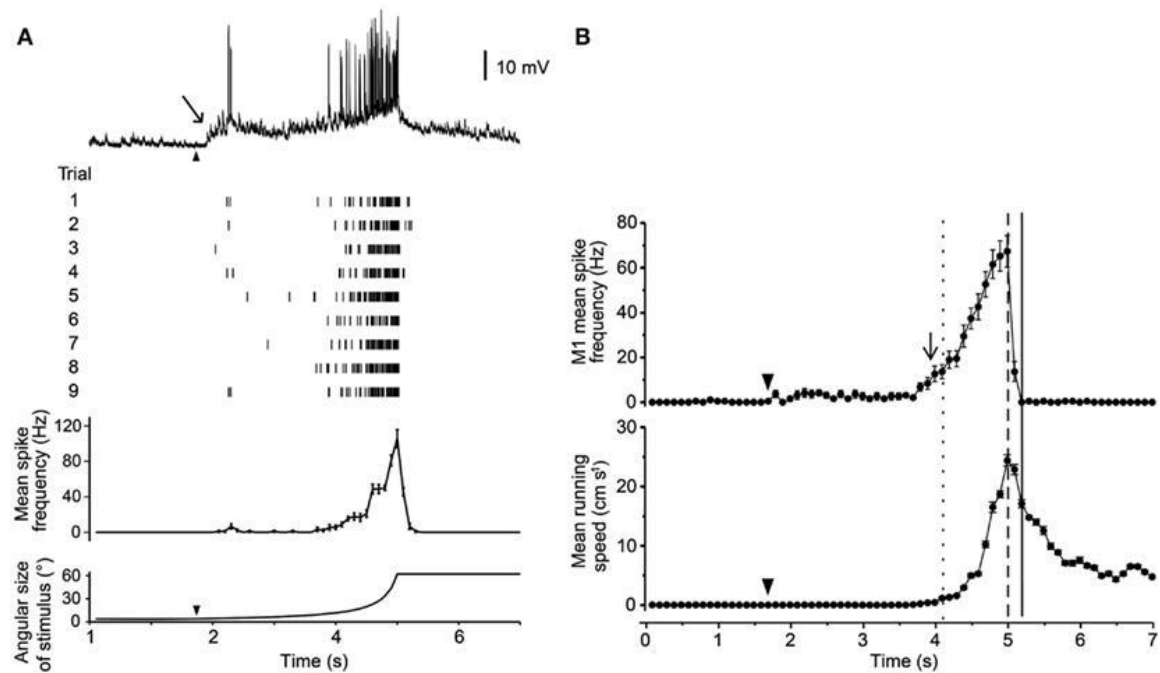
Crabs

The role of identified neurons in visually mediated escape behavior has also recently been studied in grapsid crabs (reviewed in [163]). The firing rate of these motion-sensitive lobula giant (LG) neurons in response to looming stimuli corresponds

with the intensity of the crab's escape behavior. Four distinct classes of these neurons have been anatomically and physiologically described. All four classes show wide-field tangential arborization in the lobula, somata located beneath, and axons that project toward the midbrain; however, they are uniquely identifiable due to differences in morphology and response preferences [164].

Three of these LG classes receive proprioceptive inputs from the legs, and thus could potentially integrate some contextual information during predator escape [165]. Oliva et al. [147] tested the escape behavior of grapsid crabs on a freely rotating styrofoam ball and recorded escape movements (i.e., running) while looming stimuli were presented. They also recorded intracellularly from the LG neurons in restrained crabs and compared these recordings with the behavioral data. Escape runs were initiated soon after the LG neuron increased its firing rate, and after maximum stimulus expansion, the LG neurons stopped firing, coinciding with run deceleration in freely behaving animals. Moreover, the spike frequency of the LG neurons reflected the timing and speed of the escape response (*Fig. A1.4A,B*). Interestingly, the activity of the LG neurons is strongly affected by season with responses weaker in winter when predation risk is typically low and the animals are less active [166].

Figure A1.4. Response of a crab's LG neuron to looming stimuli and correlation with escape run.

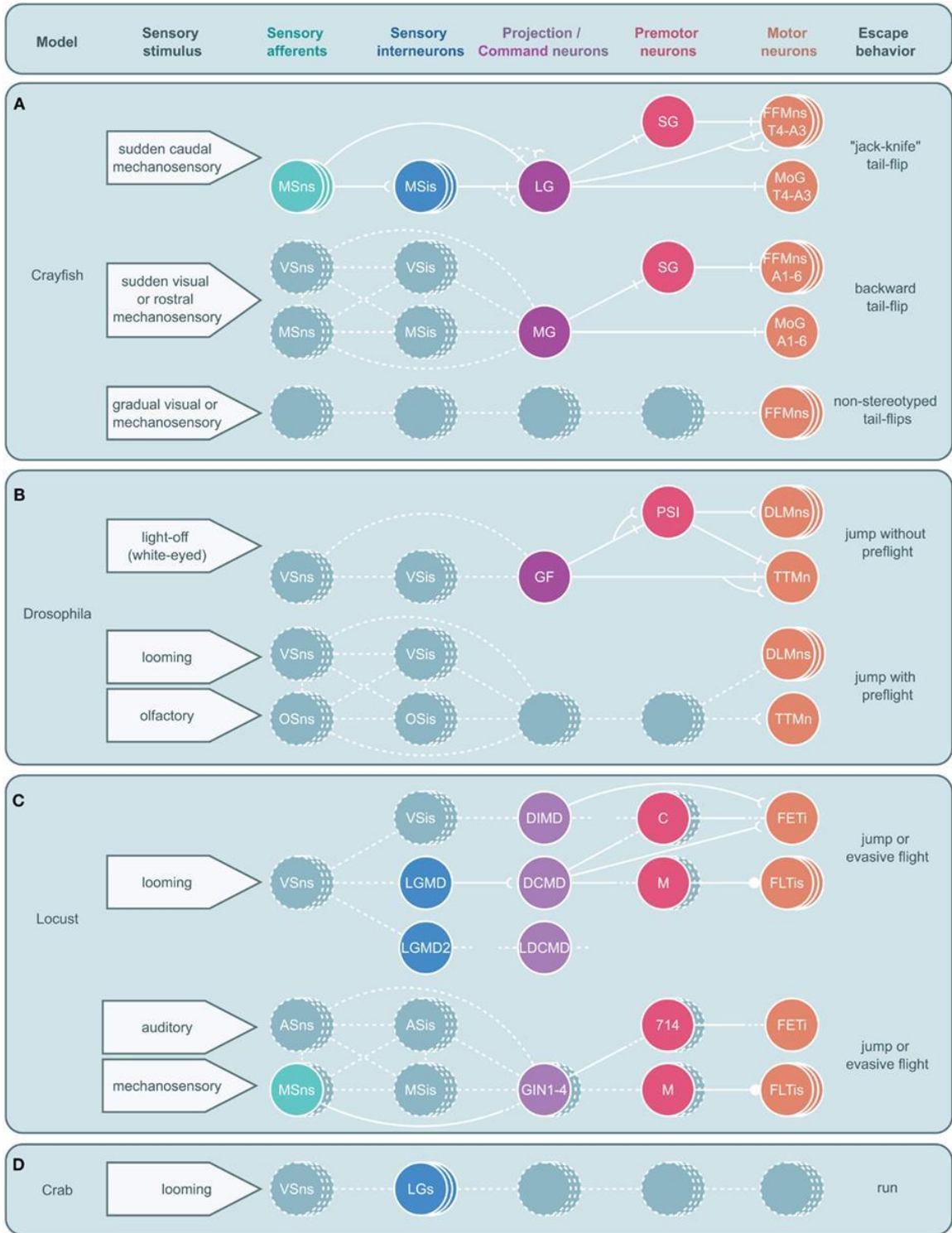


(A) Intracellular trace from one LG neuron in response to a looming stimulus. Raster plot shows responses from one neuron to nine repetitions of the stimulus. Histogram shows mean spike rate obtained from all nine trials. Angular size of the looming object is shown in bottom trace. (B) Mean spike rate from a single LG neuron (top) and mean escape running speed (bottom). Arrowheads mark the start of stimulus expansion and long arrows mark increase in spike rate above resting level. Adapted with permission from Oliva et al. [147].

The relation between LG neuron activity and escape behavior was also nicely demonstrated in experiments that tested short-term and long-term visual memory in crabs. Tomsic et al. [167] showed that LG neurons changed their responses to a visual threat (displacement of a black screen above the animal) in correspondence with the behavioral changes observed in unrestrained animals. Modification of LG neuron activity occurred during learning and persisted, after spaced training, for 24 h. However, while

the memory of freely behaving crabs reflects a strong stimulus-context association, LG neurons generalize the learned stimulus into new spatial locations. Thus, despite being able to clearly distinguish the learned stimulus from other similar stimuli (i.e., stimulus memory), the LG neurons do not appear to be involved in processing contextual visual information (i.e., where the stimulus was learned; [168]). In summary, the LG neurons are sensory neurons located in the eyestalk, and their neural activity patterns closely match escape behavior produced in unrestrained crabs [164]. Their exact role in producing the behavior, however, is unknown. To answer this question, detailed investigation of the descending pathways that connect the LG neurons to the motor centers that control escape runs will be required (*Fig. A1.5D*).

Figure A1.5. Circuitry for arthropod escape behavior.



Neural circuits underlying escape behaviors for crayfish (**A**), *Drosophila* (**B**), locust (**C**), and crab (**D**) are illustrated. Circuits are divided into five levels: sensory neurons, sensory interneurons, projection (ascending or descending) or command neurons, premotor neurons, and motor neurons with associated sensory stimuli on the left and motor output on the right. Solid circles and lines represent identified neurons and connections while dashed circles and lines represent neurons and connections yet to be identified. Stacked circles represent a population of neurons. Lines end in four ways: with a perpendicular line, a concave cup, a circle, or dashes. Perpendicular lines represent electrical synapses. Concave cups represent electrical synapses. Circles represent inhibitory synapses. Dashes indicate an unknown synapse type. Generic abbreviations: MSNs, mechanosensory neurons; MSIs, mechanosensory interneurons; VSns, visual sensory neurons; VSIs, visual sensory interneurons; OSns, olfactory sensory neurons; OSIs, olfactory sensory neurons; ASns, auditory sensory neurons; ASIs, auditory sensory interneurons. (**A**) Crayfish tail-flips are controlled by one of three circuits, the lateral giant (LG), medial giant (MG), and non-giant escape circuit. While the LG system is almost fully elucidated and the abdominal motor outputs of the MG are also well described, very little beyond the fast flexor motor neurons (FFMns) are known to play a part in non-giant tail-flips. SG, segmental giant neuron, MoG, motor giant neuron. (**B**) *Drosophila* escape jumps are the result of at least two circuits; a giant fiber (GF) system mediating jumps lacking preparatory leg and wing movements and a yet to be identified escape circuit that produces escape jumps with preparatory preflight limb and wing adjustments. (PSI, peripherally synapsing interneuron, DLMns, dorsal lateral motor neurons, TTMn, tergotrochanteral muscle neuron.) (**C**) Locusts possess at least two escape circuits as well, one responsive to looming stimuli and another responsive to auditory and mechanosensory stimuli. While numerous neurons that are believed to play a role in these behaviors have been identified, both circuits remain incomplete. [LGMD, lobula giant movement detector neuron; LGMD2, lobula giant movement detector neuron 2, DCMD, descending contralateral movement detector neuron; DIMD, descending ipsilateral movement detector neuron; LDCMD, late descending contralateral movement detector neuron, C, C (“cocking”) neuron, M, M-neuron, FETi, fast extensor tibia motor neuron, FLTis, flexor tibia motor neurons, 714, neuron 714.] (**D**) In crabs, a class of visual interneurons, the lobula giants (LGs), have been identified that are thought to play a role in the crab’s escape behavior; however, no other elements in this escape circuit have been elucidated.

Value-Based Decision Making

Adaptive behavioral decisions are essential for the survival and reproductive success of most animals, including humans. Animals can typically choose from several

behavioral alternatives, which need to be evaluated before the most desirable option is selected. To determine what behavior is most desirable at any given point, the nervous system must integrate external conditions (e.g., predation risk) with current internal drives (e.g., hunger state), thus trading off the costs and benefits of different alternatives before deciding which one to choose. For example, a hungry animal is more likely to choose a behavioral option that involves risks because the value placed on foraging is greater than the value placed on other alternatives such as hiding. If the benefit of finding a meal outweighs the estimated cost of being attacked by a predator, the decision is to forage. If the value placed on foraging is low because the animal is satiated, other behavioral options become more valuable and behavioral output will shift toward less risky activities. The literature on value-based decision making, especially with a focus on prey behavior in predator-prey interactions, is extensive and covers a wide range of organisms (e.g., [110,169]).

The relatively new field of “neuroeconomics” is concerned with the neural underpinnings of value-based decision making in humans and other non-human primates [170,171] and there is now fast growing interest in understanding the neural mechanisms that govern cost-benefit calculations. An increasing number of studies performed in humans and other primates are combining non-invasive techniques such as functional magnetic resonance imaging or cortical recordings with discrimination tasks or cognitive experiments [172–174]. The complexity of the mammalian brain, however, presents many challenges. It is difficult to directly correlate neuronal activity and behavioral

expression and to obtain detailed information on neural circuit organization, cellular mechanisms, and the interplay between sensory and motor systems. Decision-making circuitry has been studied quite extensively in various invertebrates, but descriptions of neural mechanisms underlying value-based (economic) behavioral decisions are rare [175,176]. This is surprising because behavioral experiments have shown that invertebrates make decisions that are not always simple and reflexive, but are often the product of careful cost-benefit calculations [110,169,177]. Thus, invertebrates are ideally suited to study the neural mechanisms underlying value-based decision making. In the following section, we will review some recent experiments on value-based decision making in response to predatory threat, and provide two examples where economic decisions can be linked to identifiable neural circuitry.

Crayfish

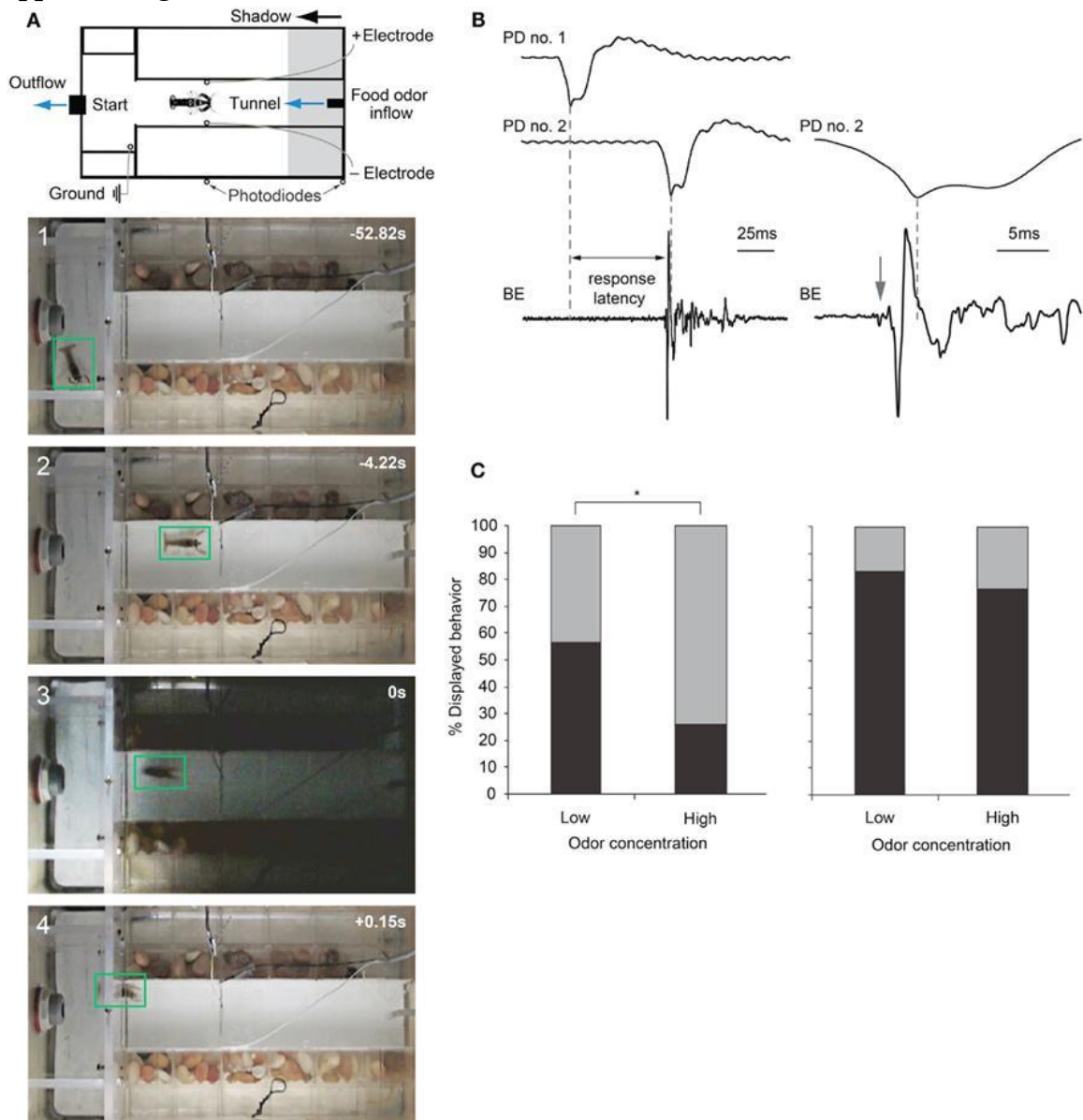
When juvenile crayfish are exposed to fast-moving shadows while foraging in an artificial stream environment, they respond by choosing one of two behavioral actions: they either freeze in place and remain motionless for several seconds before resuming foraging or they produce a tail-flip mediated by the MG neuron that propels the animal backward and away from the approaching shadow and the expected food source ([133]; **Fig. A1.6A**). Thus, crayfish respond to visual threat signals that simulate the imminent attack of a predator with defensive behaviors that are discrete and incompatible. When Liden and Herberholz [133] exposed groups of juvenile crayfish to different shadow velocities, they found that the frequencies of the two behavioral responses were

dependent on shadow speed. Slower moving shadows evoked more tail-flips than freezing, but as shadow speed increased the frequency of tail-flips decreased and crayfish primarily produced freezing behavior. The study also showed that different individuals choose different anti-predator strategies when exposed to one type of shadow. Some animals decided to freeze in response to the danger signal while others decided to tail-flip. This suggests that different crayfish have different thresholds for each behavioral action, but what underlies this difference remains to be determined. Because all tested animals were of identical size and shared the same social experiences and feeding history, other intrinsic factors must be responsible.

Recently, Liden et al. [134] used the same experimental design to show that crayfish base their escape decisions on the values of each behavioral option. They measured escape latencies for shadow-induced MG-mediated tail-flips by comparing photodiode signals with bath electrode recordings that non-invasively captured neural and muscular activity produced during tail-flips (*Fig. A1.6B*). They found that very fast approaching shadows become inescapable because they collided with the animal before a tail-flip could be generated. Moreover, tail-flips are costly because they move the animal away from the expected food source. Thus, the observed suppression of tail-flipping in favor of freezing in animals facing inescapable shadows, where the value of a tail-flip would be low, reflects the output product of an “economic” decision-making process. Although tail-flipping is considered a less risky strategy when experiencing a predator attack, crayfish also defaulted to freezing behavior when the expected reward became

more valuable. When food odor concentration in the artificial stream was increased 10-fold, shadows that evoked mostly tail-flips under standard conditions now generated mainly freezing behavior. Interestingly, if high food value was paired with a strong predator signal (a slow moving shadow) that reliably evoked tail-flips under regular conditions, the behavioral shift toward freezing was less pronounced. Thus, a strong predator signal was able to override the exaggerated food incentive (*Fig. AI.6C*). This illustrates that crayfish calculate the costs and benefits of different behavioral options and they carefully weigh predation risk against expected reward, eventually selecting the most valuable behavioral choice [134]. Because these observed tail-flips are always generated by activation of MG neurons and the MG circuit is accessible for neurophysiological and neurochemical experiments, the neural workings underlying value-based decision making in crayfish can now be investigated on the cellular level. This establishes the crayfish as an important new model for studying the neuroeconomics underlying predator avoidance. However, to understand the decision-making process on the network level, identification of interneurons that form the descending visual pathway for freezing behavior will be required.

Figure A1.6. Escape choices and neural activation in crayfish exposed to approaching shadows.



(A) Experimental diagram and four video frames illustrating a crayfish foraging (first two panels) and then tail-flipping (last two panels) in response to a fast approaching shadow with time in seconds. **(B)** Left: example recordings from photodiodes positioned on the tank walls (PD no. 1 and PD no. 2) when a shadow passes by, and from bath electrodes (BE) located inside the tank that capture field potentials generated during a tail-flip.

Right: Traces from PD no. 2 and BE at higher temporal resolution. In this example, animal initiated a tail-flip response (arrow) 4 ms before the shadow collided with the animal and produced the peak response in PD no. 2. The first small deflection (arrow) in the BE trace is due to MG neuron activation, while the large phasic potential and the smaller more erratic potentials that follow are due to muscular activity during tail-flips. (C) Left: when exposed to a medium speed shadow (2 m/s), crayfish produce fewer tail-flips (black bars) and more freezing (gray bars) when food odor concentration flowing through the tank is high. Right: when exposed to slower (1 m/s) shadows, the effect of food odor concentration on behavioral choice is less pronounced. (A) Modified from Liden and Herberholz [133]. (B,C) Modified from Liden et al. [134].

Sea Slug

The marine snail has been a fruitful model for studying the neural mechanisms underlying decision making and behavioral choice. Using a “competing behaviors” paradigm, early work suggested that different incompatible behaviors were organized in a hierarchical model, each controlled by command-like neurons that produced one behavior while inhibiting others. For example, when the sea slug was feeding, avoidance withdrawal in response to a tactile stimulus was suppressed [178]. This suppression is caused by identified interneurons that are part of the motor circuit that generates feeding. Thus, feeding behavior takes precedence over withdrawal, while escape swimming dominates most other behaviors, including feeding [179]. The A1 neurons, a bilateral pair of interneurons located in the cerebropleural ganglion of the snail, are necessary elements of the escape swimming behavior, and their activity also inhibits feeding behavior.

Recent work, however, has shown that sea slugs base their decisions on cost-benefit computations ([180]; *Fig A1.7*). When presented with food stimuli, feeding behavior or avoidance behavior can be activated, depending on the concentration of the

food stimulus and the current behavioral state of the animal. At low concentrations and in satiated animals, food stimuli typically evoked avoidance behavior. When the threshold for feeding was exceeded, avoidance behavior was suppressed, and in hungry snails, even nociceptive stimuli elicited feeding behavior (*Fig. AI.7A*). This suggests both appetitive and noxious stimuli provide inputs to neural networks underlying feeding and avoidance behavior, but the final behavioral decision is determined by hunger state. Thus, in partially or fully satiated animals, the value placed on feeding behavior is low while it is high for avoidance behavior that protects the animal from predators. Using a simple cost-benefit analysis, the animal weighs nutritional needs against predator risk and selects the most desirable choice ([180]; *Fig. AI.7B*). Importantly, feeding and avoidance can be observed as fictive motor patterns in isolated central nervous systems of the snail and some of the neurons controlling these behaviors have been individually identified [181]. Moreover, in isolated central nervous systems, spontaneous feeding network activity reflects feeding thresholds of the nervous system donors (for proboscis extension and biting); while orienting turns were more frequent in low-feeding threshold donors, avoidance turns dominated in high-feeding threshold donors. When a “command” neuron in the feeding network of a high-feeding threshold donor was electrically stimulated, avoidance turns were converted to orienting turns [182]. Thus, the neurophysiological and neurochemical mechanisms underlying cost-benefit calculations can now be investigated in the isolated nervous system of this animal. This is expected to

substantially contribute to our cellular understanding of value-based decision-making processes.

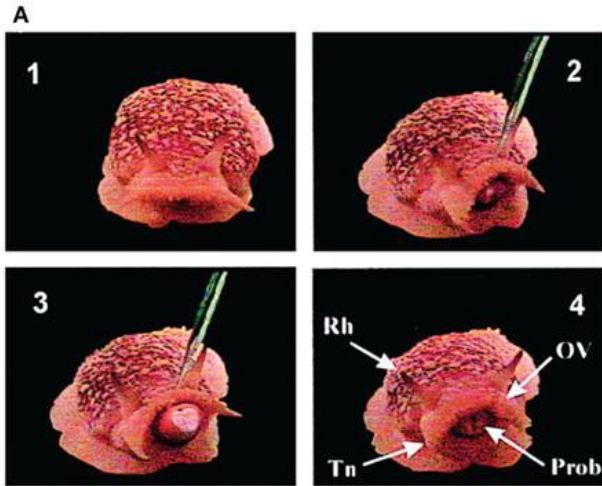
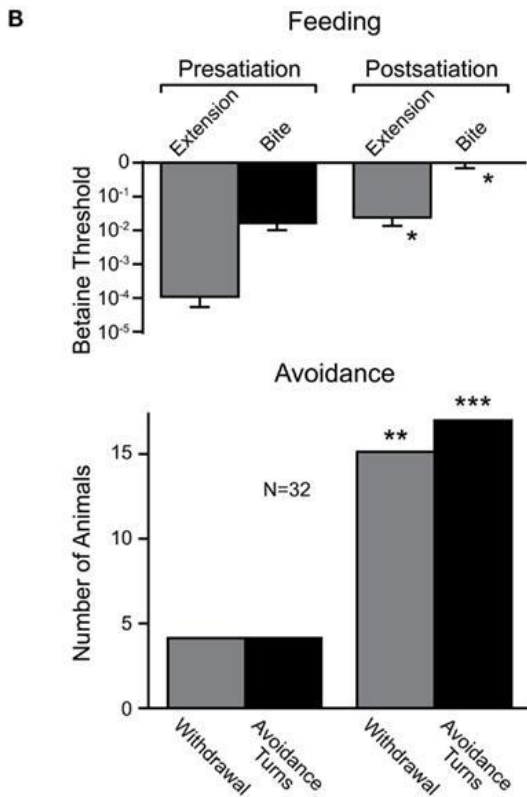


Figure A1.7. Effects of internal state on behavioral choice in a sea slug.

(A) Four video frames showing feeding behavior in *Pleurobranchaea californica*. Betaine application induces an orienting turn (panel 2) followed by proboscis extension and biting (panel 3). Chemosensory structures (panel 4): rhinophore (Rh), oral veil (OV), tentacle (Tn), and proboscis (Prob). (B) Partial satiation raised the threshold for proboscis extension and biting (i.e., feeding), and increased the frequency of withdrawal and turns (i.e., avoidance) in response to betaine. Modified from Gillette et al. [180].



Conclusion and Future Directions

Recent work in the arthropods discussed suggests that the escape behavior of all may be more complex and varied than has generally been assumed. Quantitative ethograms that divide complex escape maneuvers into a sequence of simpler events can help identify variability within each system. Moreover, combining ethograms with measures of neural structure or neural activity can elucidate the link between discrete motor actions within a series of behavioral events and the corresponding underlying neural mechanisms [183,184].

Based on the high-speed video analysis of the behavior of fruit flies and locusts, a reexamination of the “simple” escape behavior of other arthropods is warranted. Perhaps an analysis at a temporal resolution comparable to that of the speed of production of these behaviors will uncover a degree of flexibility and control not previously appreciated in these animals as well. For example, while the escape tail-flip and freezing behavior of the crayfish in response to visual stimuli have been assumed to be two distinct behaviors, which has been supported by video analysis at 250 fps [134], possibly higher speed analysis will show that these distinct decisions are in fact part of a single escape sequence. Such an observation could provide direction in the search for the neural circuit(s) responsible for freezing, the identification of which would provide a unique opportunity to explore decision making between two circuits underlying known behavioral alternatives.

While this new appreciation for the complexity of arthropod escape behavior has reinvigorated work on giant fibers and escape behavior, it raises two significant issues. First, if the giant fiber systems previously assumed to underlie observed escape behaviors are not in fact necessary or sufficient for the production of these behaviors, what circuits are? While Fotowat et al. [115] have made initial progress toward characterizing the activity of part of an additional putative escape circuit, the neurons will have to be anatomically identified and the circuit fleshed out in future work. Second, if the giant fibers are not involved in escape behaviors produced under existing experimental contexts, what contexts elicit their recruitment? It would be exceedingly wasteful for the largest axons in the fruit fly's nerve cord to go unused. There must be some combination of internal states and external stimulus conditions that lead to GF-mediated escape response and work should be directed toward identifying these constraints.

It is likely other arthropod models will have a similar redundancy in escape circuitry as has been described in the crayfish. Thus, a comprehensive understanding of decision making during predator avoidance will have to wait until all pathways and not just parts of some are fully characterized (*Fig. A1.5*). While the identification of all escape circuits in any one arthropod is non-trivial, that parts of both command and non-command systems have been successfully identified in various arthropods is evidence of the feasibility of such a research program. For example, the LG neurons in grapsid crab are fully characterized and individually identifiable cells that can be accessed for intracellular recordings in live animals. The activity of these neurons is highly correlated

with behavioral output, which suggests that they play a major role in mediating escape decisions. However, relevant analysis of the complete escape circuit is still missing and descending pathways that orchestrate motor actions need to be identified.

As such, future work should focus on completing the picture of currently known circuits, where often substantial sensory or motor elements remain poorly characterized, as well as identifying unknown but hinted at command or non-command circuits. This hunt for currently uncharacterized circuits might be aided by the possible similarity to and knowledge of already characterized systems found in related species (*Fig. A1.5*). For instance, the poorly studied non-giant tail-flip circuit in crayfish might share characteristics with that of the DCMD circuit in locusts and knowledge of the structure and function of the DCMD circuit could aid in the identification and characterization of this escape system.

Due to the assumption that giant fiber systems were a singular system responsible for the production of all escape behaviors, there is currently much confusion as to what discrete escape behavior is subserved by what specific circuit. Since it now appears that there are likely many circuits that produce a range of escape behaviors, the spectrum of these behaviors and the stimulus conditions that lead to their display will need to be carefully cataloged and behavioral assays developed that can differentiate them. However, without the ability to simultaneously record both escape behaviors and neural activity, it will be difficult to ascribe a discrete escape sequence or subcomponent of escape behavior to a particular circuit or set of neurons. For this, the use of telemetry that

allows for in vivo recordings in freely behaving animals [116,117] will have to be expanded to other invertebrates. While it will be some time before these techniques can be adapted to all models, some should be able to benefit immediately. Arguably, these techniques might have the most to offer in models like the crayfish where large parts of a number of well-described escape circuits have long been worked out (*Fig. A1.5A*). In such a model, not only can the function of identified neurons be correlated to the performance of distinct components of a complex behavioral sequence, but also how an animal chooses between a range of escape behaviors might be elucidated. Recordings with implanted electrodes or bath electrodes, which non-invasively record neural and muscular field potentials in freely behaving animals, have begun to reveal some of the basic neural patterns underlying escape decisions in crayfish [133,134,136,185].

There is a notable lack of neuroethological studies focused on escape mechanisms produced under natural conditions. While staged encounters with natural predators in the laboratory provide some insight into the interplay between neural function and ecologically relevant escape behavior, these studies are sparse. Field studies on the other hand are often focused on ecology and behavior and not designed to investigate neural processes. Occasionally, data sets obtained separately in the field and laboratory allow for a comparative view and for correlating firing patterns of individual neurons and natural escape behavior (e.g., [163]); however, the development of new technologies that permit direct measures of nervous system function in natural settings is highly desirable.

Finally, the neuromodulation of escape behavior by monoamines such as octopamine, serotonin and dopamine is worth further exploration. Although a number of the escape circuits discussed have been shown to be responsive to the application or removal of monoamines [186–191], little is known about the context in which these monoamines affect the performance of behavioral decisions. Since most invertebrate aminergic effects are mediated by metabotropic receptors that can have a gradual but pronounced impact on behavior, monoamines are an attractive candidate for how a nervous system may be biased toward the production of one behavior over another [192,193]. Through these monoamines, escape behaviors might modulate or be modulated by competing behaviors. Monoamines (e.g., dopamine and serotonin) have been targeted for roles in decision making and the encoding of punishment and reward [194]. Thus, the study of monoamines in the context of the evolutionarily critical task of predator avoidance provides an excellent opportunity to explore the postulated neurochemical currency of neuroeconomic decision making. Unfortunately, little work on value-based decision making has been undertaken with invertebrates despite the description of numerous value-based decisions that are likely to involve identified circuits including those mediating escape or avoidance behavior. Research in this field is currently limited to a few invertebrate species, namely the previously discussed sea slug and crayfish, where basic neural mechanisms underlying cost-benefit computations have been partially uncovered. It is surprising that researchers interested in neuroeconomics have not taken greater advantage of these highly tractable models, as they are likely to

contribute much to this new field, as they have contributed to neuroscience in general [195]. Possibly we have just begun to realize that invertebrate models are ideally suited to answer some of the most challenging questions faced today by neuroscience research.

Bibliography

References

1. Peng H, Chung P, Long F, Qu L, Jenett A, Seeds AM, et al. BrainAligner: 3D registration atlases of *Drosophila* brains. *Nat Methods*. 2011;8: 493–500.
2. Ronneberger O, Liu K, Rath M, Rueß D, Mueller T, Skibbe H, et al. ViBE-Z: a framework for 3D virtual colocalization analysis in zebrafish larval brains. *Nat Methods*. 2012;9: 735–742.
3. Portugues R, Feierstein CE, Engert F, Orger MB. Whole-brain activity maps reveal stereotyped, distributed networks for visuomotor behavior. *Neuron*. 2014;81: 1328–1343.
4. Randlett O, Wee CL, Naumann EA, Nnaemeka O, Schoppik D, Fitzgerald JE, et al. Whole-brain activity mapping onto a zebrafish brain atlas. *Nat Methods*. 2015;12: 1039–1046.
5. Higashijima S, Okamoto H, Ueno N, Hotta Y, Eguchi G. High-frequency generation of transgenic zebrafish which reliably express GFP in whole muscles or the whole body by using promoters of zebrafish origin. *Dev Biol*. 1997;192: 289–299.
6. Jessen JR, Willett CE, Lin S. Artificial chromosome transgenesis reveals long-distance negative regulation of *rag1* in zebrafish. *Nat Genet*. 1999;23: 15–16.
7. Suster ML, Sumiyama K, Kawakami K. Transposon-mediated BAC transgenesis in zebrafish and mice. *BMC Genomics*. [biomedcentral.com; 2009; Available: http://www.biomedcentral.com/1471-2164/10/477/](http://www.biomedcentral.com/1471-2164/10/477/)
8. Bayer TA, Campos-Ortega JA. A transgene containing *lacZ* is expressed in primary sensory neurons in zebrafish. *Development*. 1992;115: 421–426.
9. Kawakami K, Takeda H, Kawakami N, Kobayashi M, Matsuda N, Mishina M. A Transposon-Mediated Gene Trap Approach Identifies Developmentally Regulated Genes in Zebrafish. *Dev Cell*. 2004;7: 133–144.
10. Parinov S, Kondrichin I, Korzh V, Emelyanov A. Tol2 transposon-mediated enhancer trap to identify developmentally regulated zebrafish genes in vivo. *Dev Dyn*. 2004;231: 449–459.
11. Davison JM, Akitake CM, Goll MG, Rhee JM, Gosse N, Baier H, et al. Transactivation from Gal4-VP16 transgenic insertions for tissue-specific cell labeling and ablation in zebrafish. *Dev Biol*. 2007;304: 811–824.
12. Scott EK, Mason L, Arrenberg AB, Ziv L, Gosse NJ, Xiao T, et al. Targeting neural circuitry in zebrafish using GAL4 enhancer trapping. *Nat Methods*. Nature Publishing

Group; 2007;4: 323–326.

13. Asakawa K, Suster ML, Mizusawa K, Nagayoshi S, Kotani T, Urasaki A, et al. Genetic dissection of neural circuits by Tol2 transposon-mediated Gal4 gene and enhancer trapping in zebrafish. *Proc Natl Acad Sci U S A*. 2008;105: 1255–1260.
14. Scott EK, Baier H. The cellular architecture of the larval zebrafish tectum, as revealed by gal4 enhancer trap lines. *Front Neural Circuits*. 2009;3: 13.
15. Pfeiffer BD, Jenett A, Hammonds AS, Ngo T-TB, Misra S, Murphy C, et al. Tools for neuroanatomy and neurogenetics in *Drosophila*. *Proc Natl Acad Sci U S A*. 2008;105: 9715–9720.
16. Jenett A, Rubin GM, Ngo T-TB, Shepherd D, Murphy C, Dionne H, et al. A GAL4-driver line resource for *Drosophila* neurobiology. *Cell Rep*. 2012;2: 991–1001.
17. Pfeiffer BD, Ngo T-TB, Hibbard KL, Murphy C, Jenett A, Truman JW, et al. Refinement of tools for targeted gene expression in *Drosophila*. *Genetics*. 2010;186: 735–755.
18. Faucherre A, López-Schier H. Delaying Gal4-driven gene expression in the zebrafish with morpholinos and Gal80. *PLoS One*. 2011;6: e16587.
19. Stockinger P, Kvitsiani D, Rotkopf S, Tirián L, Dickson BJ. Neural circuitry that governs *Drosophila* male courtship behavior. *Cell*. 2005;121: 795–807.
20. Satou C, Kimura Y, Hirata H, Suster ML, Kawakami K, Higashijima S-I. Transgenic tools to characterize neuronal properties of discrete populations of zebrafish neurons. *Development*. 2013;140: 3927–3931.
21. Otsuna H, Hutcheson DA, Duncan RN, McPherson AD, Scoresby AN, Gaynes BF, et al. High-resolution analysis of central nervous system expression patterns in zebrafish Gal4 enhancer-trap lines. *Dev Dyn*. 2015;244: 785–796.
22. Bergeron SA, Hannan MC, Codore H, Fero K, Li GH, Moak Z, et al. Brain selective transgene expression in zebrafish using an NRSE derived motif. *Front Neural Circuits*. 2012;6: 110.
23. Xie X, Mathias JR, Smith M-A, Walker SL, Teng Y, Distel M, et al. Silencer-delimited transgenesis: NRSE/RE1 sequences promote neural-specific transgene expression in a NRSF/REST-dependent manner. *BMC Biol*. 2013;10: 93.
24. Bartel DP. MicroRNAs: target recognition and regulatory functions. *Cell*. 2009;136: 215–233.
25. Mishima Y, Fukao A, Kishimoto T, Sakamoto H, Fujiwara T, Inoue K. Translational inhibition by deadenylation-independent mechanisms is central to microRNA-mediated

- silencing in zebrafish. *Proc Natl Acad Sci U S A*. 2012;109: 1104–1109.
26. Subtelny AO, Eichhorn SW, Chen GR, Sive H, Bartel DP. Poly(A)-tail profiling reveals an embryonic switch in translational control. *Nature*. 2014;508: 66–71.
 27. Rath M, Nitschke R, Filippi A, Ronneberger O, Driever W. Generation of high quality multi-view confocal 3D datasets of zebrafish larval brains suitable for analysis using Virtual Brain Explorer (ViBE-Z) software. *Nature Protocol Exchange*; 2012; Available: <https://www.scientificprotocols.org/protocols/generation-of-high-quality-multi-view-confocal-3d-datasets-of-zebrafish-larval-brains-suitable-for-analysis-using-virtual-brain-explorer-vibe-z-software>
 28. Burgess HA, Johnson SL, Granato M. Unidirectional startle responses and disrupted left–right co-ordination of motor behaviors in robo3 mutant zebrafish. *Genes Brain Behav*. Blackwell Publishing Ltd; 2009;8: 500–511.
 29. Tabor KM, Bergeron SA, Horstick EJ, Jordan DC, Aho V, Porkka-Heiskanen T, et al. Direct activation of the Mauthner cell by electric field pulses drives ultrarapid escape responses. *J Neurophysiol*. 2014;112: 834–844.
 30. Sivasubbu S, Balciunas D, Davidson AE, Pickart MA, Hermanson SB, Wangenstein KJ, et al. Gene-breaking transposon mutagenesis reveals an essential role for histone H2afza in zebrafish larval development. *Mech Dev*. 2006;123: 513–529.
 31. Bergeron SA, Carrier N, Li GH, Ahn S, Burgess HA. Gsx1 expression defines neurons required for prepulse inhibition. *Mol Psychiatry*. 2015;20: 974–985.
 32. Varshney GK, Lu J, Gildea DE, Huang H, Pei W, Yang Z, et al. A large-scale zebrafish gene knockout resource for the genome-wide study of gene function. *Genome Res*. 2013;23: 727–735.
 33. Schneider CA, Rasband WS, Eliceiri KW. NIH Image to ImageJ: 25 years of image analysis. *Nat Methods*. 2012;9: 671–675.
 34. Wan Y, Otsuna H, Chien C-B, Hansen C. FluoRender: An Application of 2D Image Space Methods for 3D and 4D Confocal Microscopy Data Visualization in Neurobiology Research. *IEEE Pac Vis Symp*. 2012; 201–208.
 35. Bae Y-K, Kani S, Shimizu T, Tanabe K, Nojima H, Kimura Y, et al. Anatomy of zebrafish cerebellum and screen for mutations affecting its development. *Dev Biol*. 2009;330: 406–426.
 36. Satou C, Kimura Y, Higashijima S-I. Generation of multiple classes of V0 neurons in zebrafish spinal cord: progenitor heterogeneity and temporal control of neuronal diversity. *J Neurosci*. 2012;32: 1771–1783.

37. Hong E, Santhakumar K, Akitake CA, Ahn SJ, Thisse C, Thisse B, et al. Cholinergic left-right asymmetry in the habenulo-interpeduncular pathway. *Proc Natl Acad Sci U S A*. 2013;110: 21171–21176.
38. Mueller T, Wullimann MF. *Atlas of Early Zebrafish Brain Development: A Tool for Molecular Neurogenetics*. Gulf Professional Publishing; 2005.
39. Sprague J, Bayraktaroglu L, Clements D, Conlin T, Fashena D, Frazer K, et al. The Zebrafish Information Network: the zebrafish model organism database. *Nucleic Acids Res*. 2006;34: D581–5.
40. Horstick EJ, Jordan DC, Bergeron SA, Tabor KM, Serpe M, Feldman B, et al. Increased functional protein expression using nucleotide sequence features enriched in highly expressed genes in zebrafish. *Nucleic Acids Res*. 2015;43: e48.
41. Baek D, Villén J, Shin C, Camargo FD, Gygi SP, Bartel DP. The impact of microRNAs on protein output. *Nature*. 2008;455: 64–71.
42. Wienholds E, Kloosterman WP, Miska E, Alvarez-Saavedra E, Berezikov E, de Bruijn E, et al. MicroRNA expression in zebrafish embryonic development. *Science*. 2005;309: 310–311.
43. Nachtigall PG, Dias MC, Pinhal D. Evolution and genomic organization of muscle microRNAs in fish genomes. *BMC Evol Biol*. 2014;14: 196.
44. Pitman JL, McGill JJ, Keegan KP, Allada R. A dynamic role for the mushroom bodies in promoting sleep in *Drosophila*. *Nature*. 2006;441: 753–756.
45. Pool A-H, Kvello P, Mann K, Cheung SK, Gordon MD, Wang L, et al. Four GABAergic interneurons impose feeding restraint in *Drosophila*. *Neuron*. 2014;83: 164–177.
46. Jungke P, Hammer J, Hans S, Brand M. Isolation of Novel CreER T2 -Driver Lines in Zebrafish Using an Unbiased Gene Trap Approach. *PLoS One*. Public Library of Science; 2015;10: e0129072.
47. Yokogawa T, Hannan MC, Burgess HA. The dorsal raphe modulates sensory responsiveness during arousal in zebrafish. *J Neurosci. Soc Neuroscience*; 2012;32: 15205–15215.
48. Kimura Y, Satou C, Fujioka S, Shoji W, Umeda K, Ishizuka T, et al. Hindbrain V2a neurons in the excitation of spinal locomotor circuits during zebrafish swimming. *Curr Biol*. 2013;23: 843–849.
49. Provost E, Rhee J, Leach SD. Viral 2A peptides allow expression of multiple proteins from a single ORF in transgenic zebrafish embryos. *Genesis*. 2007;45: 625–629.
50. Urasaki A, Morvan G, Kawakami K. Functional dissection of the Tol2 transposable element

- identified the minimal cis-sequence and a highly repetitive sequence in the subterminal region essential for transposition. *Genetics*. 2006;174: 639–649.
51. Groth AC, Olivares EC, Thyagarajan B, Calos MP. A phage integrase directs efficient site-specific integration in human cells. *Proc Natl Acad Sci U S A*. 2000;97: 5995–6000.
 52. Hu G, Goll MG, Fisher S. ΦC31 integrase mediates efficient cassette exchange in the zebrafish germline. *Dev Dyn*. 2011;240: 2101–2107.
 53. Gohl DM, Silies MA, Gao XJ, Bhalerao S, Luongo FJ, Lin C-C, et al. A versatile in vivo system for directed dissection of gene expression patterns. *Nat Methods*. 2011;8: 231–237.
 54. Park HC, Kim CH, Bae YK, Yeo SY, Kim SH, Hong SK, et al. Analysis of upstream elements in the HuC promoter leads to the establishment of transgenic zebrafish with fluorescent neurons. *Dev Biol*. 2000;227: 279–293.
 55. Kimura Y, Satou C, Higashijima S-I. V2a and V2b neurons are generated by the final divisions of pair-producing progenitors in the zebrafish spinal cord. *Development*. 2008;135: 3001–3005.
 56. Tay TL, Ronneberger O, Ryu S, Nitschke R, Driever W. Comprehensive catecholaminergic projectome analysis reveals single-neuron integration of zebrafish ascending and descending dopaminergic systems. *Nat Commun*. Nature Publishing Group; 2011;2: 171.
 57. Zhang Y, Werling U, Edelman W. SLiCE: a novel bacterial cell extract-based DNA cloning method. *Nucleic Acids Res*. 2012;40: e55.
 58. Kimura Y, Hisano Y, Kawahara A, Higashijima S-I. Efficient generation of knock-in transgenic zebrafish carrying reporter/driver genes by CRISPR/Cas9-mediated genome engineering. *Sci Rep*. nature.com; 2014;4: 6545.
 59. Lillesaar C, Stigloher C, Tannhäuser B, Wullmann MF, Bally-Cuif L. Axonal projections originating from raphe serotonergic neurons in the developing and adult zebrafish, *Danio rerio*, using transgenics to visualize raphe-specific *pet1* expression. *J Comp Neurol*. 2009;512: 158–182.
 60. Xi Y, Yu M, Godoy R, Hatch G, Poitras L, Ekker M. Transgenic zebrafish expressing green fluorescent protein in dopaminergic neurons of the ventral diencephalon. *Dev Dyn*. 2011;240: 2539–2547.
 61. Choi J, Dong L, Ahn J, Dao D, Hammerschmidt M, Chen J-N. FoxH1 negatively modulates *flk1* gene expression and vascular formation in zebrafish. *Dev Biol*. 2007;304: 735–744.
 62. Masai I, Lele Z, Yamaguchi M, Komori A, Nakata A, Nishiwaki Y, et al. N-cadherin mediates retinal lamination, maintenance of forebrain compartments and patterning of retinal neurites. *Development*. 2003;130: 2479–2494.

63. Bernardos RL, Raymond PA. GFAP transgenic zebrafish. *Gene Expr Patterns*. 2006;6: 1007–1013.
64. McLean DL, Fan J, Higashijima S-I, Hale ME, Fetcho JR. A topographic map of recruitment in spinal cord. *Nature*. 2007;446: 71–75.
65. Pittman AJ, Law M-Y, Chien C-B. Pathfinding in a large vertebrate axon tract: isotopic interactions guide retinotectal axons at multiple choice points. *Development*. 2008;135: 2865–2871.
66. Nechiporuk A, Linbo T, Poss KD, Raible DW. Specification of epibranchial placodes in zebrafish. *Development*. 2007;134: 611–623.
67. Kinkhabwala A, Riley M, Koyama M, Monen J, Satou C, Kimura Y, et al. A structural and functional ground plan for neurons in the hindbrain of zebrafish. *Proc Natl Acad Sci U S A*. 2011;108: 1164–1169.
68. Preibisch S, Saalfeld S, Tomancak P. Globally optimal stitching of tiled 3D microscopic image acquisitions. *Bioinformatics*. 2009;25: 1463–1465.
69. Schindelin J, Arganda-Carreras I, Frise E, Kaynig V, Longair M, Pietzsch T, et al. Fiji: an open-source platform for biological-image analysis. *Nat Methods*. 2012;9: 676–682.
70. Amo R, Aizawa H, Takahoko M, Kobayashi M, Takahashi R, Aoki T, et al. Identification of the zebrafish ventral habenula as a homolog of the mammalian lateral habenula. *J Neurosci*. 2010;30: 1566–1574.
71. Mueller T. What is the Thalamus in Zebrafish? *Front Neurosci*. 2012;6: 64.
72. Ulitsky I, Shkumatava A, Jan CH, Subtelny AO, Koppstein D, Bell GW, et al. Extensive alternative polyadenylation during zebrafish development. *Genome Res*. 2012;22: 2054–2066.
73. Koga A, Cheah FSH, Hamaguchi S, Yeo GH, Chong SS. Germline transgenesis of zebrafish using the medaka Tol1 transposon system. *Dev Dyn*. 2008;237: 2466–2474.
74. LaFave MC, Varshney GK, Burgess SM. GeIST: a pipeline for mapping integrated DNA elements. *Bioinformatics*. 2015;31: 3219–3221.
75. Rozen S, Skaletsky H. Primer3 on the WWW for general users and for biologist programmers. *Methods Mol Biol*. 2000;132: 365–386.
76. Marquart GD, Tabor KM, Brown M, Strykowski JL, Varshney GK, LaFave MC, et al. A 3D Searchable Database of Transgenic Zebrafish Gal4 and Cre Lines for Functional Neuroanatomy Studies. *Front Neural Circuits*. 2015;9: 1566.

77. Rohlfing T, Maurer CR Jr. Nonrigid image registration in shared-memory multiprocessor environments with application to brains, breasts, and bees. *IEEE Trans Inf Technol Biomed.* 2003;7: 16–25.
78. Avants BB, Epstein CL, Grossman M, Gee JC. Symmetric diffeomorphic image registration with cross-correlation: evaluating automated labeling of elderly and neurodegenerative brain. *Med Image Anal.* 2008;12: 26–41.
79. Avants BB, Tustison NJ, Song G, Cook PA, Klein A, Gee JC. A reproducible evaluation of ANTs similarity metric performance in brain image registration. *Neuroimage.* 2011;54: 2033–2044.
80. Higashijima S, Hotta Y, Okamoto H. Visualization of cranial motor neurons in live transgenic zebrafish expressing green fluorescent protein under the control of the islet-1 promoter/enhancer. *J Neurosci.* 2000;20: 206–218.
81. Wen L, Wei W, Gu W, Huang P, Ren X, Zhang Z, et al. Visualization of monoaminergic neurons and neurotoxicity of MPTP in live transgenic zebrafish. *Dev Biol.* 2008;314: 84–92.
82. Fosque BF, Sun Y, Dana H, Yang C-T, Ohyama T, Tadross MR, et al. Neural circuits. Labeling of active neural circuits in vivo with designed calcium integrators. *Science.* 2015;347: 755–760.
83. Burgess HA, Johnson SL, Granato M. Unidirectional startle responses and disrupted left–right co-ordination of motor behaviors in robo3 mutant zebrafish. *Genes Brain Behav. Wiley Online Library;* 2009;8: 500–511.
84. Inoue D, Wittbrodt J. One for all—a highly efficient and versatile method for fluorescent immunostaining in fish embryos. *PLoS One.* 2011;6: e19713.
85. Huttenlocher DP, Klanderman GA, Rucklidge WJ. Comparing images using the Hausdorff distance. *IEEE Trans Pattern Anal Mach Intell.* 1993;15: 850–863.
86. Klein A, Andersson J, Ardekani BA, Ashburner J, Avants B, Chiang M-C, et al. Evaluation of 14 nonlinear deformation algorithms applied to human brain MRI registration. *Neuroimage.* 2009;46: 786–802.
87. Murphy K, van Ginneken B, Reinhardt JM, Kabus S, Ding K, Deng X, et al. Evaluation of registration methods on thoracic CT: the EMPIRE10 challenge. *IEEE Trans Med Imaging.* 2011;30: 1901–1920.
88. Marquart GD, Tabor KM, Horstick EJ, Brown M, Geoca AK, Polys NF, et al. Supporting data for “High precision registration between zebrafish brain atlases using symmetric diffeomorphic normalization” [Internet]. *GigaScience Database;* 2017. doi:10.5524/100322
89. Ware C, Franck G. Viewing a graph in a virtual reality display is three times as good as a 2D

- diagram. Proceedings of 1994 IEEE Symposium on Visual Languages. 1994. pp. 182–183.
90. Ota D, Loftin B, Saito T, Lea R, Keller J. Virtual reality in surgical education. *Comput Biol Med.* 1995;25: 127–137.
 91. Bowman DA, McMahan RP. Virtual Reality: How Much Immersion Is Enough? *Computer .* 2007;40: 36–43.
 92. Henry JAG, Polys NF. The effects of immersion and navigation on the acquisition of spatial knowledge of abstract data networks. *Procedia Comput Sci.* 2010;1: 1737–1746.
 93. Rohlfing T. Image similarity and tissue overlaps as surrogates for image registration accuracy: widely used but unreliable. *IEEE Trans Med Imaging.* 2012;31: 153–163.
 94. Canfield JG, Rose GJ. Activation of Mauthner neurons during prey capture. *J Comp Physiol A.* Springer-Verlag; 1993;172: 611–618.
 95. Zottoli SJ, Cioni C, Seyfarth E-A. Reticulospinal neurons in anamniotic vertebrates: a celebration of Alberto Stefanelli’s contributions to comparative neuroscience. *Brain Res Bull.* 2007;74: 295–306.
 96. Furshpan EJ, Furukawa T. Intracellular and extracellular responses of the several regions of the Mauthner cell of the goldfish. *J Neurophysiol.* 1962;25: 732–771.
 97. Korn H, Faber DS. The Mauthner cell half a century later: a neurobiological model for decision-making? *Neuron.* 2005;47: 13–28.
 98. Eaton RC, DiDomenico R, Nissanov J. Flexible body dynamics of the goldfish C-start: implications for reticulospinal command mechanisms. *J Neurosci.* 1988;8: 2758–2768.
 99. O’Malley DM, Kao YH, Fetcho JR. Imaging the functional organization of zebrafish hindbrain segments during escape behaviors. *Neuron.* 1996;17: 1145–1155.
 100. Liu KS, Fetcho JR. Laser ablations reveal functional relationships of segmental hindbrain neurons in zebrafish. *Neuron.* 1999;23: 325–335.
 101. Zottoli SJ, Newman BC, Rieff HI, Winters DC. Decrease in occurrence of fast startle responses after selective Mauthner cell ablation in goldfish (*Carassius auratus*). *J Comp Physiol A.* 1999;184: 207–218.
 102. Marquart GD, Tabor KM, Horstick EJ, Brown M, Geoca AK, Polys NF, et al. High precision registration between zebrafish brain atlases using symmetric diffeomorphic normalization. *Gigascience.* 2017; doi:10.1093/gigascience/gix056
 103. Pisharath H, Rhee JM, Swanson MA, Leach SD, Parsons MJ. Targeted ablation of beta cells in the embryonic zebrafish pancreas using *E. coli* nitroreductase. *Mech Dev.* 2007;124:

218–229.

104. Lin JY, Lin MZ, Steinbach P, Tsien RY. Characterization of engineered channelrhodopsin variants with improved properties and kinetics. *Biophys J*. 2009;96: 1803–1814.
105. Nern A, Pfeiffer BD, Svoboda K, Rubin GM. Multiple new site-specific recombinases for use in manipulating animal genomes. *Proc Natl Acad Sci U S A*. 2011;108: 14198–14203.
106. Aizawa H, Bianco IH, Hamaoka T, Miyashita T, Uemura O, Concha ML, et al. Laterotopic representation of left-right information onto the dorso-ventral axis of a zebrafish midbrain target nucleus. *Curr Biol*. 2005;15: 238–243.
107. Burgess HA, Granato M. Sensorimotor gating in larval zebrafish. *J Neurosci*. 2007;27: 4984–4994.
108. Pologruto TA, Sabatini BL, Svoboda K. ScanImage: flexible software for operating laser scanning microscopes. *Biomed Eng Online*. 2003;2: 13.
109. Kavaliers M, Choleris E. Antipredator responses and defensive behavior: ecological and ethological approaches for the neurosciences. *Neurosci Biobehav Rev*. 2001;25: 577–586.
110. Lima SL, Dill LM. Behavioral decisions made under the risk of predation: a review and prospectus. *Can J Zool*. NRC Research Press; 1990;68: 619–640.
111. Hammond S, O’Shea M. Escape flight initiation in the fly. *J Comp Physiol A Neuroethol Sens Neural Behav Physiol*. 2007;193: 471–476.
112. Hammond S, O’Shea M. Ontogeny of flight initiation in the fly *Drosophila melanogaster*: implications for the giant fibre system. *J Comp Physiol A Neuroethol Sens Neural Behav Physiol*. 2007;193: 1125–1137.
113. Card G, Dickinson M. Performance trade-offs in the flight initiation of *Drosophila*. *J Exp Biol*. 2008;211: 341–353.
114. Card G, Dickinson MH. Visually mediated motor planning in the escape response of *Drosophila*. *Curr Biol*. 2008;18: 1300–1307.
115. Fotowat H, Fayyazuddin A, Bellen HJ, Gabbiani F. A novel neuronal pathway for visually guided escape in *Drosophila melanogaster*. *J Neurophysiol*. 2009;102: 875–885.
116. Fotowat H, Harrison RR, Gabbiani F. Multiplexing of motor information in the discharge of a collision detecting neuron during escape behaviors. *Neuron*. 2011;69: 147–158.
117. Harrison RR, Fotowat H, Chan R, Kier RJ, Olberg R, Leonardo A, et al. Wireless Neural/EMG Telemetry Systems for Small Freely Moving Animals. *IEEE Trans Biomed*

- Circuits Syst. 2011;5: 103–111.
118. Kupfermann I, Weiss KR. The command neuron concept. *Behav Brain Sci*. Cambridge University Press; 1978;1: 3–10.
 119. Kupfermann I, Weiss KR. Motor program selection in simple model systems. *Curr Opin Neurobiol*. 2001;11: 673–677.
 120. Edwards DH, Heitler WJ, Krasne FB. Fifty years of a command neuron: the neurobiology of escape behavior in the crayfish. *Trends Neurosci*. 1999;22: 153–161.
 121. Eaton RC, Lee RK, Foreman MB. The Mauthner cell and other identified neurons of the brainstem escape network of fish. *Prog Neurobiol*. 2001;63: 467–485.
 122. Bullock TH. Comparative Neuroethology of Startle, Rapid Escape, and Giant Fiber-Mediated Responses. In: Eaton RC, editor. *Neural Mechanisms of Startle Behavior*. Springer US; 1984. pp. 1–13.
 123. Esch T, Kristan WB Jr. Decision-making in the leech nervous system. *Integr Comp Biol*. 2002;42: 716–724.
 124. Wine JJ, Krasne FB. The cellular organization of crayfish escape behavior. *The biology of Crustacea*. Academic Press, NY; 1982;4: 241–292.
 125. Krasne FB, Wine JJ. The Production of Crayfish Tailflip Escape Responses. *Neural Mechanisms of Startle Behavior*. Springer, Boston, MA; 1984. pp. 179–211.
 126. Wiersma CAG. Giant nerve fiber system of the crayfish; a contribution to comparative physiology of synapse. *J Neurophysiol*. 1947;10: 23–38.
 127. Wiersma CAG. Repetitive discharges of motor fibers caused by a single impulse in giant fibers of the crayfish. *J Cell Comp Physiol*. 1952;40: 399–419.
 128. Liu Y-C, Herberholz J. Sensory activation and receptive field organization of the lateral giant escape neurons in crayfish. *J Neurophysiol*. 2010;104: 675–684.
 129. Herberholz J, Antonsen BL, Edwards DH. A lateral excitatory network in the escape circuit of crayfish. *J Neurosci*. 2002;22: 9078–9085.
 130. Wine JJ, Krasne FB. The organization of escape behaviour in the crayfish. *J Exp Biol*. 1972;56: 1–18.
 131. Edwards DH, Yeh SR, Barnett LD, Nagappan PR. Changes in synaptic integration during the growth of the lateral giant neuron of crayfish. *J Neurophysiol*. 1994;72: 899–908.
 132. Heitler WJ, Edwards DH. Effect of temperature on a voltage-sensitive electrical synapse in crayfish. *J Exp Biol*. 1998;201: 503–513.

133. Liden WH, Herberholz J. Behavioral and neural responses of juvenile crayfish to moving shadows. *J Exp Biol.* 2008;211: 1355–1361.
134. Liden WH, Phillips ML, Herberholz J. Neural control of behavioural choice in juvenile crayfish. *Proc Biol Sci.* 2010;277: 3493–3500.
135. Wine JJ. The structural basis of an innate behavioural pattern. *J Exp Biol.* jeb.biologists.org; 1984; Available: <http://jeb.biologists.org/content/112/1/283.short>
136. Herberholz J, Sen MM, Edwards DH. Escape behavior and escape circuit activation in juvenile crayfish during prey-predator interactions. *J Exp Biol.* 2004;207: 1855–1863.
137. Wyman RJ, Thomas JB, Salkoff L, King DG. The *Drosophila* Giant Fiber System. *Neural Mechanisms of Startle Behavior.* Springer, Boston, MA; 1984. pp. 133–161.
138. Allen MJ, Godenschwege TA, Tanouye MA, Phelan P. Making an escape: development and function of the *Drosophila* giant fibre system. *Semin Cell Dev Biol.* 2006;17: 31–41.
139. Bellen HJ, Tong C, Tsuda H. 100 years of *Drosophila* research and its impact on vertebrate neuroscience: a history lesson for the future. *Nat Rev Neurosci.* 2010;11: 514–522.
140. Power ME. The thoracico-abdominal nervous system of an adult insect, *Drosophila melanogaster*. *J Comp Neurol.* 1948;88: 347–409.
141. Trimarchi JR, Schneiderman AM. Initiation of flight in the unrestrained fly, *Drosophila melanogaster*. *J Zool.* Blackwell Publishing Ltd; 1995;235: 211–222.
142. McKenna M, Monte P, Helfand SL, Woodard C, Carlson J. A simple chemosensory response in *Drosophila* and the isolation of *acj* mutants in which it is affected. *Proc Natl Acad Sci U S A.* 1989;86: 8118–8122.
143. Holmqvist MH. A visually elicited escape response in the fly that does not use the giant fiber pathway. *Vis Neurosci.* 1994;11: 1149–1161.
144. Trimarchi JR, Schneiderman AM. Different neural pathways coordinate *Drosophila* flight initiations evoked by visual and olfactory stimuli. *J Exp Biol.* 1995;198: 1099–1104.
145. Sun H, Frost BJ. Computation of different optical variables of looming objects in pigeon nucleus rotundus neurons. *Nat Neurosci.* 1998;1: 296–303.
146. Rind FC, Simmons PJ. Orthopteran DCMD neuron: a reevaluation of responses to moving objects. I. Selective responses to approaching objects. *J Neurophysiol.* 1992;68: 1654–1666.
147. Oliva D, Medan V, Tomsic D. Escape behavior and neuronal responses to looming

- stimuli in the crab *Chasmagnathus granulatus* (Decapoda: Grapsidae). *J Exp Biol.* 2007;210: 865–880.
148. Nakagawa H, Hongjian K. Collision-sensitive neurons in the optic tectum of the bullfrog, *Rana catesbeiana*. *J Neurophysiol.* 2010;104: 2487–2499.
 149. Riede K. Prepulse inhibition of the startle reaction in the locust *Locusta migratoria* (Insecta: Orthoptera: Acridoidea). *J Comp Physiol A.* Springer-Verlag; 1993;172: 351–358.
 150. Friedel T. The vibrational startle response of the desert locust *Schistocerca gregaria*. *J Exp Biol.* 1999;202: 2151–2159.
 151. Pearson KG, O’Shea M. Escape Behavior of the Locust. *Neural Mechanisms of Startle Behavior.* Springer, Boston, MA; 1984. pp. 163–178.
 152. Burrows M. *The neurobiology of an insect brain.* Oxford University Press on Demand; 1996.
 153. Santer RD, Yamawaki Y, Rind FC, Simmons PJ. Motor activity and trajectory control during escape jumping in the locust *Locusta migratoria*. *J Comp Physiol A Neuroethol Sens Neural Behav Physiol.* 2005;191: 965–975.
 154. Hassenstein B, Hustert R. Hiding responses of locusts to approaching objects. *J Exp Biol.* 1999;202 (Pt 12): 1701–1710.
 155. Burrows M, Morris G. The kinematics and neural control of high-speed kicking movements in the locust. *J Exp Biol.* 2001;204: 3471–3481.
 156. Simmons PJ, Rind FC, Santer RD. Escapes with and without preparation: the neuroethology of visual startle in locusts. *J Insect Physiol.* 2010;56: 876–883.
 157. Heitler WJ, Burrows M. The locust jump. I. The motor programme. *J Exp Biol.* 1977;66: 203–219.
 158. Fotowat H, Gabbiani F. Relationship between the phases of sensory and motor activity during a looming-evoked multistage escape behavior. *J Neurosci.* 2007;27: 10047–10059.
 159. Santer RD, Yamawaki Y, Rind FC, Simmons PJ. Preparing for escape: an examination of the role of the DCMD neuron in locust escape jumps. *J Comp Physiol A Neuroethol Sens Neural Behav Physiol.* 2008;194: 69–77.
 160. Gray JR, Blincow E, Robertson RM. A pair of motion-sensitive neurons in the locust encode approaches of a looming object. *J Comp Physiol A Neuroethol Sens Neural Behav Physiol.* 2010;196: 927–938.
 161. Santer RD, Simmons PJ, Rind FC. Gliding behaviour elicited by lateral looming stimuli

- in flying locusts. *J Comp Physiol A Neuroethol Sens Neural Behav Physiol*. 2005;191: 61–73.
162. Santer RD, Rind FC, Stafford R, Simmons PJ. Role of an identified looming-sensitive neuron in triggering a flying locust's escape. *J Neurophysiol*. 2006;95: 3391–3400.
 163. Hemmi JM, Tomsic D. The neuroethology of escape in crabs: from sensory ecology to neurons and back. *Curr Opin Neurobiol*. 2012;22: 194–200.
 164. Medan V, Oliva D, Tomsic D. Characterization of lobula giant neurons responsive to visual stimuli that elicit escape behaviors in the crab *Chasmagnathus*. *J Neurophysiol*. 2007;98: 2414–2428.
 165. de Astrada MB, Tomsic D. Physiology and morphology of visual movement detector neurons in a crab (Decapoda: Brachyura). *J Comp Physiol A*. Springer-Verlag; 2002;188: 539–551.
 166. Sztarker J, Tomsic D. Neuronal correlates of the visually elicited escape response of the crab *Chasmagnathus* upon seasonal variations, stimuli changes and perceptual alterations. *J Comp Physiol A Neuroethol Sens Neural Behav Physiol*. 2008;194: 587–596.
 167. Tomsic D, Berón de Astrada M, Sztarker J. Identification of individual neurons reflecting short- and long-term visual memory in an arthropod. *J Neurosci*. 2003;23: 8539–8546.
 168. Sztarker J, Tomsic D. Brain Modularity in Arthropods: Individual Neurons That Support “What” But Not “Where” Memories. *J Neurosci*. Society for Neuroscience; 2011;31: 8175–8180.
 169. Ydenberg RC, Dill LM. The Economics of Fleeing from Predators. *Adv Stud Behav*. 1986;16: 229–249.
 170. Schall JD. Neural basis of deciding, choosing and acting. *Nat Rev Neurosci*. 2001;2: 33–42.
 171. Rangel A, Camerer C, Montague PR. A framework for studying the neurobiology of value-based decision making. *Nat Rev Neurosci*. 2008;9: 545–556.
 172. Glimcher PW, Rustichini A. Neuroeconomics: the consilience of brain and decision. *Science*. 2004;306: 447–452.
 173. Huettel SA, Song AW, McCarthy G. Decisions under uncertainty: probabilistic context influences activation of prefrontal and parietal cortices. *J Neurosci*. 2005;25: 3304–3311.
 174. Sugrue LP, Corrado GS, Newsome WT. Choosing the greater of two goods: neural currencies for valuation and decision making. *Nat Rev Neurosci*. 2005;6: 363–375.

175. Kristan W, Gillette R. Behavioral choice. Cold Spring Harbor Monogr Ser. CSH COLD SPRING HARBOR LABORATORY PRESS; 2007;49: 533.
176. Kristan WB. Neuronal decision-making circuits. *Curr Biol*. 2008;18: R928–32.
177. Chittka L, Skorupski P, Raine NE. Speed–accuracy tradeoffs in animal decision making. *Trends Ecol Evol*. 2009;24: 400–407.
178. Kovac MP, Davis WJ. Behavioral choice: neural mechanisms in Pleurobranchaea. *Science*. 1977;198: 632–634.
179. Jing J, Gillette R. Neuronal elements that mediate escape swimming and suppress feeding behavior in the predatory sea slug Pleurobranchaea. *J Neurophysiol*. 1995;74: 1900–1910.
180. Gillette R, Huang RC, Hatcher N, Moroz LL. Cost-benefit analysis potential in feeding behavior of a predatory snail by integration of hunger, taste, and pain. *Proc Natl Acad Sci U S A*. 2000;97: 3585–3590.
181. Jing J, Gillette R. Directional avoidance turns encoded by single interneurons and sustained by multifunctional serotonergic cells. *J Neurosci*. 2003;23: 3039–3051.
182. Hirayama K, Gillette R. A neuronal network switch for approach/avoidance toggled by appetitive state. *Curr Biol*. 2012;22: 118–123.
183. Harley CM, English BA, Ritzmann RE. Characterization of obstacle negotiation behaviors in the cockroach, *Blaberus discoidalis*. *J Exp Biol*. 2009;212: 1463–1476.
184. Harley CM, Ritzmann RE. Electrolytic lesions within central complex neuropils of the cockroach brain affect negotiation of barriers. *J Exp Biol*. 2010;213: 2851–2864.
185. Herberholz J, Issa FA, Edwards DH. Patterns of neural circuit activation and behavior during dominance hierarchy formation in freely behaving crayfish. *J Neurosci*. 2001;21: 2759–2767.
186. Glanzman DL, Krasne FB. Serotonin and octopamine have opposite modulatory effects on the crayfish's lateral giant escape reaction. *J Neurosci*. 1983;3: 2263–2269.
187. Bustamante J, Krasne FB. Effects of octopamine on transmission at the first synapse of the crayfish lateral giant escape reaction pathway. *J Comp Physiol A*. Springer-Verlag; 1991;169: 369–377.
188. Stern M, Thompson KSJ, Zhou P, Watson DG, Midgley JM, Gewecke M, et al. Octopaminergic neurons in the locust brain: morphological, biochemical and electrophysiological characterisation of potential modulators of the visual system. *J Comp Physiol A*. Springer-Verlag; 1995;177: 611–625.

189. Pflüger HJ, Duch C, Heidel E. Neuromodulatory octopaminergic neurons and their functions during insect motor behaviour. The Ernst Florey memory lecture. *Acta Biol Hung.* 2004;55: 3–12.
190. Harvey J, Brunger H, Middleton CA, Hill JA, Sevdali M, Sweeney ST, et al. Neuromuscular control of a single twitch muscle in wild type and mutant *Drosophila*, measured with an ergometer. *Invert Neurosci.* 2008;8: 63–70.
191. Rind FC, Santer RD, Wright GA. Arousal facilitates collision avoidance mediated by a looming sensitive visual neuron in a flying locust. *J Neurophysiol.* 2008;100: 670–680.
192. Crisp KM, Mesce KA. Beyond the central pattern generator: amine modulation of decision-making neural pathways descending from the brain of the medicinal leech. *J Exp Biol.* 2006;209: 1746–1756.
193. Mesce KA, Pierce-Shimomura JT. Shared Strategies for Behavioral Switching: Understanding How Locomotor Patterns are Turned on and Off. *Front Behav Neurosci.* 2010;4. doi:10.3389/fnbeh.2010.00049
194. Daw ND, Kakade S, Dayan P. Opponent interactions between serotonin and dopamine. *Neural Netw.* 2002;15: 603–616.
195. Clarac F, Pearlstein E. Invertebrate preparations and their contribution to neurobiology in the second half of the 20th century. *Brain Res Rev.* 2007;54: 113–161.